ABSTRACT

Non-Isothermal Non-Newtonian Flow and Interlayer Adhesion in Large Area Additive Manufacturing Polymer Composite Deposition

Blake P. Heller, Ph.D.

Mentor: Douglas E. Smith, Ph.D.

Large Area Additive Manufacturing (LAAM) has seen substantial improvement in recent years due in large part to the addition of short carbon fiber reinforcement to the polymer feedstock. The addition of short carbon fibers improves the anisotropic mechanical and thermomechanical properties of printed beads which are dependent on the spatially varying orientation of carbon fibers. In this research, the finite element method is used to evaluate Stokes flow of a temperature dependent Carreau-Yasuda fluid for a two-dimensional planar flow field within a Strangpresse Model 19 LAAM extrusion nozzle. A shape optimization method is developed to zero the surface normal velocity to compute the polymer melt flow field geometry immediately after the nozzle exit during deposition onto a moving platform. Fiber orientation tensors are calculated within the extrudate using a custom software program which applies a rotary diffusion function to account for fiber interaction and the orthotropic fitted closure. The bulk mechanical and thermomechanical properties are calculated using the orientation homogenization method in the deposited bead. The computed thermal conductivity of the carbon fiber polymer composite that composes the deposited bead is then used to evaluate bead cooling for

single and multi-bead printed layers which provides temperature along the interlayer bond line with respect to time. Infrared heating of printed beads, an addition to the current deposition process, is also modeled to determine the increase in temperature along the bond line for LAAM printing. Post deposition smooth and textured rolling are used to improve polymer bonding and increase bond area between interlayer surfaces. Interlayer bonding of printed beads with and without processing improvements are evaluated with shear testing of lap joint test specimens. Results show high fiber alignment in the longitudinal direction and increased thermal conductivity in all three dimensions of the fiber filled polymer beads which decreases the bonding time between layers and decreases bond strength. In addition, these deposition processing modifications increase bond strength by increasing temperature between layers, intimate contact between layers, and bonding surface area. Improved bonding between layers increases overall part strength and industrial viability of large area additively manufactured parts.

Non-Isothermal Non-Newtonian Flow and Interlayer Adhesion in Large Area Additive Manufacturing Polymer Composite Deposition

by

Blake P. Heller, B.S., M.S.

A Dissertation

Approved by the Department of Mechanical Engineering

_____

Paul I. Ro, Ph.D., Chairperson

Submitted to the Graduate Faculty of
Baylor University in Partial Fulfillment of the
Requirements for the Degree
of

Doctor of Philosophy

Approved by the Dissertation Committee

_____

Douglas E. Smith, Ph.D., Chairperson

_____

David A. Jack, Ph.D.

_____

Abhendra Singh, Ph.D.

_____

Jill Klentzman, Ph.D.

_____

Ronald Morgan, Ph.D.

Accepted by the Graduate School

December 2019

_____

J. Larry Lyon, Ph.D., Dean

Page bearing signatures is kept on file in the Graduate School.

TABLE OF CONTENTS

LIST OF FIGURES

LIST OF TABLES

ACKNOWLEDGMENTS

I would like to first thank my advisor Dr. Douglas E. Smith for all of his support and guidance through this project. As well, I would like to thank Dr. David Jack for his help in answering my many questions, and for the use of his MATLAB code for the calculation of fiber orientation. I would like to also thank my committee for their willingness to improve the content of this dissertation. A special thanks goes to all of the materials research group who keep the office environment as stress free and lighthearted as possible. Last, I would like to thank my wife, daughter, and family for all their support and understanding for the long hours I have spent away to complete this work.

DEDICATION

To my loving wife and daughter who
have supported and kept me focused through all my endeavors

CHAPTER ONE

Introduction

1.1 Research Motivation and Objective

Large Area Additive Manufacturing (LAAM) is a polymer deposition additive manufacturing technology that has greatly increased in popularity and industrial viability in recent years. There has been substantial improvement in mechanical and thermomechanical properties of polymers due in large part to additives such as carbon, glass, copper, and iron fibers and spherules to the polymer feedstock [1-4]. Mechanical and thermomechanical properties of these composites are spatially varying and highly dependent on the orientation of the additive fibers which is a function of velocity gradients in the polymer flow field.

Substantial research has focused on the orientation and resultant mechanical and thermomechanical property prediction of fiber filled polymers in deposition printing processes [5-9], as well as mechanical testing and imaging of tested surfaces for fiber orientation in printed parts [2, 10-11]. Anisotropic mechanical and thermomechanical properties of fiber filled additively manufactured parts have been computed [6-9] using the orientation homogenization method for fiber orientation which was proposed by Advani and Tucker [12] and derived by Jack and Smith [13]. In this research, fiber orientation in the fluid domain is calculated using orientation tensors (first applied to short fiber composites by Advani and Tucker [12]) with the Orthotropic Fitted Closure

[14, 15] and both the isotropic rotary diffusion function and the reduced strain closure methods proposed by Folgar-Tucker [16] and Wang, et al. [17], respectfully.

The prediction of fiber orientation in LAAM short fiber reinforced polymers depends on modeling of the deposition process including the prediction of extrudate swell of the polymer after the nozzle exit and flow shape upon deposition onto the print plate or previously printed beads. Prediction of polymer extrudate shape for the Fused Filament Fabrication (FFF) and LAAM processes has been of significant interest in recent years and is one of the topics considered in this dissertation.

Bellini, et al. [18] created a planar deposition model for FFF printed ceramic materials which analyzed start and stop flow characteristics but did not include steady state deposition which occurs during the majority of the FFF print process. Heller, et al. [6] created an axisymmetric extrudate swell model of a Newtonian fluid passing through an FFF print nozzle from which the fiber orientation and mechanical properties were evaluated. Heller, et al. [7] improved the previous model by including the turning flow of the polymer during LAAM deposition with a two-dimensional Newtonian planar model where the die geometry was based on the Strangpresse Model 19 nozzle [19]. This work evaluated the fiber orientation and resulting mechanical and thermomechanical properties of the printed bead.

Though great strides have been made to improve the quality of polymer deposition printing, issues still exist that effect the final part quality and strength. A significant issue limiting the application of deposition additive manufacturing printing are the interlayer and intralayer bond strength [20], and void formation between adjacent beads [21].

This dissertation focuses on interlayer temperature, and the resultant bond strength including experimental testing. Substantial research has been performed on analyzing bond formation in deposition additive manufacturing processes [22-24] and is based on the bonding theories derived for polymer welding of joined plastics [25-27] and weld line analysis [28] in injection molded parts. Polymer bonding through healing or autohesion depends on time, temperature, and degree of intimate contact, where the latter is based on pressure, viscosity, and roughness at the bonding interface. Accurate heat transfer models are needed to predict the time and temperature dependent diffusion during the adhesion process. Several heat transfer models for the polymer deposition additive manufacturing process have been developed [29-31], but do not consider the effect of the short fibers suspension on the thermal properties of the bonding materials. A heat transfer model for multi-bead deposition is presented in this dissertation and is expanded for the addition of infrared pre-deposition heating of the printed polymer.

For the work done in this dissertation infrared pre-deposition heating is added to the deposition process, as well as a post deposition roller and a textured post deposition roller. These additions are included for the purpose of improving interlayer polymer bonding. Pre-deposition heat application has been included in the deposition additive manufacturing print process in many studies [20, 32-34], but application has been purely experimental without predictive tools to optimize the pre-deposition heating process. Application of pressure post deposition has also been reported by Kunc, et al. [10] who use a “z-tamper” to compress printed materials immediately after deposition which has been shown to improve interlayer bond strength. To the authors knowledge the application of texture to the printed bead post deposition has not been analyzed.

Patterning of adhesive layers has been seen in aerospace applications of adhesive joining to greatly improve the mechanical properties of the joint [35-40]. The proposed textured roller is expected to both increase bonding area and create a mechanical interlock between successively printed layers.

The goal of this dissertation is to model the extrudate geometry for steady state deposition of fiber filled polymers from a large area additive manufacturing printer, as well as model and improve the bond formation between successive beads. The latter is tested with a single lap shear tensile testing method. The extrudate deposition flow shape is calculated using a minimization technique to zero the normal velocity along the free surface boundaries after the nozzle exit until deposition onto the print platform. The analysis employs a two-dimensional planar temperature dependent Carreau-Yasuda fluid undergoing Stokes flow. Fiber orientation is calculated using the orientation tensor approach proposed first by Advani and Tucker [12], and mechanical and thermomechanical properties are evaluated from the fiber orientation state in the deposited bead using the orientation homogenization method derived by Jack and Smith [13] which also appears in Advani and Tucker [12]. Bond strength between successively deposited beads is evaluated using a two-dimensional planar heat transfer finite element model and bond strength growth analyses [41-43]. Experimental testing of bond strength is evaluated using lap joint test specimens based on the ASTM D3163-01 standard, and printed with the Baylor Large Area Additive Manufacturing Printer which uses a Strangpresse Model 19 [19] extruder and a CNC-based gantry system. Pre-deposition infrared heating and post-deposition rolling and texturing of the printed beads is also

studied in this dissertation as methods to improve interlayer bonding between successive beads.

1.2 Order of Dissertation

Chapter Two presents an in-depth review of previously published literature pertaining to the topics presented in this dissertation, such as extrudate swell modeling, fiber orientation evaluation, mechanical and thermomechanical property evaluation for misaligned short fiber polymer composites, polymer bonding analysis, and experimental testing for LAAM printing techniques. Chapter Three covers deposition flow modeling of a Newtonian fluid in Large Area Additive Manufacturing as well as fiber orientation and mechanical and thermomechanical property evaluation in the deposited bead. This chapter was previously published in the Journal of Additive Manufacturing. In this journal article D. E. Smith provided polymer melt flow modeling guidance, D. A. Jack provided fiber orientation and property evaluation modeling guidance and source code for the evaluation of fiber orientation and property evaluation in a flow domain, and B. P. Heller created the flow model used, built upon the code for fiber orientation and property evaluation, ran all calculations, and created all figures in the published document. Chapter Four presents an improved deposition flow model which incorporates a temperature dependent Carreau-Yasuda fluid flow with effects of the heated aluminum print plate considered on polymer bead cooling. Chapter Five presents two transient heat transfer models of a two-dimensional planar bead stack (with and without infrared pre-deposition heating). Chapter Six presents analytical bond strength prediction and experimental testing of the bond strength using LAAM printed single lap shear tensile specimens. Chapter Seven covers the results and conclusions presented in this

dissertation as well as recommendations for future work in the area of Large Area Additive Manufacturing.

CHAPTER TWO

Literature Review

Polymer Deposition Additive Manufacturing (PDAM) is an Additive Manufacturing method that has grown substantially in popularity over the last decade and is quickly becoming an industrially viable manufacturing method. Due to the inclusion of fiber reinforced materials in PDAM processes interest in orientation of short fibers and the resulting mechanical and thermomechanical properties has seen renewed interest. Extrudate swell and fiber orientation has been studied for decades and is reviewed and discussed in this chapter. To properly define the orientation of fibers flowing in a polymer melt, through a PDAM extrusion nozzle, there must be a thorough understanding of all factors that affect the fiber filled melt. Properly defining the extrudate swell is pivotal to the understanding of the polymer melt geometry after the nozzle exit. The exact values of the extrudate swell for Newtonian and Non-Newtonian fluids are important in the design and manufacturing of extrusion dies.

Recently the bonding of successively deposited beads in a PDAM printed part has become an area of focus in Additive Manufacturing research. Polymer bonding has been studied for decades and has seen renewed interest with respect to PDAM printing. Due to the poor bonding that occurs in the printing process additions have been made to improve bonding between successively deposited layers. The relevant works in polymer bonding and process additions to improve interlayer bonding are reviewed and discussed in this chapter.

2.1 Polymer Deposition Modeling

Polymer melt flow modeling has been studied substantially for traditional molding processes such as extrusion, injection molding, and compression molding. Due to the novel method created by the Polymer Deposition Additive Manufacturing (PDAM) technique a new modeling effort has been seen recently for this process. Traditional modeling and new modeling approaches are discussed in this section and its applicability to the modeling approach presented in this dissertation are discussed.

2.1.1 Polymer Extrusion Modeling

Extrudate swell of polymer melt flows has been studied in depth over the last several decades and is well understood for traditional manufacturing processes. When a polymer melt flow is extruded from an orifice it expands and the percent expansion is dictated by the type of fluid that is being modeled and the external conditions immediately outside of the die. The swell of fluids is modeled by a free surface approach where the compressed fluid becomes a fluid jet after the nozzle exit. Tanner [44, 45] prescribed several assumptions that must be made in evaluating the extrudate swell of fluids exiting a die. The assumptions are (a) flow is isothermal and incompressible, (b) the die is long meaning length/diameter of the die is much greater than one, $\frac{l_{die}}{d_{die}} \gg 1$, (c) gravity, body forces, and surface tension are ignored, (d) no fluid inertia, and (e) small slow recovery far from the die is ignored. Using the given assumptions Tanner [44, 45] defines an equation for extrudate swell of a viscoelastic fluid exiting a circular nozzle given as

$$\frac{D}{d} = \left[1 + \frac{1}{2}\left(\frac{N_1}{2\tau_w}\right)\right]^{\frac{1}{6}} + 0.13 \tag{2.1}$$

where N_1 is the first normal stress difference at the wall of a long circular die, d is the diameter of the die exit, τ_w is the wall shear stress, D is the diameter of the extrudate after die exit, and the 0.13 term takes into account the swell of a Newtonian fluid undergoing Stokes flow. For a Newtonian fluid N_1 is zero which causes the swell value in Equation 2.1 to be 1.13 or 13% swell.

Stokes flow of an incompressible flow is defined by the continuity and momentum equations given as

$$\nabla \cdot \mathbf{v} = 0 \tag{2.2}$$

$$\nabla \cdot \boldsymbol{\sigma} = 0 \tag{2.3}$$

where $\mathbf{v}$ is the velocity vector and $\boldsymbol{\sigma}$ is the stress tensor which is given as

$$\boldsymbol{\sigma} = -p\boldsymbol{I} + \mu[(\nabla \mathbf{v}) + (\nabla \mathbf{v})^{\mathrm{T}}] \tag{2.4}$$

In Equation 2.4, p is the pressure, $\boldsymbol{I}$ is the identity tensor, and μ is the fluid viscosity.

Modeling of the free surface requires two boundary conditions, (1) boundary stress must be equal to zero, and (2) the normal velocity along the boundary must be equal to zero given as

$$\boldsymbol{\sigma} : [\mathbf{nn}] = 0 \tag{2.5}$$

and

$$\mathbf{u} \cdot \mathbf{n} = 0 \tag{2.6}$$

where ":" indicates the double contraction of the stress tensor with the outer product of the normal vector with itself, which gives the stress traction along the free surface. When modeling the swell of a polymer extrudate one of the boundary conditions is set and the

other condition is solved for through a minimization technique. Defining the surface stress as equal to zero is termed the zero surface tension method and defining the normal velocity as equal to zero is termed the zero penetration method [46].

The first study considered is by Georgiou [47, 48] who analyzed extrudate swell of a Newtonian fluid using a finite element model to evaluate the stick slip free surface of an axisymmetric fluid jet exiting an extrusion die. The authors found that the measured extrudate swell for the Newtonian fluid was 13% and that the swell had a particular rate of expansion. Heller, et al. [6] used an axisymmetric model of a Fused Filament Fabrication (FFF) nozzle, applied the free surface model to the extrudate swell of a Newtonian fluid and found that the expected 13% swell was matched. Elwood, et al. [49] used a finite element model to evaluate the extrudate swell of a Newtonian fluid exiting a square die and found that the swell was equal to 19% due to the non-circular nature of the die exit. The larger swell seen for rectangular dies was also calculated by Karagiannis, et al. [50] and has been shown experimentally by Michaeli [51]. Heller, et al. [7] used a two-dimensional planar finite element model with Stokes flow of a Newtonian fluid and found the expected 19% swell result was matched for a rectangular die. Due to the two-dimensional nature, this represents the extrusion of a rectangular sheet being extruded from a Large Area Additive Manufacturing (LAAM) extrusion nozzle. Mitsoulis, et al. [52] used a similar numerical approach to that of Gergiou [47, 48] for the swell of a Newtonian fluid exiting an extrusion die to show the effects of gravity, inertia, slip at the wall, surface tension, pressure dependence of viscosity, and compressibility on percent swell of the extruded material. It was found that swell ratios could range from -90% to 50% dependent on the given parameters. The extremes of these swell percentages do

come from unlikely processing conditions, but it does show the effect that these factors have on extrudate swell.

In the previous models, polymer melts were described as a Newtonian fluid flow which is known to not fully represent the shear thinning and viscoelastic nature that is exhibited by polymers. Studies have taken into consideration these effects and are presented here.

Mitsoulis and Hatzikiriakos [53] and Kanvisi, et al. [54] have simulated die swell using viscoelastic material models to include the elastic effects in polymer melts and have found that extrudate swell ratios are larger than those produced with Newtonian fluid models, as expected. Wang, et al. [9] analyzed a similar axisymmetric model to that of Heller, et al. [6] of a FFF extrusion nozzle, but took into consideration the swell of Power Law, Carreau-Yasuda, Simplified Viscoelastic, and Phan-Thien-Tanner models for polymer melts. Swell ratios for the Power Law and Carreau-Yasuda models were found to be approximately 3%, the Newtonian model was found to be 13% as expected, and the Simplified Viscoelastic and PTT models were found to be approximately 20% which represents the expected increase for Non-Newtonian viscoelastic flow models.

2.1.2 Extrusion Deposition Flow Modeling

Many researchers have made an effort to model the extrusion and deposition of materials onto a print platform which occurs in the FFF process and extrusion deposition process. Bellini, et al. [18] modeled the two-dimensional planar flow of small scale extrusion of ceramics onto a print platform using Ansys Polyflow (Ansys, Inc., Canonsbug, PA). The start and stop characteristic shapes of the deposited ceramic was found, but did not take into consideration the steady state deposition properties that exist

during the majority of the printing process or the inclusion of filler materials. Bellini, et al. [18] also evaluated the pressure driven flow of a filament based extrusion system and buckling of the filament which occurs when the drive force becomes greater than the buckling strength of the respective material. Nixon, et al. [55] was one of the first to analyze the extrusion of a fiber filled polymer from an FFF nozzle by modeling the flow out of an FFF nozzle into an open cavity using Moldflow (Autodesk, Inc., San Rafael, CA). Lewicki, et al. [56] analyzed a fiber filled epoxy with an 8% volume fraction of carbon fibers exiting an extrusion nozzle. Carbon fibers were modeled as discrete particles which was highly computationally expensive, but it was found that in the areas close to the nozzle wall fibers aligned most quickly due to high shear rates. The post nozzle exit orientation of fibers was again neglected due to computational constraints. These methods did not evaluate the swell of the extrudate after the nozzle exit which will affect the fiber orientation. Heller, et al. [6] modeled the Stokes flow of a fiber filled Newtonian fluid in an axisymmetric representation of an FFF nozzle. This model took into consideration the extrudate swell which occurs after the nozzle exit and its effects on the fiber alignment in the extruded material. In the initial study by Heller, et al. [6] a parametric study of nozzle geometry and its effects on fiber alignment were considered and it was shown fiber alignment and the resulting mechanical properties could be changed substantially with changing nozzle geometry. Wang, et al. [9] improved the axisymmetric extrusion model by including the extrusion of generalized Newtonian fluids and viscoelastic fluids from an FFF nozzle. The extrudate swell of the given fluids was analyzed as well as the effects on fiber orientation of increased swell ratios. It was found that the swell does effect the fiber orientation, but the average mechanical properties

through the extrudate thickness found for higher swell ratios did not change substantially. In a work by Osswald, et al. [57], which analyzed in depth the melt effects of a filament as it enters the heated nozzle, found that the preceding works incorrectly assumed complete melting of the filament upon entrance into the nozzle. It was shown complete melting of the filament did not occur until much further into the nozzle. Ramanath, et al. [58] used Ansys Polyflow (Ansys, Inc., Canonsbug, PA) to analyze a two-dimensional planar model of a power law fluid and found that the polymer filament (poly-ε-caprolactone) did not fully melt until it was 42 mm inside the heated nozzle. Other considerations have also been analyzed for filament-based systems such as annular backflow by Gilmer, et al. [59] where the polymer melt flows backward in the nozzle around the filament being fed in which is not in contact with the side wall. The annular backflow would also affect fiber orientation in filament based system which should be studied. The transition from filament-based extrusion systems to pellet fed Large Area Additive Manufacturing systems avoids the concern for the issues stated by Osswald and Gilmer. In pellet-based systems which utilize long polymer extrusion screws the polymer is fully melted before entering the final nozzle geometry and backflow is negligible.

In the analysis by Mulholland, et al. [2] of the extrusion of copper fiber filled polymers it was stated that the 90 degree turn that occurs during deposition onto a print platform was necessary for correct modeling of the fiber orientation. Heller, et al. [7] analyzed the turning (or deposition flow) using a two-dimensional planar Stokes flow of a fiber filled Newtonian fluid and the effect of the turn on fiber orientation. It was shown that while the fiber orientation did change through the thickness of the deposited bead, bulk mechanical and thermomechanical properties changed very little. In a study by

Russell, et al. [8], which utilized the planar deposition flow model created by Heller, et al. [7], it was shown that the use of different fiber orientation models effected the resultant fiber orientation and the associated mechanical and thermomechanical properties. In this work, the coefficient of thermal expansion in deposited beads for misaligned fibers was evaluated for the first time in fiber filled polymer deposition. Wang, et al. [60] has recently analyzed the rotational velocity gradients caused by the screw which is used in LAAM polymer deposition. It was found that the upstream rotation of the screw causes a reduced degree of fiber alignment in the direction of extrusion which decreases the average mechanical properties through the thickness of extruded beads.

2.2 Fiber Orientation and Property Evaluation

Fiber orientation models are used to evaluate the direction of groups of fibers suspended in fiber filled polymer flows. The orientation state in printed beads can then be used to predict the mechanical and thermomechanical properties of short fiber reinforced polymer parts. These models have seen significant research over the past several decades for traditional manufacturing processes such as injection and compression molding and are well understood. These models are used in commercial software packages such as Moldflow (Autodesk, Inc., San Rafael, CA) and Moldex 3D (CoreTech System Co., Ltd., Hsinchu County, Taiwan). However, fiber orientation models and property evaluation models presented in this dissertation are done using an in house software. There has been a renewed interest in fiber orientation to describe the mechanical and thermomechanical properties as it relates to the LAAM printing process which is presented in this dissertation.

2.2.1 Fiber Orientation Models

The study of fiber orientation can be traced back to work by Einstein [61] who studied the motion of spherical inclusions in a viscous fluid. Jeffery [62] expanded this work to include the periodic tumbling motion of an ellipsoidal fiber suspended in viscous incompressible flow. Jeffery assumed that the fiber is suspended in simple shear flow and a low Reynolds number flow, which is applicable to polymer melt flows. Jeffery also assumed no fiber-fiber interaction and no fiber boundary interaction based on the assumption that the motion of a fiber in a dilute solution would be influenced by its nearest neighbor. Jeffery's assumptions can be written in differential form as [16]

$$\frac{D\mathbf{p}}{Dt} = \boldsymbol{\Omega} \cdot \mathbf{p} + \lambda(\boldsymbol{\Gamma} \cdot \mathbf{p} - \boldsymbol{\Gamma} : \mathbf{ppp}) \tag{2.7}$$

where **p** is the unit vector along the primary axis of the fiber with components given as

$$p_1 = \sin\theta\cos\varphi\,,\; p_2 = \sin\theta\sin\varphi\,,\; p_3 = \cos\theta \tag{2.8}$$

In Equation 2.8, θ and φ are angles between the p vector and the principal coordinate system as is shown in Figure 2.1.

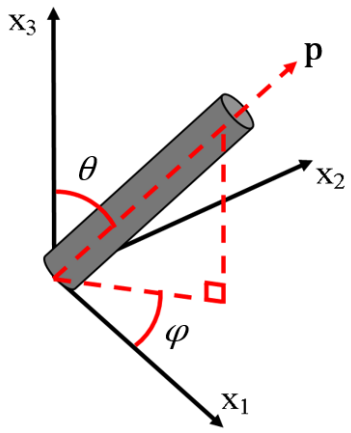

Figure 2.1. Single Fiber Coordinate System for Jeffery's Equation

In Equation 2.7, $\boldsymbol{\Omega}$ is the vorticity tensor given as

$$\boldsymbol{\Omega} = \frac{1}{2}[(\nabla \mathbf{v}) - (\nabla \mathbf{v})^{\mathrm{T}}] \tag{2.9}$$

and $\boldsymbol{\Gamma}$ is the rate of deformation tensor given as

$$\boldsymbol{\Gamma} = \frac{1}{2}[(\nabla \mathbf{v}) + (\nabla \mathbf{v})^{\mathrm{T}}] \tag{2.10}$$

In Equation 2.7, λ is a coefficient related to fiber geometry as

$$\lambda = \frac{r_e^2 - 1}{r_e^2 + 1} \tag{2.11}$$

where r_e is the equivalent aspect ratio which is calculated for a cylindrical fiber as (see e.g., Zhang [63])

$$r_e = 0.000035\beta^3 - 0.00467\beta^2 + 0.764\beta + 0.404 \tag{2.12}$$

where $\beta = l/d$ is the geometric aspect ratio of the cylindrical fiber, l is the length, and d is the diameter.

Direct implementation of Jeffery's method for short fiber composites is computationally prohibitive since each of the thousands of fibers must be evaluated separately. Also, Jeffery's approach is only effective for dilute suspensions which is not the case for LAAM printed composites. Folgar and Tucker [16] introduced the fiber orientation probability density function $\psi(\mathbf{p})$ to represent a large number of interacting short fibers which is time dependent given as

$$\frac{d\psi}{dt} = -\nabla \cdot \mathbf{p} \cdot \left((\boldsymbol{\Omega} \cdot \mathbf{p} + \lambda \boldsymbol{\Gamma} \cdot \mathbf{p} - \lambda \boldsymbol{\Gamma} : \mathbf{ppp})\psi(\mathbf{p})\right) + \boldsymbol{D_r} \tag{2.13}$$

In Equation 2.13, $\boldsymbol{D_r}$ is the rotary diffusion function which accounts for fiber interaction. Computing the fiber orientation distribution function as a function of time is also computationally expensive; therefore, it is common to compute the moments of the

distribution function which was first proposed by Advani and Tucker [12] for short fiber composites. The termed "orientation tensor" approach is a Fourier series expansion of the probability distribution function. The differential equation for computing the time history of the second order orientation tensor $\boldsymbol{A}$ is written as

$$\frac{D\boldsymbol{A}}{Dt} = -\frac{1}{2}(\boldsymbol{\Omega}\cdot\boldsymbol{A}-\boldsymbol{A}\cdot\boldsymbol{\Omega})+\frac{1}{2}\lambda(\boldsymbol{\Gamma}\cdot\boldsymbol{A}+\boldsymbol{A}\cdot\boldsymbol{\Gamma}-2\mathbb{A}:\boldsymbol{\Gamma})+\boldsymbol{D_r} \tag{2.14}$$

where the second, $\boldsymbol{A}$, and fourth order, $\mathbb{A}$, orientation tensors are defined respectively as

$$\boldsymbol{A}_{ij} = \oint p_i p_j \psi(\mathbf{p}) d\mathbf{p} \tag{2.15}$$

$$\mathbb{A}_{ijkl} = \oint p_i p_j p_k p_l \psi(\mathbf{p}) d\mathbf{p} \tag{2.16}$$

The Advani and Tucker orientation tensor approach improves the calculation speed compared to the probability distribution function. Advani and Tucker [12] stated an increase in computation speed of two orders of magnitude, but it was shown later by Montgomery-Smith, et al. [64] that an increase of up to four orders of magnitude was seen. When $\boldsymbol{D_r}$ is set equal to zero Jeffery's equation which was defined in Equation 2.7 is achieved.

In Equation 2.13, $\boldsymbol{D_r}$ is introduced to diffuse the periodic fiber motion, which takes into consideration fiber-fiber interactions. Folgar and Tucker [16] introduced an Isotropic Rotary Diffusion (IRD) function which is given as

$$\boldsymbol{D_{IRD}} = 2C_I\dot{\gamma}(\boldsymbol{I}-3\boldsymbol{A}) \tag{2.17}$$

where $\boldsymbol{I}$ is the identity tensor, $\dot{\gamma}$ is the magnitude of the rate of deformation tensor defined as

$$\dot{\gamma} = \left(2(\Gamma:\Gamma)\right)^{\frac{1}{2}} \tag{2.18}$$

and C_I is an empirically derived interaction coefficient.

Several methods exist to estimate C_I, but for the results given in this dissertation the method of Bay [65] is used, which is given as

$$C_I = 0.018408e^{-0.714807^{V_f * l}_{d}} \tag{2.19}$$

where $V_f$is the volume fraction of fibers in the polymer feedstock.

The IRD method presented by Folgar and Tucker [16] has been shown to over predict the rate of fiber alignment; therefore, a more accurate model is needed. The reduced strain closure method (IRD-RSC), introduced by Wang, et al. [17] reduces the rate of fiber alignment using an empirical scaling parameter, κ, which ranges from 0 to1 dependent on the volume fraction of fibers in the fiber filled polymer flow. The IRD-RSC model is given as

$$D_{IRD-RSC} = -2(1-\kappa)(\mathbb{L} - \mathbb{M}:\mathbb{A}):\boldsymbol{\Gamma} + 2\kappa C_I\dot{\gamma} \tag{2.20}$$

where $\mathbb{L}$ and $\mathbb{M}$ are analytical functions of the eigenvalues and eigenvectors of $\boldsymbol{A}$ which are defined respectively as

$$\mathbb{L} = \sum_{i=1}^{3} \lambda_i(e_i e_i e_i e_i) \tag{2.21}$$

and

$$\mathbb{M} = \sum_{i=1}^{3} e_i e_i e_i e_i \tag{2.22}$$

In Equation 2.20, κ is an empirical scaling parameter that ranges from 0 to 1. When κ reaches 1 the model reduces to the Folgar-Tucker IRD model.

Phelps and Tucker [66] introduced anisotropic rotary diffusion (ARD) and the ARD-RSC method to reduce the rate of fiber alignment in fiber filled polymer flows. The ARD model is given as

$$\boldsymbol{D_{ARD}} = \dot{\gamma}[2\boldsymbol{C} - 2(tr\boldsymbol{C})\boldsymbol{A} - 5(\boldsymbol{C}\cdot\boldsymbol{A} + \boldsymbol{A}\cdot\boldsymbol{C}) + 10\mathbb{A}\!:\!\boldsymbol{C}] \tag{2.23}$$

and the ARD-RSC is defined as

$$\begin{aligned}\frac{\boldsymbol{DA}}{\boldsymbol{Dt}}_{ARD-RSC} &= (\boldsymbol{\Omega}\cdot\boldsymbol{A} - \boldsymbol{A}\cdot\boldsymbol{\Omega}) \\ &+ \lambda\{\boldsymbol{\Gamma}\cdot\boldsymbol{A} + \boldsymbol{A}\cdot\boldsymbol{\Gamma} - 2[\mathbb{A} + (1-\kappa)(\mathbb{L} - \mathbb{M}\!:\!\mathbb{A})]\!:\!\boldsymbol{\Gamma}\} \\ &+ \dot{\gamma}\{2[\boldsymbol{C} - (1-\kappa)\mathbb{M}\!:\!\boldsymbol{C}] - 2\kappa(tr\boldsymbol{C})\boldsymbol{A} - 5(\boldsymbol{C}\cdot\boldsymbol{A} + \boldsymbol{A}\cdot\boldsymbol{C}) \\ &+ 10[\mathbb{A} + (1-\kappa)(\mathbb{L} - \mathbb{M}\!:\!\mathbb{A})]\!:\!\boldsymbol{C}\}\end{aligned} \tag{2.24}$$

where $\boldsymbol{C}$ is a spatial tensor describing fiber-fiber interactions given as

$$\boldsymbol{C} = b_1\boldsymbol{I} + b_2\boldsymbol{A} + b_3\boldsymbol{A}^2 + \frac{b_4}{\dot{\gamma}}\boldsymbol{\Gamma} + \frac{b_5}{\dot{\gamma}}\boldsymbol{\Gamma}^2 \tag{2.25}$$

2.2.2 Closure Methods

The fiber orientation tensor model proposed by Advani and Tucker [12] has one inherent issue that must be considered. There exists an infinite series of even ordered tensors ($A_{ij}, \mathbb{A}_{ijkl}, \mathcal{A}_{ijklmn}$, ...) which must be truncated. Closure methods have been created in order to truncate the series which uses the second order orientation tensor to approximate the fourth order orientation tensor. Initial works with respect to closure methods included the linear [67] and quadratic [68] closure approximations. The linear closure approximation is simply a summation of all the products of $\boldsymbol{A}$ and δ, which is the Dirac delta function, given as

$$\widehat{\mathbb{A}} = -C_1\left(\delta_{ij}\delta_{kl} + \delta_{ik}\delta_{jl} + \delta_{il}\delta_{jk}\right) + C_2(A_{ij}\delta_{kl} + A_{ik}\delta_{jl} + A_{il}\delta_{jk} + A_{kl}\delta_{ij} + A_{jl}\delta_{ik} + A_{jk}\delta_{il}) \tag{2.26}$$

where C_1 and C_2 are constants defined respectively as 1/35 and 1/7 for three-dimensional orientation and respectively as 1/24 and 1/6 for two-dimensional planar constrained orientation.

The quadratic closure is defined as the product of the second-order orientation tensor given as

$$\widetilde{\mathbb{A}}_{ijkl} = A_{ij}A_{kl} \tag{2.27}$$

The linear closure is exact for a random fiber orientation distribution while the quadratic closure is exact for fully aligned fibers. Advani and Tucker [12] introduced the hybrid closure which combined the strengths of each method to approximate the fourth order orientation tensor which is given as

$$\overline{\mathbb{A}} = (1 - f)\widehat{\mathbb{A}} + f\widetilde{\mathbb{A}} \tag{2.28}$$

where f is an alignment parameter defined as

$$f = aA_{ij}A_{ji} - b \tag{2.29}$$

where a and b are respectively 3/2 and ½ for three-dimensional orientation and 2 and 1 for two dimensional planar fiber orientation states. The hybrid closure is shown to be an improvement across the orientation spectrum when compared to the linear and quadratic approximations.

The orthotropic fitted closure presented by Cintra and Tucker [69] provides an improvement to the hybrid closure. It is based on the idea that all fourth order tensor approximations must be orthotropic which is obtained when the principal axes match

those of the second order orientation tensor from which the fourth order tensor approximation is computed. The orthotropic fitted closure is given as

$$\overline{\mathbb{A}}^{ORT} = C_m^1 + C_m^2 A_{(1)} + C_m^3 \left[A_{(1)}\right]^2 + C_m^4 A_{(2)} + C_m^5 \left[A_{(2)}\right]^2 + C_m^6 A_{(1)} A_{(2)} \qquad (2.30)$$

where $m = 1{,}6$, $A_{(i)}$ are the eigenvalues of the second order orientation tensor, $\boldsymbol{A}$, and C_m are 18 independent coefficients that are computed using a minimization process that fits empirical data for the second order orientation tensor $\boldsymbol{A}$ for various homogeneous flow fields produced by Verwyst, et al. [15] and used by Wetzel, et al. [70]. Other similar process created by Verleye and Dupret [71], termed the Natural Closure, and Chung and Kwon [72], termed the Invariant Based Orthotropic Fitted closure use an orthogonality approach similar to the ORT closure method to approximate the fourth order orientation tensor, but in this dissertation the Orthotropic Fitted Closure is used.

2.2.3 Mechanical and Thermomechanical Property Evaluation

Fiber orientation effects the directionally dependent mechanical and thermomechanical properties in fiber filled polymers. The properties of fiber filled polymer composites has seen substantial study specifically in the area of unidirectional composites. Tucker and Liang [73] analyzed the popular models for predicting stiffness of unidirectional short fiber composites using a macromechanics representative volume element method and reported results of each model and which model produced the most accurate results. Several assumptions were made in the creation of the RVE finite element model which are stated as: fibers and matrix are linearly elastic, fibers and matrix are well bonded, the matrix is isotropic and the fibers are isotropic or transversely isotropic, and fibers are axisymmetric, identical in shape and size, and are characterized by and aspect ratio l/d. To describe the micromechanics models Tucker and Liang use

the method of Hill [74] to describe stress and strain concentration tensors, $\mathbb{A}$ and $\mathbb{B}$ which are given for the average stress and strain in the composite as

$$\bar{\varepsilon}^f = \mathbb{A}\bar{\varepsilon} \tag{2.31}$$

and

$$\bar{\sigma}^f = \mathbb{B}\bar{\sigma} \tag{2.32}$$

where $\mathbb{A}$ and $\mathbb{B}$ are fourth order tensors. An alternate strain concentration tensor is presented that relates the average fiber strain to the average matrix strain which is given as

$$\bar{\varepsilon}^f = \hat{\mathbb{A}}\bar{\varepsilon}^m \tag{2.33}$$

where m is a property of the matrix, and $\hat{\mathbb{A}}$ is related to $\mathbb{A}$ by

$$\mathbb{A} = \hat{\mathbb{A}}\left[(1 - v_f)\boldsymbol{I} + v_f\hat{\mathbb{A}}\right]^{-1} \tag{2.34}$$

In Equation 2.34, v_f is the volume fraction of fibers and $\boldsymbol{I}$ is the identity tensor. Liang then presents the average composite stiffness using the Voight assumption that the fiber and matrix undergo the same uniform strain given as

$$\boldsymbol{C}_V = \boldsymbol{C}^m + v_f(\boldsymbol{C}^f - \boldsymbol{C}^m) \tag{2.35}$$

and the compliance is given with the Reuss assumption that the fiber and matrix undergo the same uniform stress given as

$$\boldsymbol{S}_R = \boldsymbol{S}^m + v_f(\boldsymbol{S}^f - \boldsymbol{S}^m) \tag{2.36}$$

Tucker and Liang [73] first evaluated the work by Eshelby [75] for dilute suspensions which considers a single fiber in an infinite matrix. The strain concentration tensor for Eshelby's micromechanics model is given as

$$\mathbb{A}_E = [\boldsymbol{I} + \boldsymbol{E}\boldsymbol{S}^m(\boldsymbol{C}^f - \boldsymbol{C}^m)]^{-1} \tag{2.37}$$

where $\boldsymbol{E}$ is the Eshelby tensor. It is worth noting that the Eshelby approach is for dilute suspensions and accuracy decreases substantially for fiber volume fractions greater than 1% which is inappropriate for short fiber reinforced polymer flows.

The authors then analyzed the Mori and Tanaka [76] model which takes into consideration many identical particles in a matrix. The strain concentration tensor for the Mori and Tanaka model is given as

$$\mathrm{A}_{MT} = \mathrm{A}_E\left[\left(1 - v_f\right)\boldsymbol{I} + v_f\mathrm{A}_E\right]^{-1} \tag{2.38}$$

Tandon and Weng [77] derived explicit expressions for the elastic constants of a unidirectional short fiber polymer composite from the Mori and Tanaka model. Zhang [78] applied a closed form approach for transversely isotropic stiffness tensor which will be used in this dissertation. Tucker and Liang also analyzed the Halpin-Tsai [79] expressions which are commonly used for evaluation of the elastic constants of a unidirectional fiber filled composite as well as bounding and shear lag models, but found that the model of Mori and Tanaka models most accurately predicted the mechanical properties of a unidirectional short fiber composite.

The models discussed are given for uniaxially aligned short fiber filled composites which is not the case in extrusion or injection molding of fiber filled composites. The evaluation of mechanical and thermomechanical properties of misaligned fibers must, therefore; be analyzed using what is termed an orientation homogenization method. This method was originally proposed by Advani and Tucker [12], but was later derived using spherical harmonics by Jack and Smith [13]. This method takes into consideration a representative volume element of the fiber filled composite where the RVE is separated into smaller aggregates having unidirectional

alignment in the given aggregate. The aggregates are homogenized using a constant mean strain (Voight) approach or a constant mean stress (Reuss) approach across all aggregates. The stiffness of the RVE is simply the combined stress of the aggregates. Using the method of Jack and Smith [13] the stiffness can be written exactly as a function of fourth order and lower order orientation tensors. The stiffness equation is given as

$$\begin{aligned}\langle C_{ijkl}\rangle = {} & b_1\left(\mathbb{A}_{ijkl}\right) + b_2\left(\boldsymbol{A}_{ij}\delta_{kl} + \boldsymbol{A}_{kl}\delta_{ij}\right) \\ & + b_3\left(\boldsymbol{A}_{ik}\delta_{jl} + \boldsymbol{A}_{il}\delta_{jk} + \boldsymbol{A}_{jl}\delta_{ik} + \boldsymbol{A}_{jk}\delta_{il}\right) + b_4\left(\delta_{ij}\delta_{kl}\right) \\ & + b_5\left(\delta_{ik}\delta_{jl} + \delta_{il}\delta_{jk}\right)\end{aligned} \tag{2.39}$$

where $b_1 \rightarrow b_5$ are given as

$$\begin{aligned} b_1 &= C_{11} + C_{22} - 2C_{12} - 4C_{66} \\ b_2 &= C_{12} - C_{23} \\ b_3 &= C_{66} + \frac{1}{2(C_{23} - C_{22})} \\ b_4 &= C_{23} \\ b_5 &= \frac{1}{2(C_{22} - C_{23})} \end{aligned} \tag{2.40}$$

In Equation 2.40, C_{11}, C_{12}, C_{22}, C_{23}, and C_{66} are the elasticity tensor coefficients of the associated unidirectional short fiber composite.

Once the fourth order stiffness tensor for misaligned fibers is evaluated for the fiber filled composite the second order coefficient of thermal expansion tensor (CTE) can be evaluated for misaligned short fiber composites. The equation for the CTE defined by Camacho, et al. [80] is given as

$$\langle \alpha_{ij}\rangle = \langle C_{klmn}\alpha_{mn}\rangle\langle C_{ijkl}\rangle^{-1} \tag{2.41}$$

where $\langle C_{klmn}\alpha_{mn}\rangle$ is the double contraction of the transversely isotropic stiffness tensor with the transversely isotropic CTE tensor which is given as [80]

$$\langle C_{klmn}\alpha_{mn}\rangle = D_1 A_{ij} + D_2 \delta_{ij} \tag{2.42}$$

where D_1 and D_2 are given as

$$D_1 = a_1(b_1 + b_2 + 4b_3 + b_5) + a_2(b_1 + 3b_2 + 4b_3) \tag{2.43}$$

and

$$D_2 = a_1(b_2 + b_4) + a_2(b_2 + 3b_4 + 4b_5) \tag{2.44}$$

In Equations 2.43 and 2.44, a_1 and a_2 are defined as

$$a_1 = \alpha_{11} - \alpha_{22} \tag{2.45}$$

and

$$a_2 = \alpha_{22} \tag{2.46}$$

where α_{11} and α_{22} are the components of the transversely isotropic CTE tensor for a unidirectional composite in the x_1 and x_2 directions respectively. The α_{11} and α_{22} coefficients can be found using micromechanical theories for unidirectional composites. The method of Schapery [81] is used as it is defined by Stair and Jack [82].

It is worth noting that Fu, et al. [83] produced a method for evaluating the bulk coefficient of thermal expansion of a composite as well as the longitudinal component of CTE tensor, α_1, and the transverse component of the CTE tensor, α_2, which includes the effects of fiber length distribution and fiber orientation, both defined using probability density functions. Initially Fu, et al. [83] discuss the longitudinal and transverse thermal conductivity tensor components for unidirectional composites defined by Schapery [81] which are given as

$$\alpha_1^u = \frac{E_f \alpha_f v_f + E_m \alpha_m v_m}{E_f v_f + E_m v_m} \tag{2.47}$$

and

$$\alpha_2^u = (1 + v_f)\alpha_f v_f + (1 + v_m)\alpha_m v_m - \alpha_1^u (v_f V_f + v_m V_m) \tag{2.48}$$

where E_f is the Young's modulus of the fiber, E_m is the Young's modulus of the matrix, α_f is the coefficient of thermal expansion of the fiber, α_m is the coefficient of thermal expansion of the matrix, v_f is the Poisson's ratio of the fiber, v_m is the Poisson's ratio of the matrix, V_f is the volume fraction of fibers, and V_m is the volume fraction of matrix.

The reduced fiber Young's modulus, $\ddot{E}_f$ presented by Cox [84] is added to α_1^u represent short fiber reinforcement which is given as

$$\alpha_1^{sfrp} = \frac{\lambda \ddot{E}_f \alpha_f v_f + E_m \alpha_m v_m}{\lambda \ddot{E}_f v_f + E_m v_m} \tag{2.49}$$

where λ is defined as

$$\lambda = 1 - \frac{\tanh \frac{\eta l}{2}}{\frac{\eta l}{2}} \tag{2.50}$$

In Equation 2.50, l is the length of the fibers, and η is the shear lag parameter defined as

$$\eta = \sqrt{\frac{2G_m}{r_f^2 E_f \ln \frac{R}{r_f}}} \tag{2.51}$$

where G_m is the shear modulus of the matrix material, r_f is the radius of the fiber, and R is the mean separation of fibers normal to their lengths. α_2^u is unaffected by the reduced fiber modulus parameter and is thus unchanged in its form, $\alpha_2^u = \alpha_2^{sfrp}$.

The equations for the coefficient of thermal expansion of a uniaxial short fiber reinforced polymer along an angle θ are given as

$$\alpha_1 = \alpha_1^{sfrp} \cos^2\theta + \alpha_2^{sfrp} \sin^2\theta \tag{2.52}$$

and

$$\alpha_2 = \alpha_1^{sfrp} \sin^2\theta + \alpha_2^{sfrp} \cos^2\theta \tag{2.53}$$

The equations for the CTE of misaligned short fiber reinforced polymers are then given as

$$\alpha_1^{maf} = \int_{\theta=0}^{\frac{\pi}{2}} \int_{l=l_{min}}^{l_{max}} \left(\alpha_1^{sfrp} \cos^2\theta + \alpha_2^{sfrp} \sin^2\theta\right) f(l) g(\theta) dl d\theta \tag{2.54}$$

and

$$\alpha_2^{maf} = \int_{\theta=0}^{\frac{\pi}{2}} \int_{l=l_{min}}^{l_{max}} \left(\alpha_1^{sfrp} \sin^2\theta + \alpha_2^{sfrp} \cos^2\theta\right) f(l) g(\theta) dl d\theta \tag{2.55}$$

where $f(l)$ and $g(\theta)$ are the fiber length distribution and fiber orientation distribution, which are defined using a probability density function. It is stated that for two-dimensional analysis $g(\theta) = {}^{2}/_{\pi}$ and for three-dimensional analysis $g(\theta, \varphi) = g(\theta) g(\varphi) / \sin\theta = {}^{\pi}/_{2}$ and $g(\theta) = \sin\theta$. This method evaluates a scalar value for the longitudinal and transverse coefficient of thermal expansion, but for an anisotropic description α_{12}, α_{13}, α_{21}, α_{23}, α_{31}, and α_{32} are non-zero and must be evaluated.

To the authors knowledge the thermal conductivity for misaligned short fiber filled composites has not been derived via the orientation homogenization method to this point and will be shown later in this dissertation. However, substantial research has gone into evaluating the thermal conductivity of short fiber filled composites which will be discussed in detail in the following paragraphs.

Springer and Tsai [85] proposed micromechanical models for evaluation of the longitudinal, k_{11}, and transverse, k_{22}, thermal conductivities of a unidirectional fiber filled composites which was said to yield similar results to the work done by Thornburg and Pears [86]. In the analysis it was assumed that: a) the composites are macroscopically homogeneous, b) locally both the fiber and matrix are homogeneous and isotropic, c) the thermal contact resistance between the filament and matrix is negligible, d) the problem is two dimensional therefore the temperature distribution is independent of z, and e) the filaments are equal and uniform in shape and size and are axisymmetric. Using the transformation properties given by Carlslaw and Jaeger [87], Springer and Tsai [85] define the longitudinal thermal conductivity, k_{11} as

$$k_{11} = k_m \left[\left(\frac{v_f k_f}{k_m} \right) + v_m \right] \tag{2.56}$$

where k_m is the thermal conductivity of the matrix material, v_m is the volume fraction of matrix material, k_f is the thermal conductivity of the fibers, and v_f is the volume fraction of fibers.

Springer and Tsai also define the transverse thermal conductivity, k_{22}, for cylindrical fibers as

$$k_{22} = k_m \left[\left(1 - 2\sqrt{\frac{v_f}{\pi}} \right) + \frac{1}{B} \left[\pi - \frac{4}{\sqrt{1 - \left(\frac{B^2 v_f}{\pi} \right)}} \tan^{-1} \frac{\sqrt{1 - \left(\frac{B^2 v_f}{\pi} \right)}}{1 + \sqrt{\frac{B^2 v_f}{\pi}}} \right] \right] \tag{2.57}$$

where B is given as

$$B \equiv 2\left(\frac{k_m}{k_f} - 1\right) \tag{2.58}$$

It was stated that the given equations for the thermal conductivity components are accurate within 5% for fiber volume fractions up to 60%. Hasselman, et al. [88] evaluated the thermal conductivity of uniaxial carbon-fiber reinforced glass matrix composites at 0° and 45° orientations to analyze the effect of off axis thermal conductivity. The respective thermal conductivities in polar coordinates (z is considered constant) are given as

$$k_{zz} = k_p \cos^2\theta + k_n \sin^2\theta \tag{2.59}$$

$$k_{xx} = k_p \sin^2\theta + k_n \cos^2\theta \tag{2.60}$$

$$k_{xz} = \left(k_p - k_n\right) \sin\theta \cos\theta \tag{2.61}$$

where k_p and k_n are the principal thermal conductivities parallel and normal to the fiber direction respectively. It is also stated that the direction of the temperature gradient is not specifically in the direction of the applied temperature gradient as was initially stated by Nye [89], but instead follows a vector along the angle φ which is found using the defined equation

$$\tan\varphi = \frac{k_n}{k_p}\tan\theta \tag{2.62}$$

In another work by Hasselman [90] the thermal conductance in the interfacial area between the fiber and surrounding matrix is considered. This assumes that there is an interfacial area between the fiber and matrix that has a combination of the properties of the two phases. This very quickly complicates the evaluation of thermal conductivity and will not be considered in this dissertation. Instead the fiber will be assumed to be perfectly bonded with the matrix. Fu, et al. [83] analyzed the thermal conductivity of unidirectional fibers and expanded into misaligned fibers in short fiber reinforced

polymers. Initially the model of Halpin [79] for thermal conductivity in unidirectional short fiber reinforced polymers is presented where the longitudinal and transverse thermal conductivities are given as

$$k_1^{sfrp} = \frac{1 + 2\left(\frac{l}{d}\right)\mu_1 v_f}{1 - \mu_1 v_f} k_m \tag{2.63}$$

and

$$k_2^{sfrp} = \frac{1 + 2\mu_2 v_f}{1 - \mu_2 v_f} k_m \tag{2.64}$$

where l and d are the length and diameter of the respective fiber, and μ_1 and μ_2 are given as

$$\mu_1 = \frac{\frac{k_{f1}}{k_m} - 1}{\frac{k_{f1}}{k_m} + 2\frac{l}{d}} \tag{2.65}$$

and

$$\mu_2 = \frac{\frac{k_{f2}}{k_m} - 1}{\frac{k_{f2}}{k_m} + 2} \tag{2.66}$$

In Equations 2.65 and 2.66, k_{f1} and k_{f2} are the thermal conductivity of the fiber in the x_1 and x_2 directions. This is expanded to lamina that are oriented along an angle θ with respect to the x_1 axis as given by Choy, et al. [91]

$$k_1 = k_1^{sfrp} \cos^2\theta + k_2^{sfrp} \sin^2\theta \tag{2.67}$$

and

$$k_2 = k_1^{sfrp} \sin^2\theta + k_2^{sfrp} \cos^2\theta \tag{2.68}$$

which matches the k_{zz} and k_{xx} in Equations 2.59 and 2.60 given by Hasselman, et al. [88]. Fu, et al. [83] also present Nielsen's model [92] in their analysis, but due to complexity of the model and the very close results proceed with the Halpin model [79].

Fu, et al. [83] then derive the equations for misaligned short fiber reinforced composites in which the fiber orientation distribution and fiber length distribution are considered. The equations for the thermal conductivity of misaligned short fiber reinforced polymers are then given as

$$k_1^{maf} = \int_{\theta=0}^{\frac{\pi}{2}} \int_{l=l_{min}}^{l_{max}} \left(k_1^{sfrp} \cos^2\theta + k_2^{sfrp} \sin^2\theta\right) f(l) g(\theta) dl d\theta \tag{2.69}$$

and

$$k_2^{maf} = \int_{\theta=0}^{\frac{\pi}{2}} \int_{l=l_{min}}^{l_{max}} \left(k_1^{sfrp} \sin^2\theta + k_2^{sfrp} \cos^2\theta\right) f(l) g(\theta) dl d\theta \tag{2.70}$$

where $g(\theta)$ is evaluated in the same way as described for Equations 2.54 and 2.55. This method evaluates a scalar value for the longitudinal and transverse thermal conductivity, but for an anisotropic description k_{12}, k_{13}, k_{21}, k_{23}, k_{31}, and k_{32} are non-zero and must be evaluated.

2.3 Polymer Bonding in Extrusion Deposition Modeling

Polymer bonding between sequentially printed layers in LAAM and FFF manufacturing processes occurs via self-diffusion of polymer chains across the boundary after intimate contact has been achieved through polymer coalescence. Substantial research has gone into polymer bonding and coalescence between two similar polymeric materials and the closely related weld line analysis in injection molding and compression molding processes. Understanding the key bonding factors for the stated manufacturing

methods is necessary as this work applies post deposition compression and reheating of deposited polymer bead.

2.3.1 Polymer Interface Bonding

The analysis and measurement of weld line strength in injection molding studied by Kim and Suh [28] was reduced to pressure, melt temperature, and molecular orientation along the bond line for amorphous polymers. It was also stated that for crystalline polymers, which are common in FFF printing processes, size and distribution of the crystalline structure effect the bond line strength. The effect of molecular orientation is well understood and has been shown to effect mechanical properties of polymers by Curtis [93] who used the model of Griffith [94] to predict properties of highly aligned polystyrene and poly methyl methacrylate (PMMA). The viscoelastic nature of polymers is also stated to effect polymer chain entanglement and has been studied by Graessley [95] and more recently by Bellehumeur [23]. It is shown that models that do not take into account the viscoelastic effects of polymers and tend to over predict the rate of polymer chain diffusion and thus over predict the strength of the bond that is formed.

Ageorges et. al [96] summarized the creation of bond strength between two polymers in five steps: (1) surface rearrangement, (2) surface approach, (3) wetting, (2) diffusion, and (5) randomization [26, 27], which are shown in Figure 2.2.

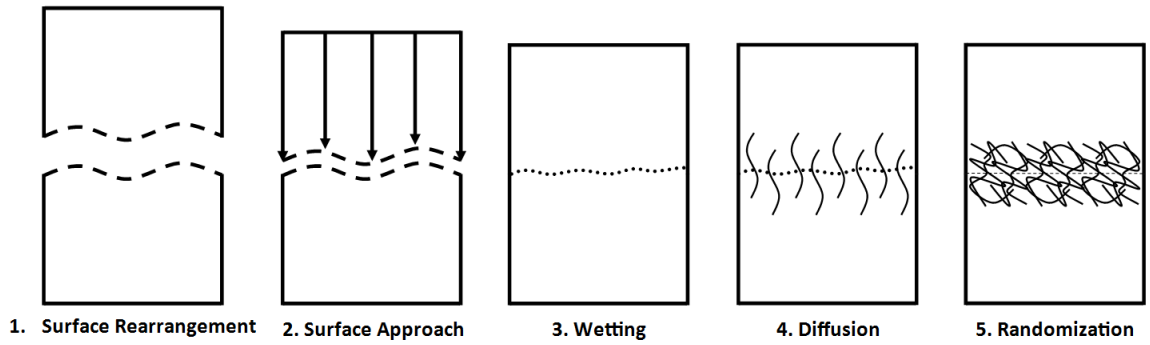

Figure 2.2. Bond Formation Steps

Surface rearrangement is the excitation of polymer chains through application of thermal energy. Surface approach is the joining of the two polymer bonding faces and wetting is the flow of molten polymer at the surface of the polymer-polymer interface at which time intimate contact is achieved at the bond line. Intimate contact which is described in detail by Dara [97] defines the amount of polymer interface that has achieved contact across which polymer chain entanglement can occur. Diffusion and randomization is dictated by reptation theory which for fiber filled matrices was described by de Gennes [25] as the motion of a polymer chain through a "tube" which confines the polymer chain to move along the length of the chain but due to the presence of other chains and fixed obstacles not in lateral motion, which is shown in Figure 2.3.

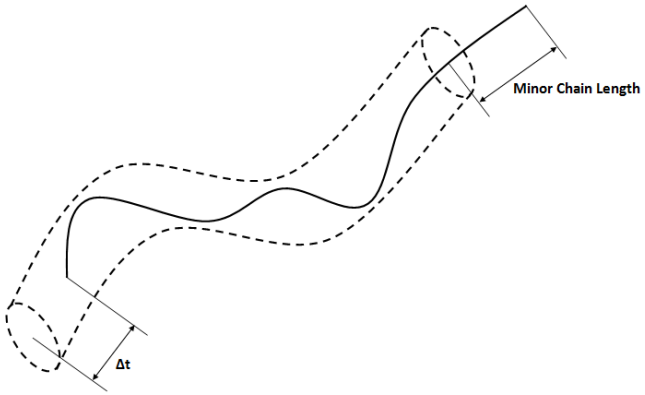

Figure 2.3. Reptation Time – Tube Chain Model

This model was used to define the strength of a polymer interface through reptation of polymer chains across a bonding surface by Wool, et al. [26, 27]. Wool used reptation theory to evaluate the fracture strength of a bonded polymer that had undergone autohesion or healing. The development of mechanical strength is given as [26, 27]

$$\frac{\sigma}{\sigma_\infty} \propto t^{\frac{1}{4}} M^{-\frac{3}{4}} \quad for\ t < t_r \tag{2.71}$$

where σ is the mechanical strength at time, t, σ_∞ is the mechanical strength for infinite time, M is the molecular weight of the amorphous polymer, and t_r is the reptation time for the given polymer. It is stated that this model is only effective for polymers with molecular weights in the range given as

$$M_C < M < 8M_C \tag{2.72}$$

where M_C is the critical entanglement molecular weight. Most polymers used in manufacturing have a molecular weight greater than the max given as $8M_C$, which merits further discussion.

Yang and Pitchumani [42] introduce a non-isothermal model for the interfacial polymer bonding of two like polymers. The authors first discuss the progression of polymer bond analysis via reptation theory. The authors define an equation for the degree of autohesion under isothermal conditions that is achieved in polymer bonding based on the models of de Gennes [25] and Prager and Tirrell [98] which is given as

$$D_h(t) = \frac{\sigma}{\sigma_\infty} = \frac{X}{X_\infty} = \left(\frac{l}{L}\right)^{\frac{1}{2}} \tag{2.73}$$

where X and X_∞ are the achieved interpenetration depth and maximum interpenetration depth of polymer chain which for the latter occurs at the reptation time, t_r, l is the minor chain length, which is the chain length that has escaped the tube, and L is the minor chain

length at reptation time, t_r, where the entire polymer chain has escaped the tube. The change in minor chain length with respect to time which is governed by a scalar diffusion coefficient due to isothermal conditions is given as

$$\frac{l}{L} = \left(\frac{t}{t_r}\right)^{\frac{1}{2}} \tag{2.74}$$

The degree of healing under isothermal conditions with respect to reptation time can then be represented as

$$D_h(t) = \frac{\sigma}{\sigma_\infty} = \left(\frac{t}{t_r}\right)^{\frac{1}{4}} \tag{2.75}$$

The reptation time in this case is said to be described by an Arrhenius equation given as

$$t_r = B_r e^{\left(\frac{A_r}{T}\right)} \tag{2.76}$$

where T is the temperature and A_r and B_r are experimentally determined coefficients. Bastien and Gillespie [41] extended the previous model to describe non-isothermal bonding of amorphous polymer laminates. In their model the time t as it ranges from $0 \rightarrow t_r$ was broken into a number of intervals, q, where

$$t_{i+1} - t_i = \Delta t = t/q \tag{2.77}$$

In Equation 2.77, the temperature is given as an isothermal value of the temperature average over the interval between time t_{i+1} and t_i, denoted as T_i^*, which defines the polymer diffusion rate and bond strength in terms of reptation theory under isothermal conditions, ${t^*}_r$. Using this model Equations 2.74 and 2.75 can be recast for incremental time as

$$\frac{\Delta l}{L} = \frac{t_{i+1}^{\frac{1}{2}} - t_i^{\frac{1}{2}}}{{t^*}_R^{\frac{1}{2}}} \tag{2.78}$$

and

$$D_H^{BG,MC}(t) = \left(\frac{l}{L}\right)^{\frac{1}{2}} = \left[\sum_0^{t/\Delta t}\left(\frac{t_{i+1}^{\frac{1}{2}} - t_i^{\frac{1}{2}}}{t^{*\frac{1}{2}}_R}\right)\right]^{\frac{1}{2}} \tag{2.79}$$

In the same way the incremental polymer bond strength formation is defined as

$$\frac{\Delta\sigma}{\sigma_\infty} = \frac{t_{i+1}^{\frac{1}{4}} - t_i^{\frac{1}{4}}}{t^{*\frac{1}{4}}_R} \tag{2.80}$$

and thus the degree of healing can be defined using the incremental polymer bond strength formation given as

$$D_H^{BG,SF}(t) = \frac{\sigma}{\sigma_\infty} = \left[\sum_0^{t/\Delta t}\left(\frac{t_{i+1}^{\frac{1}{4}} - t_i^{\frac{1}{4}}}{t^{*\frac{1}{4}}_R}\right)\right]^{\frac{1}{2}} \tag{2.81}$$

where $t^*{}_R$ is average the reptation time evaluated for the average interval temperature, T_i^*. This model more accurately describes the nonisothermal approach but relies on isothermal conditions for each interval, therefore; does not completely describe the non-isothermal evolution of properties in polymer welding. Sonmez and Hahn [99] produced an improvement in the non-isothermal modeling of polymer bonding to the previous model. To more accurately describe the minor chain growth the authors differentiate Equation 2.74 with respect to time given as

$$\frac{dl}{L} = \frac{dt}{2\sqrt{t_r t}} \tag{2.82}$$

Integrating Equation 2.82 and remembering that, $\sigma \approx \sqrt{l}$, the degree of healing equation can be written as

$$D_h^{SH}(t) = \frac{\sigma}{\sigma_\infty} = \left(\frac{l}{L}\right)^{\frac{1}{2}} = \left[\int_0^t \frac{d\tau}{2\sqrt{\tau t_r(\tau)}}\right]^{\frac{1}{2}} \tag{2.83}$$

where time, t, is the defined by an interval $(\tau, \tau + d\tau)$.

The integral in Equation 2.83 is only appropriate if the process is isothermal to reptation time, $t_r(\tau)$, from $t = 0$ to $t = \tau$. For this reason the process still does not represent the non-isothermal temperature history. Yang and Pitchumani [42] now present their non-isothermal model derivation for the interfacial polymer bonding of like materials. First the authors take into consideration the molecular weight issue described earlier with respect to critical molecular weight. It is stated that for polymers with molecular weights, $M > 8M_C$, that interpenetration depth, X, and minor chain length, l, do not have to reach X_∞ and L respectively for full healing to occur. From this point forward the authors represent terms of weld time, t_w, which is less than the reptation time, t_r. At this reduced time the interpenetration depth and fully reptated minor chain length are denoted as X_w and L_w. The non-isothermal healing development model is given generally as

$$\frac{\partial P}{\partial t} = D\frac{\partial^2 P}{\partial s^2} \tag{2.84}$$

where D is the time and temperature dependent diffusion coefficient, and P is a probability density function with respect to time, t, and position of a particular chain segment position at that time. The authors then set boundary conditions for Equation 2.84. The initial condition is stated for time, $t = 0$, the chain segment, s, is considered to be at its origin, $s = 0$, thus

$$P(s, 0) = \delta(0) \tag{2.85}$$

where δ is the Dirac delta function. Also, the domain is considered to be infinite which can be stated as $|s| \to \infty$, therefore; natural boundary conditions that must be satisfied are given as

$$P(s,t) = 0;\ \frac{\partial P(s,t)}{\partial s} = 0 \quad as\ |s| \to \infty \tag{2.86}$$

The authors then provide a lengthy derivation for non-isothermal analysis which has been abbreviated. The basis of non-isothermal healing of interfacial polymer bonding is given as

$$P(s,t) = \frac{1}{2\pi}\int_{-\infty}^{\infty} exp\left[\omega^2 \int_0^t -D(t)dt\right]\cos(\omega s)\, d\omega \tag{2.87}$$

where ω is the transformed variable in the frequency domain which was included due to use of a Fourier transformation in the derivation, $D(t)$ is the time and temperature dependent diffusion function given as

$$D(t) = \frac{L_w^2}{2t_w[T(t)]} \tag{2.88}$$

where weld time, t_w, is dependent on the temperature as a function of time during the bonding process. As defined with previous models the degree of healing during polymer bonding is given as

$$D_h^{PY}(t) = \left(\frac{l}{L_w}\right)^{\frac{1}{2}} = \left[\int_0^t \frac{1}{t_w(T)}\, dt\right]^{\frac{1}{4}} \tag{2.89}$$

In a follow-up article Yang and Pitchumani [100] include the effects of intimate contact on the non-isothermal interfacial polymer bonding and present the respective degree of bonding. Intimate contact requires consideration and measurement of the surface roughness of the bonding polymers, but for bonding of deposition printing is presented with models of polymer coalescence. It is worth noting that Yang and

Pitchumani [100] proposed a surface roughness model based on fractal geometry which is used in the derivation for the cited intimate contact model.

A similar model to the one proposed by Yang and Pitchumani [42] with respect to polymer bonding is presented by Ezekoye, et al. [101]. The significant differences in the models exists with the description of reptation time, t_r, versus weld time, t_w, and the use of radius of gyration versus minor chain length for polymer chain walking during bonding. Ezekoye, et al. [101] also represent surface roughness and intimate contact using terms via the method of contact resistance. An equivalent diffusion coefficient that evaluated the temperature change during welding with respect to time was proposed. The equivalent diffusion coefficient, $\overline{D}_s$ is given as

$$\overline{D}_s = \frac{1}{t_{m,max}} \int_0^{t_{m,max}} D_s(t_m, T) dt_m \tag{2.90}$$

where t_m is the time for which the interface is molten for semi crystalline polymers which could be related to the time above T_g, the glass transition temperature of amorphous polymers which ranges, $t_m = 0 \rightarrow t_{m,max}$, T is the interface temperature at time t_m. The percentage of maximum strength at a heal time of $t_{m,max}$, or the degree of healing D_h is then specified as

$$D_h^{ELFH} = \frac{\sigma(t_{m,max})}{\sigma_{max}} = \left(\frac{t_{m,max}}{t_r}\right)^{\frac{1}{4}} = \left(\frac{t_{m,max}\overline{D}_s}{R_g^2}\right)^{\frac{1}{4}} \tag{2.91}$$

where σ_{max} is the strength of the virgin polymer, and R_g is the radius of gyration for the given polymer.

2.3.2 Interlayer Adhesion of Polymer Deposited Beads

In polymer deposition additive manufacturing the effect of polymer sintering or polymer coalescence between two particles, or in the case of printing, two beads has been studied substantially in recent years. Polymer coalescence gives the rate of neck growth between two similar materials with respect to time and it is understood that polymer chain inter-diffusion can only occur in the neck area where intimate contact is achieved.

Polymer coalescence was originally studied by Frenkel [102] who determined the rate of neck growth between two contacting particles. The Frenkel model was then corrected by Eshelby [103] and the rate of neck growth is given as

$$\frac{x}{a} = \left(\frac{t\Gamma}{\eta a_0}\right)^{\frac{1}{2}} \tag{2.92}$$

where a is the particle radius, a_0 is the initial particle radius, t is sintering time, x is the sintering neck radius, Γ is the surface tension, and η is the viscosity. Bellehumeur, et al. [23] stated that the corrected Frenkel model is only accurate for early stages of polymer sintering. Pokluda, et al. [22] created a polymer coalescence model similar to the Frenkel model but took into consideration the change in particle neck radius with respect to time and the work of surface tension and work of viscous forces. The equation produced in the model by Pokluda, et al. [22] is given as

$$\theta' = \frac{\Gamma}{\eta a_0} \frac{2^{-\frac{5}{3}} \cos\theta \sin\theta \, (2 - \cos\theta)^{\frac{1}{3}}}{(1 - \cos\theta)(1 + \cos\theta)^{\frac{1}{3}}} \tag{2.93}$$

where θ is the angle between the center of the particle and the outermost point of the neck between particles which is shown in Figure 2.4. The neck growth for the Pokluda model can then be defined as

$$\frac{x}{a} = \sin\theta \tag{2.94}$$

Equation 2.94 ranges in value from 0 to 1, where 0 is at the time of contact where no coalescence has occurred, and a value of 1 occurs when the particles have fully coalesced and the sintering neck radius is equal to the combined particle radius which occurs when θ is equal to zero, shown in Figure 2.4 from Bellehumeur, et al. [23].

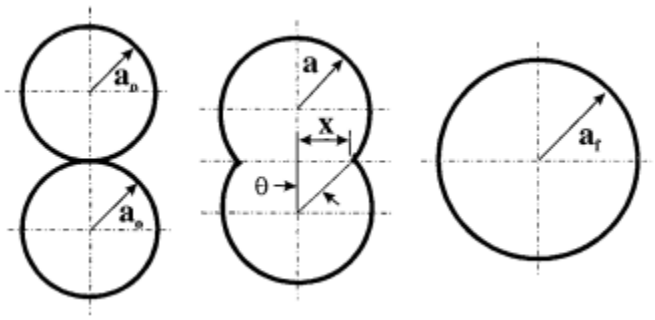

Figure 2.4. Polymer Particle Coalescence with Respect to Time

The previous models assume a Newtonian fluid, but neck growth has been experimentally shown to occur more slowly which is stated to be due to viscoelasticity of polymer particles. Bellehumeur, et al. [104] proposed a model that takes into consideration viscoelastic effects by adding Maxwell upper and lower convected models. The equation for sintering rate is given as

$$8(\alpha\lambda K_1\theta') + \left(2\alpha\lambda K_1 + \frac{\eta a_0}{\Gamma}\frac{K_1^2}{K_2}\right)\theta' - 1 = 0 \tag{2.95}$$

where K_1 and K_2 are defined as

$$K_1 = \frac{\sin\theta}{(1+\cos\theta)(2-\cos\theta)} \tag{2.96}$$

and

$$K_2 = \frac{2^{-\frac{5}{3}} \cos\theta \sin\theta}{(1+\cos\theta)^{\frac{4}{3}}(2-\cos\theta)^{\frac{5}{3}}} \tag{2.97}$$

In Equation 2.95 α is equal to 1, -1, or 0 which corresponds to upper, lower, and co-rotational derivative, and λ is the relaxation time of the polymer. This model shows improved accuracy with respect to rate of neck growth in coalescing polymers when compared to experimental results. Bellehumeur, et al. [23] applied the Newtonian coalescence model created by Pokluda, et al. [22] to neck growth predictions and bonding predictions for the FFF process. Good agreement was found between predicted strength values and experimental testing. Envelope temperature and deposition temperature were analyzed as print parameters and it was found that deposition temperature had a much larger effect on neck growth between filaments. It was found overall that filaments in FFF cannot fully bond due to rapid heat loss and low polymer volume which should be substantially different in LAAM polymer deposition. Bellehumeur, et al. [23] analyzed the heat transfer models of Li, et al. [30] and Rodriquez, et al. [29] by putting thermocouples in between printed layers and evaluating the temperature over time. It was found that the model of Li, et al. [30] was far more accurate immediately after deposition and for a short time afterwards whereas the model of Rodriguez, et al. [29] performed better at longer time scales. A similar experimental study was run with ranging deposition temperatures and envelope temperatures during deposition and similar results were found with respect to neck growth rates. Gurrala, et al. [24] extended the polymer coalescence model by Pokluda, et al. [22] to cylinders which represent coalescing beads deposited in the FFF print process. A similar derivation is completed to previous works with the major

difference being the surface area produced by the growth of the neck includes the bead length. The equation for rate of neck growth derived by Gurrala, et al. [24] is given as

$$\theta' = \frac{d\theta}{dt} = \frac{\Gamma}{3\sqrt{\pi} r_0 \eta}\left[\frac{[(\pi-\theta)\cos\theta + \sin\theta][\pi - \theta + \sin\theta\cos\theta]^{\frac{1}{2}}}{(\pi-\theta)^2 \sin^2\theta}\right] \tag{2.98}$$

where r_0 is the initial radius of the cylindrical bead. Experimental analysis showed an overshoot by the predictive model in tensile strength said to be due to different neck sizes at each layer because of different amounts of contained thermal energy and different heat transfer characteristics at each layer. It is also stated that the elliptical shape of the bead at deposition does not fully agree with the circular bead shape assumption.

The polymer coalescence approach has been applied to FFF printing processes for bond formation and strength growth between polymer filaments, but in order to accurately define neck growth rates and healing between deposited filaments an accurate heat transfer model is needed. Several approaches have been produced which will be analyzed in the next paragraphs.

Thomas and Rodriguez [29] presented a 2D transient heat transfer model for four stacked rectangular beads in the FFF print process. The governing equation is given as

$$\frac{\partial^2 T^*}{\partial x^2} + \frac{\partial^2 T^*}{\partial y^2} = \frac{1}{\alpha}\frac{\partial T^*}{\partial t} \tag{2.99}$$

where T^* is a normalized temperature given as

$$T^* = \frac{T - T_E}{T_E} \tag{2.100}$$

where T_E is the envelope temperature. Boundary and initial conditions are applied and the equation is then given as an eigenfunction expansion solution over the width of the bead is defined as

$$T_{ave}(x,y,t) = T_E + \frac{2T_E}{W}\sum_{m=1}^{\infty}\sum_{n=1}^{\infty}\left(\frac{\alpha_{mn}}{\beta_n}\sin(\lambda_m y)\cos\left(\frac{\beta_n W}{2}\right)\right)e^{-\alpha^2(\lambda_m^2+\beta_n^2)t} \quad (2.101)$$

where α_{mn} is given as

$$\alpha_{mn} = \frac{4T_L^*}{E_m^2 F_n^2 \lambda_m \beta_n}\sin\left(\frac{9\lambda_m H}{2}\right)\sin\left(\frac{\lambda_m H}{2}\right)\sin\left(\frac{\beta_n W}{2}\right) \quad (2.102)$$

In Equation 2.102 E_m^2 and F_n^2 are defined as

$$E_m^2 = \frac{1}{2}\left(5H - \frac{\sin(10\lambda_m H)}{2\lambda_m}\right) \quad (2.103)$$

and

$$F_n^2 = \frac{1}{2}\left(W + \frac{\sin(\beta_n W)}{\beta_n}\right) \quad (2.104)$$

In Equations 2.101-2.103 λ_m and β_n are given as

$$\lambda_m \cot(5\lambda_m H) = \frac{-h}{k} \quad (2.105)$$

and

$$\beta_n \tan\left(\frac{\beta_n W}{2}\right) = \frac{h}{k} \quad (2.106)$$

Finally, α^2 is defined as

$$\alpha^2 = \frac{k}{C_p \rho} \quad (2.107)$$

Li, et al. [30] proposed a lumped capacitance heat transfer model for deposition of FFF beads. In the analysis the beads are considered to be ellipses with cross sectional area and perimeter defined as

$$A = \pi ab \quad (2.108)$$

and

$$P = \pi(a+b)\left(\frac{64-3\lambda^4}{64-16\lambda^2}\right) \tag{2.109}$$

where λ is defined as

$$\lambda = \frac{a-b}{a+b} \tag{2.110}$$

In Equations 2.108-2.110, a and b are the major and minor axis of an ellipse. Li, et al. [30] assumes that conduction at the interface between two beads would not appreciably change the temperature of the foundation and thus heat transfer is considered to be in the form of convection. The energy balance equation given these assumptions is presented as

$$\rho CAv\frac{\partial T}{\partial x} = A\frac{\partial\left(k\frac{\partial T}{\partial x}\right)}{\partial x} - hP(T-T_\infty) \tag{2.111}$$

By applying the following boundary conditions

$$T = T_0 \; at \; x = 0 \; and \; t \geq 0 \tag{2.112}$$

and

$$T = T_\infty \; at \; x = \infty \; and \; t \geq 0 \tag{2.113}$$

the following equation for temperature with respect to time is given as

$$T = T_\infty + (T_0 - T_\infty \;)e^{-mx} \tag{2.114}$$

where m and x are

$$m = \frac{\sqrt{1+4\alpha\beta}-1}{2\alpha} \; and \; x = vt \tag{2.115}$$

In Equation 2.115 α and β are given as

$$\alpha = \frac{k}{\rho Cv} \tag{2.116}$$

and

$$\beta = \frac{hP}{\rho CAv} \tag{2.117}$$

It has been found that the model of Li, et al. [30] predict bead temperature with more accuracy immediately after deposition and the model of Rodriguez and Thomas [29] more closely predict temperature after longer cooling times. Compton, et al. [31] created a one dimensional heat transfer model using finite difference to evaluate the heat transfer of successively printed beads in a LAAM printing process. The energy balance equation used is given as

$$\dot{E}_{in} + \dot{E}_g = \dot{E}_{st} \tag{2.118}$$

where $\dot{E}_{in}$ is the rate of energy coming into the system, $\dot{E}_g$ is the rate of energy generation by the system defined as 0 for the given process, and $\dot{E}_{st}$ is the rate of change of energy stored in the print volume. In equation 2.118 $\dot{E}_{st}$ is defined as

$$\dot{E}_{st} = q_{cond} + q_{conv} + q_{rad} \tag{2.119}$$

where q_{cond}, q_{conv}, and q_{rad} are the rate of conduction, convection, and radiation in the system. Layers are considered infinite in length and temperature is considered constant through the thickness of the part and temperature is evaluated at three nodes per element in the vertical direction (bottom, middle, and top of respective layers). Average values were used for many of the temperature dependent properties and need further analysis to improve accuracy of the model. The purpose of this study was to evaluate the warping and delaminations in LAAM parts based on cooling rates of deposited thin wall structures. The heat transfer model was validated using infrared thermography of printed specimens to analyze temperature with respect to time which showed good agreement with the model. It was found that substantial differences in thermal conductivity in the model effect the predicted warping and delamination of printed parts due to accelerated

heat loss in the printed structure. Different thermal conductivity values also caused a change in the number of layers that were affected by the print bed temperature and addition of the top layer of molten polymer.

2.4 Additive Manufacturing Properties Improvement

Parameters that effect print quality and mechanical properties of Fused Filament Fabrication and Large Area Additive Manufacturing processes have seen substantial research over the last decade. Processing parameters, polymer additives, secondary polymer additions to feedstocks, and post deposition processing parameters have been analyzed to assess the possible improvements to the FFF and LAAM printing processes to increase industrial viability.

2.4.1 Process Parameter Optimization

Ahn, et al. [105] ran a design of experiments test that evaluated the effect of bead width, air gap, build temperature, raster orientation, and color of materials on mechanical properties of FFF printed ABS P400 parts. Tensile and compression tests were run to evaluate the effect of each print parameter on mechanical properties. It was found that air gap and raster orientation have a substantial effect on mechanical properties whereas bead width, print temp, and color of materials have little effect. For raster orientations of [$\pm$ 45°] and [0°/90°] optimum printing conditions resulted in ultimate tensile strengths of 65% and 72% of injection molded parts of the same ABS material. Sood, et al. [106] also ran a design of experiments for layer thickness, part build orientation, raster angle, air gap, and raster width using the Taguchi method to minimize the dimensional stability of printed parts. Optimum results were found using the Grey Taguchi method and artificial

neural networks. Optimum dimensional stability was found at a layer thickness of 0.254 mm, part orientation of 0°, raster angle of 0°, raster width of 0.4564 mm, and air gap of 0.008mm. Mohamed, et al. [107] evaluated six FDM printing parameters (air gap, raster angle, build orientation, layer thickness, road width, and number of contours) with respect to the effect on the mechanical performance of printed bars. DMA testing was done for each sample and the storage modulus, loss modulus, and mechanical damping value were recorded for the design of experiments. The influence of each parameter on the three properties evaluated were then used to find the optimum print parameters for the print process. The optimum parameters are layer thickness of 0.3302 mm, air gap 0 mm, raster angle 0°, build orientation of 0°, and 10 contours. Bayraktar, et al. [108] used artificial neural networks to predict the mechanical properties of 3d printed parts. The parameters used in the ANN model were also used to print specimens for testing. It was found that a -45 45 raster pattern produced the highest tensile strength. Lower print temperatures produced lower part strengths which was attributed to lack of polymer chain diffusion. It was found that the ANN model produced 0-6.44 percent deviation with respect to tensile testing results meaning reasonable part mechanical properties could be predicted before physically printing the parts.

Ning, et al. [109] analyzed the effects of raster orientation, print speed, layer height, and print temp on the tensile strength of 5% fiber filled ABS for FFF printed parts. It was shown that 0 90 raster pattern had a substantially larger ultimate tensile strength and Young's modulus and yield strength than -45 45 rasters. A print speed of 25mm/s, print temp of 220 °C, and 0.15 mm layer height was found to produce the best mechanical properties.

Many other parameter studies have been run in regard to improving mechanical and aesthetic properties of prints, but the improvement to properties based on printing parameters is limited to the inherent properties of the polymers being used to print. Others have sought improvement by adding second phase materials to the neat polymers. The inclusion of additives is discussed in the next section, but the orientation and distribution of the added particles will affect the amount of improvement and must be understood.

2.4.2 Multiple Materials Printing

Nikzad, et al. [1] analyzed the effect of the addition of copper and iron particles to the ABS polymer feedstock. The added materials ranged in size from 10 to 45 μm and in volume fractions of 5, 10, 20, 30, and 40%. It was found that notable changes in thermal conductivity did not occur until 20% volume fraction of copper and 30% volume fraction of iron particles. It was also noted that agglomerations and clogging occurred at large volume fractions. Mulholland, et al. [2] analyzed the addition of copper spheres and fibers to PA6 FFF printing materials and the resulting thermal conductivity of the printed specimens. It was found that at a volume fraction of 25% the thermal conductivity increased by 20% in the direction of printing. Micro-CT analysis also yielded fiber orientation results for the printed filled polymer, and it was found that orientations ranged from 0.7-0.8 in the printing direction for the analyzed samples. Tekinalp, et al. [3] analyzed the properties of LAAM printed parts with the addition of chopped carbon fiber to the ABS feedstock in weight fractions of 10, 20, 30, and 40% with an average length of 3.2 mm. The fiber filled ABS material was printed into dog bone specimens for tensile testing with the use of the BAAM system which employs a tamping mechanism. Fiber

orientation in the printed specimen was evaluated using the method produced by Velez-Garcia, et al. [110], and it was found that fiber orientation was highly aligned. A_{11} ranged from 0.915 for 10% weight fraction of fibers to 0.869 for 40% weight fraction, in the bead printing direction. The tensile strength increased 35% to 100% for weight fractions of 10-40% and modulus increased 400-700% for the printed tensile specimens in comparison to neat ABS specimens. Jiang, et al. [111] analyzed three short fiber filled polymers (PLA, ABS, and PETG) produced for FFF printing with print orientations of [0/90] and [$\pm$ 45]. It was found that the tensile strength and Young's modulus increased for all materials with the addition of carbon fiber, but results in reduced ductility. It was found that carbon fiber filled PETG saw the greatest improvements with the addition of carbon fiber.

2.4.3 Post Deposition Processing

Non-contact methods of heating a polymer-polymer bond interface have been studied at length for polymer joint welding. The area most critical to the work done in this dissertation is the method of infrared preheating of printed beads. Infrared heating for weld joints was originally studied by Potente, et al. [112] who evaluated IR welding in butt joined polymers. It was found that coloration and the addition of soot particles caused a decrease in penetration depth of infrared radiation and thus a smaller melt thickness layer. This is due to the decreased transmission and absorption index caused by pigments and second phase materials (soot). For equal melt layer thickness the soot filled material also was found to have a higher surface temperature which quickly reached the point of polymer degradation. Temperature of the irradiated surface also effects the amount of transmission and absorption of thermal energy from the infrared heater which

means the absorption is also dependent on irradiation time. It was advised that intermitting irradiation of the bonding surface be used to control the rate of heating. Grimm and Yeh [113] analyzed the infrared absorption and transmission of pigmented ABS polymers with a spectrum from red to blue as well as parts with carbon black added. It was found that for a quartz halogen lamp, which emits on a wavelength closer to the red end of the light spectrum, ABS with red pigment absorbed the most thermal energy. It is stated that for different lamps with varying emission wavelengths this could vary with the most absorption occurring in the most closely related pigment. Results similar to Potente, et al. [112] for the addition of carbon black were found where very small volume fractions substantially increased the absorption of thermal energy and quickly caused degradation of the polymer which must be controlled. Chen and Benetar [114] analyzed IR weld strength with a parameter study of the 3 bonding steps in IR welding of polymers. The steps are (1) IR heating of the joint surfaces, (2) change over time, (3) joining and cooling under pressure. IR heating time was varied and found to increase joint strength to an optimum point with increasing melt layer thickness, but for excessive heating times it was found that polymer degradation began to decrease joint strength. IR heater distance was evaluated and as expected greater heating time was needed for greater distances due to reduced flux density. Welding pressure was found to increase to an optimum point then decrease due to excessive squeezing out of the melt layer and the creation of adverse molecular orientation. Change over time or time between heating and intimate contact was varied and found to reach an optimum joint strength point and decrease as time increased.

The effect of infrared heating on polymer interfaces has been analyzed with respect to the FFF and LAAM printing process as well. Infrared and other preheating methods have been used to improve interlayer bonding. Ravi, et al. [32] applied an infrared laser heater to the FFF printing process reheating previously deposited layers before deposition of the new layer. A 2W laser attached to the extruder head was used to apply the infrared radiation. It was found that laser intensity increased flexural strength of the printed specimen up to 1W before seeing a decrease which was attributed to polymer degradation and surface damage to the printed bead. It was also found that flexural strength increased with increase in print speed until a pseudo-plateau occurred at print speeds at and above 4 mm/s. A 50% increase in flexural strength at optimum print speeds and laser intensity was found for the FFF printed specimens. Kusel [33] applied ultraviolet laser illumination to the previously printed layers to induce localized pre-deposition heating in FFF printing. Three print speeds were used (5, 10, and 15 mm/s) as well as four laser power settings for two applied lasers were used (0, 100, 200, 300, and 363 mW/laser) in the analysis. It was found that the addition of the ultraviolet laser led to a slight increase in the strength for each increase in irradiation power with a similar increase in strength as print speed was increased. This is attributed to more heat application with the laser and more retained heat with the increasing print speeds which increases polymer chain diffusion across the interlayer boundary. Kishore, et al. [20] applied infrared heating to the previously printed bead surfaces immediately before deposition of the next layer of fiber filled polymer to improve bonding between successively printed layers. Three test speeds (3.8, 5.1, and 7.6 cm/s), two infrared heater intensities (500W and 1000W), and three offset heights were used in the experiment. It

was shown that for the two slower print speeds IR heating increased fracture strength, but for the fastest print speed results were unchanged which is due to increased retained heat between depositions of the next bead. It was found for increased heater intensities and the lowest offset height that fracture energy decreases due to degradation of the printed polymer.

It is worth noting that other methods have been produced to improve interlayer bonding and have seen different levels of improvement. Partain [34] used forced air pre-deposition heating similar to that used in PVC welding to improve interlayer bonding in FFF printed parts. The work was largely unsuccessful due to very little to no increase in part strength and substantial issues with part deformation at high airflow rates. Shih, et al. [115] studied the effects of cold plasma treatments and mechanical polishing on interlayer bond strength in PLA FFF printed parts by increasing the wettability of the printed bead surface. It was found that interlayer bonding increased substantially with cold plasma treatment where 30 s treatment times increased fracture strength by 134% and treatment times of 300 s increased fracture strength by 63%. The reduced effectiveness of the 300 s cold plasma treatment time was said to be due to the creation of an over-oxidized layer at the top of the treated bead, and treatment time optimization was needed to produce the best results. Mechanical polishing was found to only slightly increase bond strength (approximately 8%) due to increasing the surface roughness of the bead reducing wettability.

The BAAM printer used at Oak Ridge National Labs is equipped with a z-tamping device which oscillates up and down compressing the layer immediately after deposition. This method has been shown to improve strength in the z direction by

increasing intimate contact area between successively deposited beads [10, 20]. It also has been shown to decrease the area of intralayer voids in the printed part.

The previous methods of interlayer bond improvement are all done during printing of the materials, but post print methods have also been produced and are now discussed. Hart, et al. [116] applied post print annealing in a fitted mold for FFF printed parts to promote interlayer bonding. Parts were annealed at temperatures from 75 °C to 175 °C with annealing times ranging from 2 to 168 hours. It was found with the most aggressive annealing parameters that fracture strengths of printed and annealed parts increased 2700% when compared with non-annealed specimens. It was found that all parts decreased in volume during annealing due to void reduction in which trapped air was forced out due to weight of the polymer on itself. Interlayer bonding was also analyzed for printed and annealed parts and it was found that the model of Rodriguez and Thomas [29] most accurately predicted fracture strength. It was stated that intimate contact is low in in FFF printing and the use of a pressure roller or similar device could have substantial effects on degree of intimate contact between successively printed layers by both smoothing the printed surface and applying pressure to the interlayer contact point which has been shown to improve bond strength. Sweeny, et al. [117] studied the effects of adding multiwall carbon nanotube coated PLA FFF feedstocks and post print microwave irradiation of the parts. Weight fractions of carbon nanotube coatings were evaluated from 0 to 20% to find optimal loadings for irradiation properties which was found to be at 10%. Printed parts were irradiated for 60 seconds in a chamber that was held at 160 °C. An increase of 275% in fracture strength was found using microwave irradiation when compared to untreated printed parts.

To the authors knowledge patterning of the print surfaces has not been completed in the FFF or LAAM printing processes to this point but it is expected that creating a mechanical interlock between layers will improve interlayer strength. Patterning of bonding surfaces has however been applied in aerospace structural applications and the results have been positive. Lee, et al. [35] analyzed the effect of micro patterning of surfaces for adhesive joints between dissimilar materials on adhesive bond strength. Pattern sizes ranged from 1:1 to 10:1 for experimental testing where the first number is the width of the cut portion of the pattern and the second number is the width of the ridge between cuts. It was found that the 10:1 ratio had a fracture strength 37% greater than the 1:1 ratio and results followed a linear increase with respect to pattern ratio. A finite element model was created to predict fracture strength in patterned surfaces and was found to be accurate within 8% of the experimental results. The pattern used in this paper was simply linear cuts with constant radius perpendicular to the loading direction. Other studies [36-40] focused on different pattern layouts for increased adhesion using micro patterning.

CHAPTER THREE

Planar Deposition Flow Modeling of Fiber Filled Composites in Large Area Additive Manufacturing

This chapter published as: Heller, B.P., Smith, D.E., Jack, D.A., Planar deposition flow modeling of fiber filled composites in large area additive manufacturing, Additive Manufacturing, 25, pp. 227-238, January 2019

There has been substantial study in the area of polymer extrusion [44-54] and specifically polymer extrusion in additive manufacturing processes [5-9] over the last decade. Bellini, et al. [18] produced a two-dimensional planar deposition model for an FFF nozzle but focused on the start and stop characteristics of deposition disregarding steady state deposition. Bellini, et al. [18] also neglected the effect of filler particles during deposition and the model was for small scale deposition of ceramic materials. In this study, three deposition flow domains representing different nozzle configurations, as a function of the relative nozzle height above the print bed are considered for a LAAM printing nozzle. Fiber orientation is computed throughout the flow domain and the resulting fiber orientation state is used to compute mechanical properties and the coefficient of thermal expansion of the deposited bead. A fourth flow configuration, that of a nozzle without a deposition plate, is also evaluated using the same simulation approach to provide insight into the effect of polymer deposition on bead mechanical and thermomechanical properties.

3.1 Deposition Flow Modeling in Large Area Additive Manufacturing

In this study, the motion of the polymer melt flow is modeled as two-dimensional planar Stokes flow of a Newtonian fluid. The polymer flow is defined as a low Reynolds number flow with high viscosity which is standard for polymer flow models [118]. Equations of mass and momentum conservation for Stokes flow of an incompressible Newtonian fluid are given as

$$\nabla \cdot \mathbf{v} = 0 \tag{3.1}$$

and

$$\nabla \cdot \boldsymbol{\sigma} = 0 \tag{3.2}$$

where $\mathbf{v}$ is the velocity vector and $\boldsymbol{\sigma}$ is the stress tensor written as

$$\boldsymbol{\sigma} = -p\boldsymbol{I} + \mu[(\nabla \mathbf{v}) + (\nabla \mathbf{v})^{\mathrm{T}}] \tag{3.3}$$

In Equation 3.3, p is the pressure, $\boldsymbol{I}$ is the identity tensor, μ is the Newtonian fluid viscosity. The shape of the extrudate after leaving the nozzle is based on the stress state in the polymer melt flow and along the extrudate surface. The extrudate swell curves are defined so the boundary stress is equal to zero as

$$\boldsymbol{\sigma} : [\mathbf{nn}] = 0 \tag{3.4}$$

where ":" indicates the double contraction of the stress tensor with the outer product of the normal vector with itself, giving the stress traction along the free surface. Free surfaces can be specified as a zero penetration boundary where the normal velocity is set to zero along the surface or a zero surface tension boundary where the normal stress along the surface is set to zero [46] as in Equation 3.4.

The polymer melt domain in our work is based on the nozzle geometry of the Strangpresse Model 19 Large Area Additive Manufacturing extruder [19] operating at

normal plate speed printing conditions shown in Figure 3.1. The Strangpresse Model 19 is capable of depositing up to 19 pounds of material per hour with typical relative deposition plate speeds of $v_x = 101.6\ mm/s$. Figure 3.1 shows the geometry of the Strangpresse Model 19 nozzle used in this work.

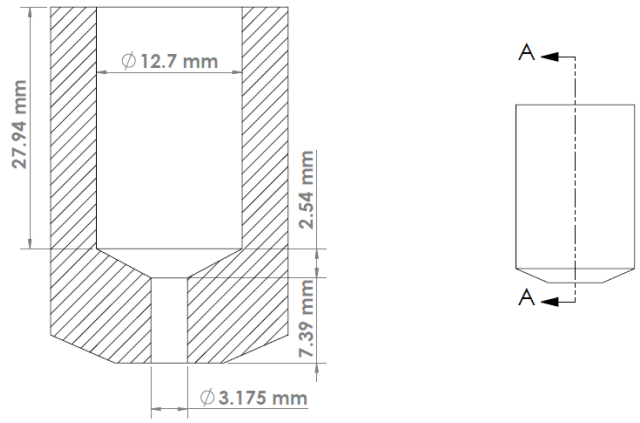

Figure 3.1. Strangpresse Model 19 Nozzle Cross Section, Geometry, and Dimensions

The extruded material, and the boundary conditions used to define the flow field during deposition process simulation are shown in Figure 3.2, (A) and (B). The bead height and nozzle height are shown in the figure as $h_b = 3$ mm and h_n, respectively. Three nozzle heights, h_n, are chosen to represent various polymer deposition conditions. The three flow models are designated as 1) *level flow* ($h_b = h_n$) where the nozzle is at the same height as the printed bead that it is producing, 2) *falling flow* ($h_b < h_n$) which represents the deposition of the polymer when the nozzle is above the deposited bead height, and 3) *bull nose flow* ($h_b > h_n$) where the nozzle is pressed into the flow creating a 'nose' in front of the nozzle and an expansion upward to the bead height behind the nozzle. The three nozzle heights studied are 2.5 mm for bull nose flow, 3 mm for level flow, and 4 mm for falling flow.

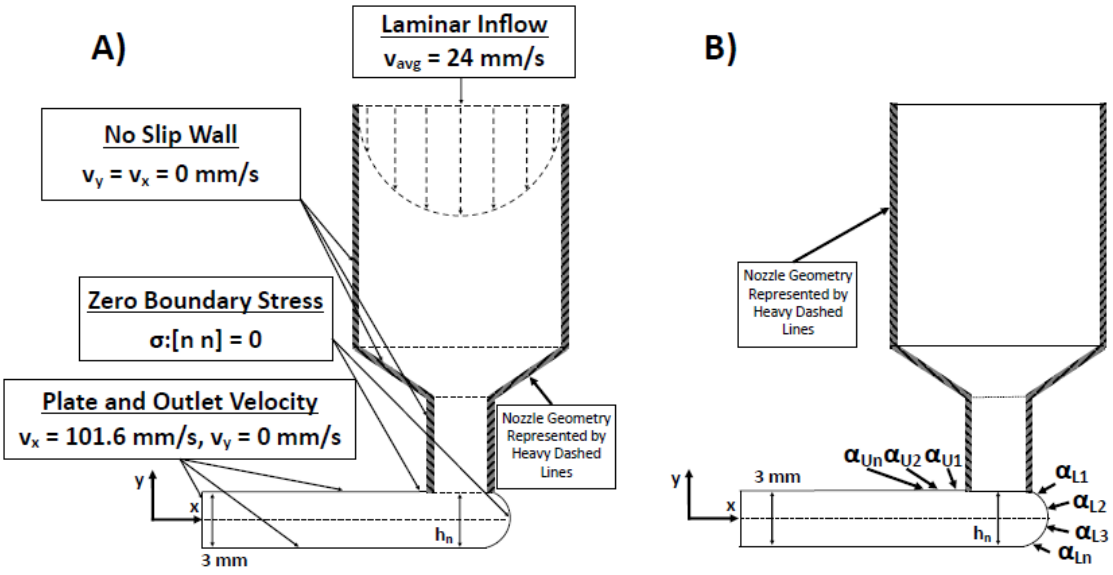

Figure 3.2. A) Boundary Conditions, B) Design Variables for the Deposition Flow Model

The value of the Newtonian viscosity, μ, in our flow simulations is 817 Pa·s, which is evaluated from a Carreau-Yasuda model for ABS at 230 °C and a shear rate of 100 s^{-1}, both typical parameters used in the LAAM process. In addition, the fluid density is ρ = 1154 kg/m^3 [118]. The outlet and plate velocities are set to be $v_x = 101.6\ mm/s$, which along with the volumetric flow rate defined at the inlet defines the deposited bead height for the deposition flow models. For the deposition flow simulations in Figure 3.2, (A), the lower surface of the extruded bead is moving at a velocity v_x with $v_y = 0\ mm/s$. The inlet of the nozzle is defined as a fully developed laminar flow profile with an average velocity, $v_{avg} = 24\ mm/s$ in all simulations. The polymer melt flow is assumed to have a no-slip boundary within the nozzle which is defined as $v_x = v_y = 0\ mm/s$.

In this study we also include the straight flow extrudate model shown in Figure 3.3 (A) and (B) as a reference to better understand the effect that the deposition process has on fiber orientation in the bead and the resulting mechanical properties.

The flow model for the straight flow is defined in a similar manner to that described above for the deposition flows except that the polymer melt flow is allowed to proceed downward without contacting a moving print plate. A zero-pressure boundary is assumed at the flow domain exit which represents the absolute pressure as shown in Figure 3.3 (A) and gravity is ignored. The design variables for the straight flow model are shown in Figure 3.3 (B).

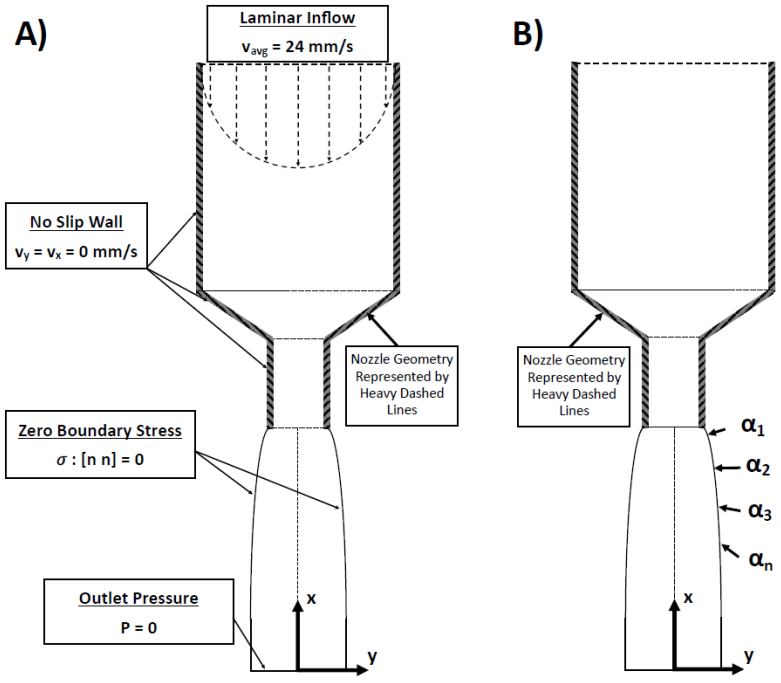

Figure 3.3. A) Boundary Conditions and, B) Design Variables for Straight Flow Model

3.2 Shape Minimization of Extrudate Surfaces

The shape of the polymer extrudate immediately outside of the nozzle is evaluated by minimizing the integrated squared normal velocity on the leading and upper curves where the zero boundary stress condition is prescribed. The minimization method presented is computed using the fmincon function in Matlab which is utilizing the interior point minimization algorithm. The optimization for computing the shape of the free surface is

$$\min_{\underline{\alpha}} f(\underline{\alpha}) = \frac{1}{l_S} \int_{S(\boldsymbol{\alpha})} \big(u(\alpha) \cdot n(\alpha)\big)^2 dS = 0 \tag{3.5}$$

where $S(\boldsymbol{\alpha})$ is defined as the union of the upper and lower surfaces defined as

$$S(\boldsymbol{\alpha}) = S_U \cup S_L \tag{3.6}$$

In Equation 3.5, the vector $\underline{\alpha}$ contains the design variables which define the geometric location, (x and y coordinates), of points along the two boundary surfaces $S(\boldsymbol{\alpha})$ as shown in Figure 3.2 (B), and l_S is the length of the free surface defined by the design variables. The square of the normal velocity along the two boundaries shown in Equation 3.5 is evaluated at each iteration of the minimization. We define the extrudate free surfaces, $\underline{\alpha}$, using an n[th] order Bezier curve whose recursive equation is defined as [119]

$$B(t) = (1-t)^n \mathbf{P}_0 + \binom{n}{1}(1-t)^{n-1} t\mathbf{P}_1 + \cdots + \binom{n}{n-1}(1-t)t^{n-1}\mathbf{P}_{n-1} + t^n \mathbf{P}_n \tag{3.7}$$

The Bezier curve is a parametric equation, therefore; the parametric variable, t, defined in Equation 3.7 ranges from 0 to 1. In Equation 3.7, $\mathbf{P}_i$ are the control points and the binomial coefficients which follow Pascal's triangle are given as

$$C_m^k = \frac{m!}{k!\,(m-k)!} \tag{3.8}$$

In our approach, the design variables in the vector $\underline{\alpha}$ define the location of the control points $\mathbf{P}_i$ such that when Equation 3.5 is solved, the position of the free surface control points define the extrudate shape.

Minor differences exist in the optimization problem between the deposition flow and straight flow models. Given the symmetry of the straight flow problem, the design variable vector $\underline{\alpha}$ in Equation 3.5 only defines one side of the extrudate domain as shown in 3.3, (B). The opposite side of the flow domain is defined through symmetry along the centerline.

3.3 Fiber Orientation in the Planar Flow Deposition Model

Once the flow domain has been defined and the melt flow velocity field has been computed, fiber orientation is computed along ten streamlines using the velocity and velocity gradients from the flow simulation.

Polymer melt flow fiber orientation simulations are typically based on the pivotal work by Jeffery [62] who first defined the periodic tumbling motion of a single ellipsoid in viscous incompressible fluid flow. Based on his work, the motion of a single fiber undergoing these conditions is defined through

$$\frac{D\mathbf{p}}{Dt} = \boldsymbol{\Omega} \cdot \mathbf{p} + \boldsymbol{\lambda}(\boldsymbol{\Gamma} \cdot \mathbf{p} - \boldsymbol{\Gamma} : \mathbf{ppp}) \tag{3.9}$$

where $\mathbf{p}$ is the unit vector along the fibers principal axis, $\boldsymbol{\Omega}$ is the vorticity tensor defined as

$$\boldsymbol{\Omega} = \frac{1}{2}[(\nabla \mathbf{v}) - (\nabla \mathbf{v})^T] \tag{3.10}$$

and $\boldsymbol{\Gamma}$ is the rate of deformation tensor given as

$$\boldsymbol{\Gamma} = \frac{1}{2}[(\nabla \mathbf{v}) + (\nabla \mathbf{v})^T] \tag{3.11}$$

The parameter λ is related to fiber geometry as

$$\lambda = \frac{\beta^2 - 1}{\beta^2 + 1} \tag{3.12}$$

where β is the equivalent ellipsoidal fiber aspect ratio which is calculated for a cylindrical fiber as (see e.g., Zhang [63])

$$\beta = 0.000035\xi^3 - 0.00467\xi^2 + 0.764\xi + 0.404 \tag{3.13}$$

In Equation 3.13, ξ, is the geometric aspect ratio defined as

$$\xi = \frac{l}{d} \tag{3.14}$$

where l is the length, and d is the diameter of the short carbon fiber.

Direct implementation of Jeffery's approach for short fiber composites is prohibitive since each of the thousands of individual suspended fibers need to be evaluated separately. Furthermore, Equation 3.9 is limited to dilute suspensions which is not the case in short fiber LAAM composites. Folgar and Tucker [16] proposed a fiber orientation probability density function, $\psi(\mathbf{p})$, to represent a large number of interacting fibers which evolves through time following

$$\frac{d\psi}{dt} = -\nabla \cdot \mathbf{p}\big((\boldsymbol{\Omega} \cdot \mathbf{p} + \lambda \boldsymbol{\Gamma} \cdot \mathbf{p} - \lambda \boldsymbol{\Gamma} : \mathbf{ppp})\psi(\mathbf{p})\big) + \boldsymbol{D_r} \tag{3.15}$$

In Equation 3.15, $\boldsymbol{D_r}$ is a function introduced to diffuse the periodic fiber motion, providing a means to account for fiber-fiber interactions. Folgar-Tucker [16] introduced an Isotropic Rotary Diffusion (IRD) function written as

$$D_r = C_I \dot{\gamma} \tag{3.16}$$

where $\dot{\gamma}$ is the scalar magnitude of the rate of deformation tensor defined as

$$\dot{\gamma} = \left(2(\boldsymbol{\Gamma}:\boldsymbol{\Gamma})\right)^{\frac{1}{2}} \tag{3.17}$$

and C_I is the empirically derived interaction coefficient. There exist several methods to estimate C_I, but for the current work we use the method presented by Bay [65] where C_I is evaluated as

$$C_I = 0.018408e^{-0.714807\frac{V_f * l}{d}} \tag{3.18}$$

and V_f is the volume fraction of fibers in the polymer feedstock.

Unfortunately, solving for the probability density function with Equation 3.15 is computationally prohibitive for large flow fields of practical interest such as those seen in LAAM printing. Therefore, we apply the computationally efficient orientation tensor approach first introduced by Advani and Tucker [12] with the Folgar-Tucker [16] IRD function to evaluate the second order orientation tensor along streamlines through the fluid domain by numerically evaluating (cf. Advani and Tucker [12])

$$\frac{D\boldsymbol{A}}{Dt} = -(\boldsymbol{\Omega}\cdot\boldsymbol{A} - \boldsymbol{A}\cdot\boldsymbol{\Omega}) + \lambda(\boldsymbol{\Gamma}\cdot\boldsymbol{A} + \boldsymbol{A}\cdot\boldsymbol{\Gamma} - 2\mathbb{A}:\boldsymbol{\Gamma}) + 2C_I\dot{\gamma}(\boldsymbol{I} - 3\boldsymbol{A}) \tag{3.19}$$

where $\boldsymbol{A}$ and $\mathbb{A}$ are the second and fourth order orientation tensors, respectively given as

$$\boldsymbol{A}_{ij} = \oint_S p_i p_j \psi(\mathbf{p}) d\boldsymbol{p} \tag{3.20}$$

and

$$\mathbb{A}_{ijkl} = \oint_S p_i p_j p_k p_l \psi(\mathbf{p}) d\boldsymbol{p} \tag{3.21}$$

Note that the fourth order orientation tensor, $\mathbb{A}$, is needed in Equation 3.19 to compute $\boldsymbol{A}$ as a function of time. Unfortunately, the equation of motion for $\mathbb{A}$ contains the sixth-order orientation tensor (not shown), and every even ordered orientation tensor

equation of motion contains the next higher even ordered orientation tensor. This necessitates the use of a closure whereby a higher ordered tensor is approximated as a function of lower ordered tensors. In the current study we employ the orthotropic fitted closure (ORT) due to its computational stability and efficiency. The ORT closure [14,15] computes $\mathbb{A}$ from the eigenvalues $\lambda_i, i = 1,2,3$, of the second order orientation tensor, $\boldsymbol{A}$, using 45 independent coefficients to obtain the approximate fourth order orientation tensor that are computed using a minimization process that fits computed values of $\boldsymbol{A}$ for various homogeneous flow fields. The orthotropic fitted closure is given as [14, 15]

$$\overline{\mathbb{A}}^{ORT} = C_m^1 + C_m^2 A_{(1)} + C_m^3 \left[A_{(1)}\right]^2 + C_m^4 A_{(2)} + C_m^5 \left[A_{(2)}\right]^2 + C_m^6 A_{(1)} A_{(2)} \qquad (3.22)$$

where $m = 1,6$.

It is worth noting that an important property of $\boldsymbol{A}$ is that its trace equates to unity. It follows that a fiber orientation state for a uniformly random distribution yields a tensor $\boldsymbol{A}$ with components equal to zero except the main diagonal which has values of $\boldsymbol{A}_{ii} = {}^1/_3$ where $i = 1,2,3$ (no summation implied). Similarly, an orientation tensor $\boldsymbol{A}$ for fibers perfectly aligned in the x or y direction would yield all diagonal components having a value of zero except $A_{11} or\ A_{22} = 1$. To better illustrate the angle of fiber alignment, we compute the angle formed between the tangential velocity vector along the given streamline, $\mathbf{v}_t$, and the principal eigenvector of the second order orientation tensor $\boldsymbol{A}$ at that same point. The angle of alignment θ is evaluated as

$$\theta = \left(\cos^{-1} \frac{\mathbf{v}_t \cdot \mathbf{e}^{(\lambda_m)}}{\sqrt{\mathbf{v}_t \cdot \mathbf{v}_t} \sqrt{\mathbf{e}^{(\lambda_m)} \cdot \mathbf{e}^{(\lambda_m)}}} \right) \frac{180}{\pi} \qquad (3.23)$$

Note that in Equation 3.23, $\mathbf{e}^{(\lambda_m)}$, defines the vector along the principal fiber direction at a point. Equation 3.23 quantifies the angle of overall misalignment of fibers

as compared to the direction of the fluid velocity which is helpful as the polymer melt flow changes direction during deposition.

3.4 Elastic Property Evaluation in the Planar Flow Deposition Model

Once the fiber orientation within the fluid domain is computed, mechanical and thermomechanical properties of the fiber filled polymer can be evaluated using the orientation homogenization method introduced by Advani and Tucker [12] and derived by Jack and Smith [13]. This approach considers the composite as a set of similar representative volume elements, each with its own unidirectional fiber alignment. The aggregates are homogenized using a constant mean strain (Voigt) or constant mean stress (Reuss) approach [74]. The stiffness of the composite is then defined as the combination of the stiffness's of the homogenized RVE's. The stiffness matrix computed by the orientation homogenization method is written as

$$\begin{aligned}\langle C_{ijkl}\rangle = {} & b_1\left(\mathbb{A}_{ijkl}\right) + b_2\left(\boldsymbol{A}_{ij}\delta_{kl} + \boldsymbol{A}_{kl}\delta_{ij}\right) \\ & + b_3\left(\boldsymbol{A}_{ik}\delta_{jl} + \boldsymbol{A}_{il}\delta_{jk} + \boldsymbol{A}_{jl}\delta_{ik} + \boldsymbol{A}_{jk}\delta_{il}\right) + b_4\left(\delta_{ij}\delta_{kl}\right) \\ & + b_5\left(\delta_{ik}\delta_{jl} + \delta_{il}\delta_{jk}\right)\end{aligned} \tag{3.24}$$

Where $b_1 \rightarrow b_5$ are given as

$$\begin{aligned} b_1 &= C_{11} + C_{22} - 2C_{12} - 4C_{66} \\ b_2 &= C_{12} - C_{23} \\ b_3 &= C_{66} + \frac{1}{2(C_{23} - C_{22})} \\ b_4 &= C_{23} \\ b_5 &= \frac{1}{2(C_{22} - C_{23})} \end{aligned} \tag{3.25}$$

In Equation 3.25, C_{11}, C_{12}, C_{22}, C_{23}, and C_{66} are the elasticity tensor coefficients of the associated unidirectional short fiber composite, which we calculate using the Tandon-Weng [77] approach, and $\langle C_{ijkl} \rangle$ is the stiffness tensor represented by the homogenization of the RVE's.

3.5 Thermomechanical Property Evaluation in the Planar Deposition Flow Model

A similar method can be used to evaluate the coefficient of thermal expansion (CTE) of a composite composed of short misaligned fibers, which is given by Camacho, et al. [80] as

$$\langle \alpha_{ij} \rangle = \langle C_{klmn} \alpha_{mn} \rangle \langle C_{ijkl} \rangle^{-1} \tag{3.26}$$

where $\langle C_{ijkl} \rangle$ is the stiffness tensor given in Equation 3.24. The $\langle C_{klmn} \alpha_{mn} \rangle$ term in Equation 3.26 is defined as

$$\langle C_{klmn} \alpha_{mn} \rangle = D_1 A_{ij} + D_2 \delta_{ij} \tag{3.27}$$

where D_1 and D_2 are given as

$$D_1 = a_1(b_1 + b_2 + 4b_3 + b_5) + a_2(b_1 + 3b_2 + 4b_3) \tag{3.28}$$

and

$$D_2 = a_1(b_2 + b_4) + a_2(b_2 + 3b_4 + 4b_5) \tag{3.29}$$

In Equations 3.28 and 3.29, a_1 and a_2 are defined as

$$a_1 = \alpha_{11} - \alpha_{22} \tag{3.30}$$

and

$$a_2 = \alpha_{22} \tag{3.31}$$

where α_{11} and α_{22} are the longitudinal and transverse components of the transversely isotropic CTE tensor, α_{ij}, for a unidirectional composite in the x_1 and x_2 directions

respectively. Stair and Jack [82] produced a tensor form for a transversely isotropic unidirectional composite, which is given as

$$\alpha = \begin{bmatrix} \alpha_{11} & 0 & 0 \\ 0 & \alpha_{22} & 0 \\ 0 & 0 & \alpha_{22} \end{bmatrix} \tag{3.32}$$

The evaluation of the CTE components are defined by the upper and lower bounds of the coefficient of thermal expansion for unidirectional composites with isotropic phases which was defined by Schapery [81].

3.6 Results

3.6.1 Deposition Flow Models

The free surface minimization approach described above was employed to determine the extrudate shapes for deposition flows appearing in Figures 3.4-3.6. In Figure 3.4 (A), the initial free surface shape for the level flow minimization is shown and the minimized flow shape is shown in Figure 3.4 (B). The initial shapes for the deposition flows are defined by setting design variables downstream from the nozzle exit equal to the bead height and design variables leading the nozzle equal to the expected maximum x value for the flow front. For the level flow the downstream design variables are set as y points equal to 3 mm and x is set as points ranging from -1.5875 mm to −8 mm with a distribution that allows more points near the nozzle exit. The leading curve is set with all x points equal to 3.5 mm and y points ranging from 3 mm to 0 mm with a distribution that puts more points near the nozzle exit and the translating plate (fewer in the middle of the flow shape). The initial shapes yield an objective function value (cf. Equation 3.5) of

458.4 mm^2/s^2 for the level flow, 943.9 mm^2/s^2 for the falling flow, and 907.1 mm^2/s^2 for the bull nose flow.

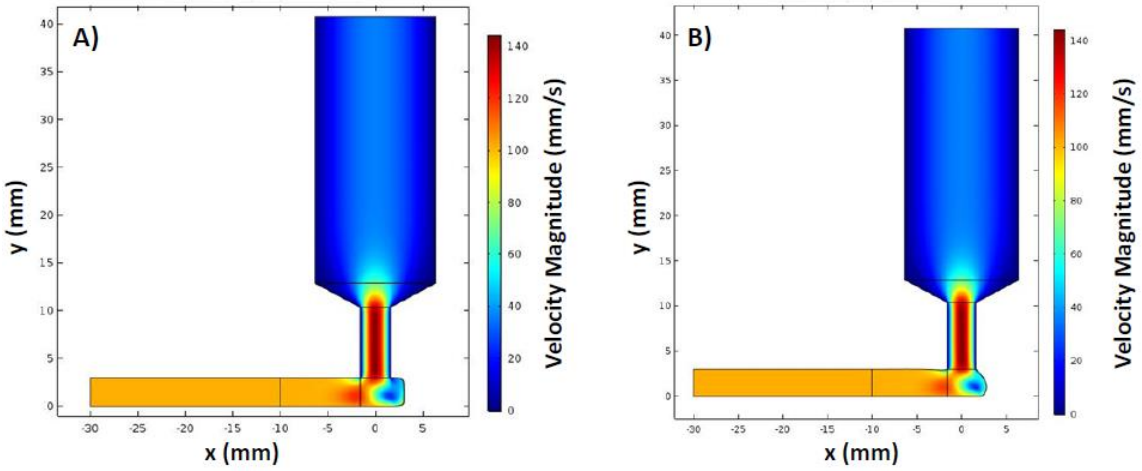

Figure 3.4. A) Flow Velocity for Level Flow Domain with the Initial Extrudate Shape and B) Minimized Extrudate Shape

The value of the objective function $f(\underline{\alpha})$ in Equation 3.5 appears in Figure 3.5 as a function of optimization iteration number.

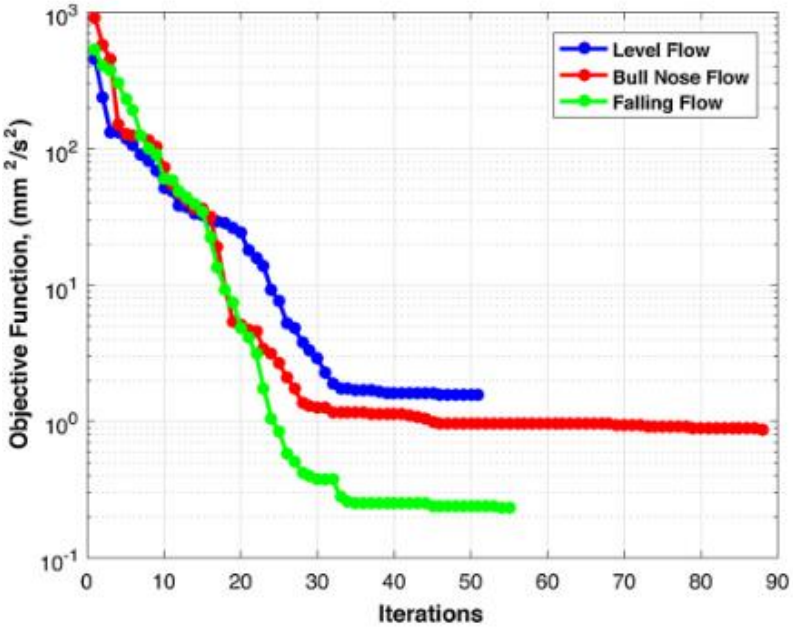

Figure 3.5. Deposition Flow Models Minimization Iteration History

Note that the objective function value decreases from 458.4 mm^2/s^2 to 1.6 mm^2/s^2 over 51 iterations for the level flow, which is a reduction of 99.7%. Similar reductions to near zero are seen for all three deposition models where the minimized flow shapes appear in Figure 3.6.

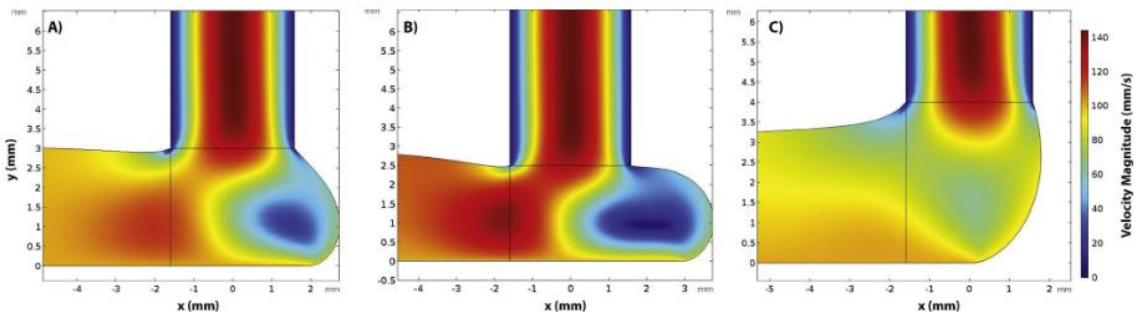

Figure 3.6. Computed Shape of Deposition and Velocity Magnitude (mm/s): A) Level Flow, B) Bull Nose Flow, C) Falling Flow

It is seen that the optimum shape of the deposition appearing in Figure 3.4 has a non-zero value for the objective function. This is due to the inherent singularities that occur at a no slip to free surface boundary condition point. To examine the quality of the minimization, a volumetric flow loss is computed to quantify the total amount of fluid crossing the free surface boundary. The computed free surface flow loss for the level flow is 0.19% of the total volumetric flow. Similarly, the falling flow has a volumetric loss of 0.33% and the bull nose flow has a loss of 1.15%. These values show that a negligible quantity of the flow is uncontained, and the minimization has the effect of producing the flow shape for the fluid domain including the extrudate swell. The higher percentage of volumetric flow loss in the bull nose flow is due to the sharp corner made at the nozzle exit in the front of the nozzle which produces a larger singularity. The

square of the normal velocity along the free surface for the level flow condition appears in Figure 3.7. It is seen that, except at the end points where large thin peaks exist, the values of velocity normal to the extrudate free surface are nearly zero. These peak values at the ends of the free surface add a relatively small non-zero value to the objective function during the minimization. Also apparent in Figure 3.6 is that a larger contribution from the singularity is seen in the upper free surface as compared to the lower.

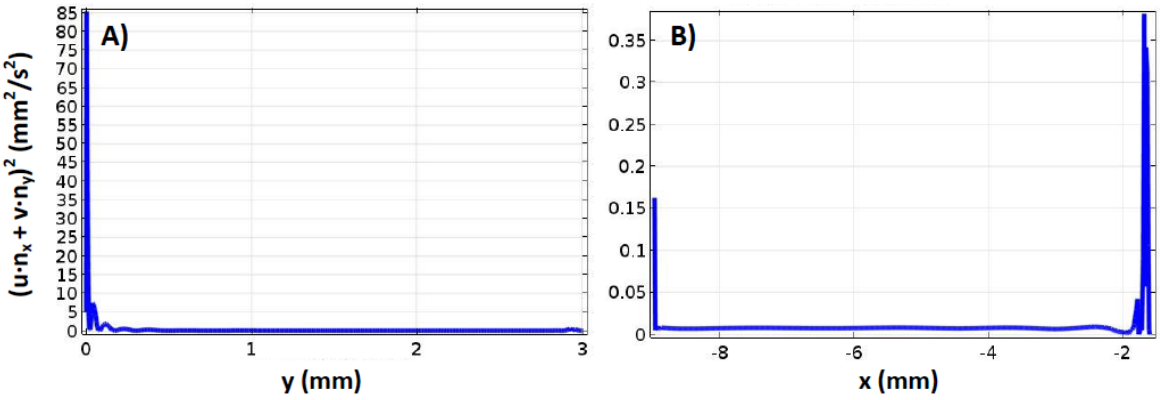

Figure 3.7. Square of the Normal Velocity Component Along the A) Upper and B) Lower Boundaries

3.6.2 Straight Flow Model

The straight planar flow model is evaluated in the same manner as the deposition models shown in the previous section. The initial and minimized flow shapes for the straight planar flow are shown in Figure 3.8 (A) and (B). The objective function value for the initial shape is 54.4 mm^2/s^2 for the straight flow and the minimized flow shape has a volumetric flow loss of 0.28%. Also, the optimized free surface shape for the straight flow had an extrudate swell of 19.2% which is comparable to that given for sheet type dies in the literature [49-51].

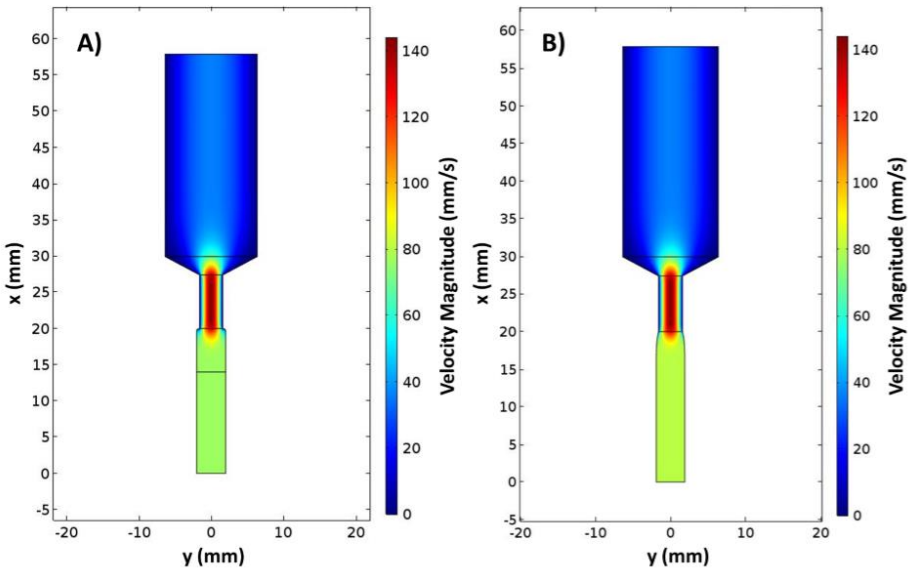

Figure 3.8. A) Flow Velocity for Straight Flow Domain with the Initial Extrudate Shape and B) Minimized Extrudate Shape

The objective function value with respect to iteration number is shown in Figure 3.9 for the straight flow model. The initial objective function value and the minimized value are substantially lower than what is seen in the deposition flow models. This is due to the free extrusion boundary condition that is defined for the extrudate which is simple in comparison to deposition onto a plate.

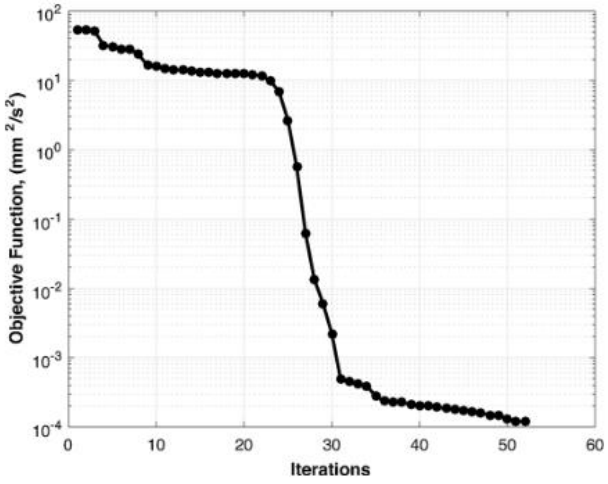

Figure 3.9. Straight Flow Model Minimization Iteration History

3.6.3 Fiber Orientation

Once the four flow regimes have been optimized, streamlines are calculated throughout the fluid domain. Ten streamlines equally spaced at the flow inlet progress through the flow domain, providing a path for computing fiber orientation tensors. The streamline locations and numbers are shown in Figure 3.10 for the optimal extrudate shape for the level flow. The initial placement for the start of the streamlines is the same as that shown in Figure 3.10 for each of the flow types studied.

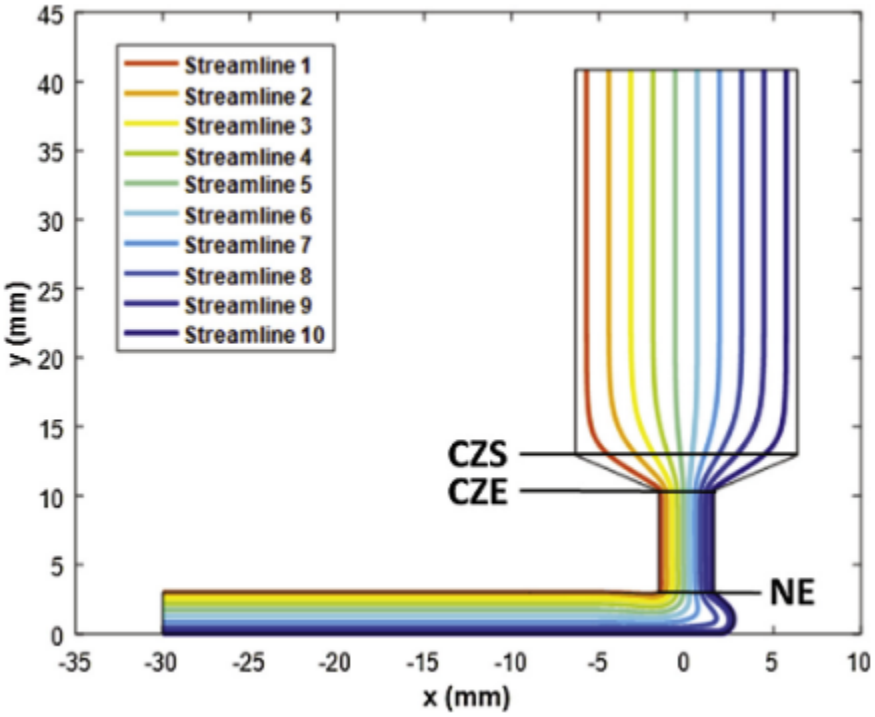

Figure 3.10. Ten Evenly Spaced Streamlines for Three Flow Regimes

Velocity and velocity gradients are evaluated along the ten streamlines to construct the vorticity and rate of deformation tensors evaluated in Equations 3.10 and 3.11, respectively, which appear in the orientation tensor evolution Equation 3.19. In the following fiber orientation evaluation, Equation 3.18 is used to compute the interaction

coefficient, $C_I = 0.0067$, and we use a cylindrical fiber aspect ratio, $\xi = 15$ which yields an equivalent aspect ratio, $\beta = 10.9314$, from Equation 3.13 and a value of, $\lambda = 0.9834$, from Equation 3.12. Figure 3.11 (A) and (B) provide a measure of fiber alignment in the y and x directions, respectively, represented here as the orientation tensor components A_{22} and A_{11}. In Figures 3.11 (A) and (B) and 3.12 (A) plots are shown as a function of d, which is the distance along the streamlines in Figure 3.10,which provides a convenient metric for identifying position in the flow. Also, regions in the flow domain are designated as convergence zone start (CZS), convergence zone end (CZE), and nozzle exit (NE) as shown in Figure 3.10.

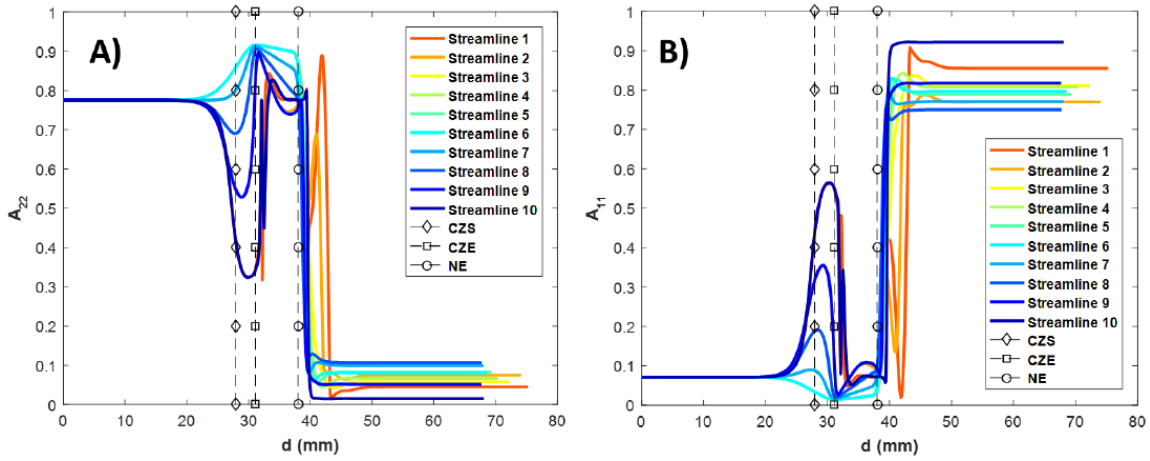

Figure 3.11. A) Fiber Alignment in the y Direction for Level Flow, A_{22}, B) in the x Direction for Level Flow, A_{11}

The initial orientation imposed at the inlet of the domain is that of the steady state for a pure shearing flow. During the initial flow history, the orientation state is unchanged as the fluid experiences pure shearing until it reaches the convergence zone start. When the flow enters the convergence zone a rapid increase in alignment in the y-direction is observed due to extensional flow. The orientation component A_{22} is shown to approach a

value of 0.9 (i.e., near uniaxial alignment) at the convergence zone end. A small decrease in fiber alignment in the y direction is seen in the straight portion of the nozzle before the nozzle exit as the flow transitions back to a shear dominated flow. The pure shear flow causes fibers to align more towards the steady state value seen at the inlet. The decrease in fiber alignment at the nozzle exit is due to expansion flow below the nozzle exit. Upstream of the nozzle exit, all four flows behave in the same manner. However, due to different flow shapes at the nozzle exits the amount of decrease in fiber alignment differs for each of the three flow regimes. For the level flow, streamlines closest to the upper extrudate curve, show an increase in velocity as the fluid accelerates to accommodate the plate speed, causing an increase in the fiber alignment. Also, fluid along streamlines closest to the leading extrudate curve decreases in speed as it enters the near-recirculation region appearing in Figure 3.4. The flow through the near-recirculation region has velocity gradients that vary significantly. The velocity gradients in this region quickly decrease fiber alignment in the y direction. Similar behavior is seen for all three deposition flows. The straight flow shows similar fiber alignment characteristics to the deposition flows with high fiber alignment in the extruded bead. It is seen in Figure 3.11 (A) that the fiber alignment in the y direction decreases substantially during deposition and into the extruded bead. This decrease coincides with an increase in the fiber alignment in the x direction which results in a high fiber alignment in the direction of the extruded bead as seen in Figure 3.11 (B). Figure 3.12 (A) shows the angle of alignment, θ, as a function of length d along each streamline as computed with Equation 3.23.

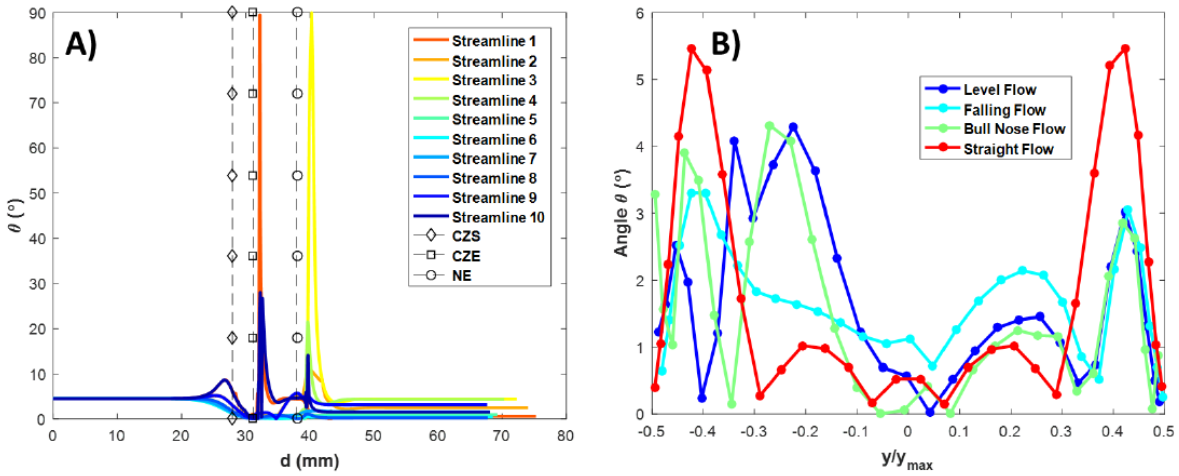

Figure 3.12. A) Angle Between Eigenvector of Maximum Eigenvalue of A and Tangential Velocity Vector For Level Flow, B) Angles Through Bead Thickness in Steady State for all Flow Regimes

At the inlet of the nozzle the principal eigenvector of the second order orientation tensor is within 5° of the y coordinate direction, which implies a fiber alignment state that is very near the y vector. At the convergence zone start, the principal eigenvector begins to decrease and reduces to near zero at the convergence zone end, which indicates a fiber alignment state that is almost perfectly aligned with the velocity vector along the streamline. In the straight portion of the nozzle before the nozzle exit the angle increases slightly due to pure shear flow as shown in Figure 3.11. Immediately after the nozzle exit the orientation angle changes rapidly in the expansion flow before reaching steady state. Computed angle of alignment values along all streamlines show that the principal eigenvector of the orientation tensor is within 5° of the unit x vector, indicating that optimum directional mechanical improvement in the polymer composite is 5 ° off of the x direction vector for the deposition flow models. Figure 3.12 (B) shows the angle of alignment, θ, through the bead thickness for all flow types. Figure 3.12 (B) plots degree of alignment over a range of y/y_{max} of -0.5 to 0.5 where -0.5 designates the bottom (left

bound for the straight flow model) and 0.5 designates the top (right) bound of the extruded bead. The normalized thickness y/y_{max} is used due to the straight flow extrudate having a thickness greater than the deposited beads due to extrudate swell of a flow that is not constrained by deposition onto a plate. The angle of alignment varies over the cross section of each flow type and varies between flow types as shown in Figure 3.12 (B). All flow shapes show a maximum degree of alignment near 5° with an average angle of near 2°.

3.6.4 Mechanical and Thermomechanical Property Evaluation

Using computed fiber orientation results presented above, mechanical properties in the extruded bead can be computed for a given matrix and fiber materials, and fiber volume fraction. The ABS matrix material considered here has a modulus of elasticity of 2.25 GPa and a Poisson's ratio of 0.35 [120]. The chopped carbon fiber material has an elastic modulus of 230 GPa and a Poisson's ratio of 0.2 which is representative of T300 PAN based fibers [121]. The volume fraction, V_f, is 13% which is common for LAAM printing materials. Figure 3.13 shows the six independent components of the second order orientation tensor through the bead thickness following deposition for the level flow type.

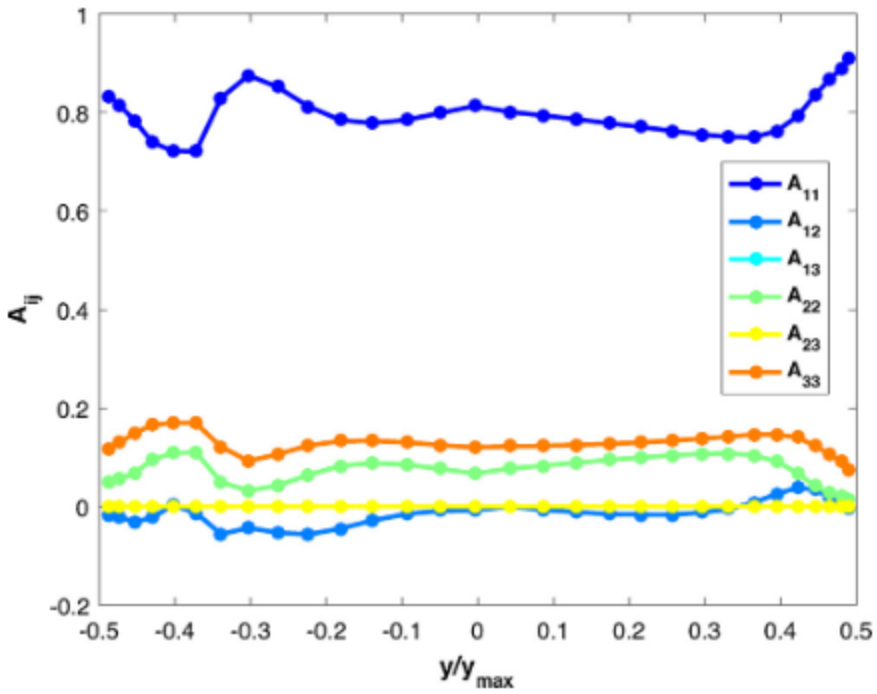

Figure 3.13. Orientation Tensor Components in the Printed Bead for Level Flow

The fiber orientation tensor components are taken from the steady state flow after the nozzle exit. The six independent tensor components are defined through the thickness of the bead using a normalized y component described in Figure 3.12 (B). All four flow types evaluated here have, A_{11}, values in the extruded bead near 0.8, indicating a slightly less aligned state than the values near 0.9 measured by Tekinalp, et al. [3] for filament-based FFF beads. Tekinalp's results indicate the propensity for polymer composite deposition AM to provide high fiber alignment as we have computed. However, differences in the process, material system, and processing conditions result in slightly different orientation tensor results as compared to our calculations. Upon comparing BAAM micrographs in Duty, et al. [10] to the FFF micrographs in Tekinalp, et al. [3], it is apparent that the large scale deposition process may lead to a less aligned state than the FFF process, further supporting our results. The orientation tensor components of the

second order tensor shown in Figure 3.13 along with the unidirectional composite stiffness tensor which is evaluated using the fiber and matrix properties defined above are used to calculate the mechanical and thermomechanical properties through the bead thickness for all four flow types using Equations 3.24 and 3.25. The components of the misaligned composite stiffness tensor are then used to evaluate the principal moduli values which are shown in Figure 3.14.

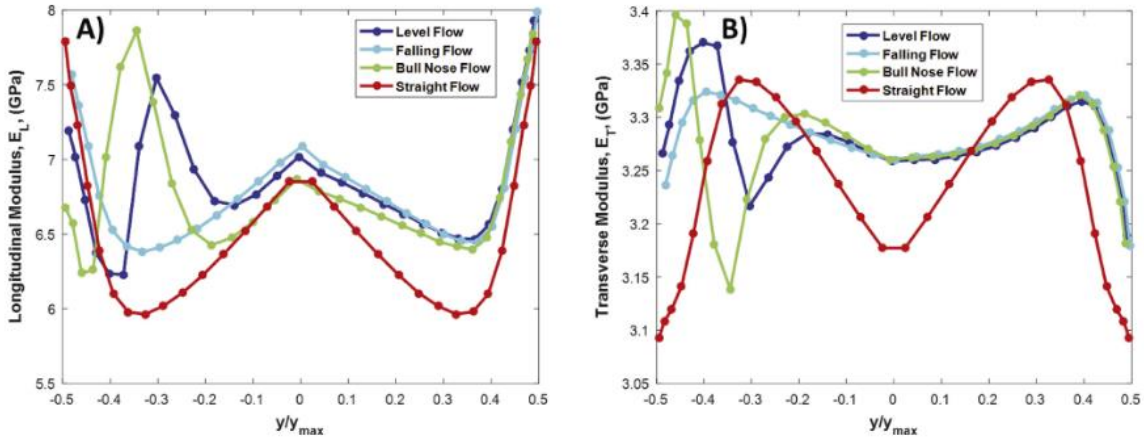

Figure 3.14. A) Longitudinal, and B) Transverse Moduli in the Printed Bead for all Flow Regimes

The coefficient of thermal expansion in the longitudinal α_L, and transverse, α_T, directions is computed from Equation 3.26 and shown in Figure 3.15 for the four flow types. We use a CTE value for ABS of 80 1e−6/°C [120] which is the midrange of the given properties and for carbon fiber of -0.6 1e−6/°C [121]. The longitudinal coefficient of thermal expansion for the printed composite is shown to be substantially lower than the transverse coefficient of thermal expansion for all flow types. This is expected for a highly aligned fiber orientation state since the CTE value of carbon fiber is substantially

lower than that of the ABS polymer matrix. Bead cross section average values are computed from data in Figures 3.14 and 3.15 and appear in Table 3.1.

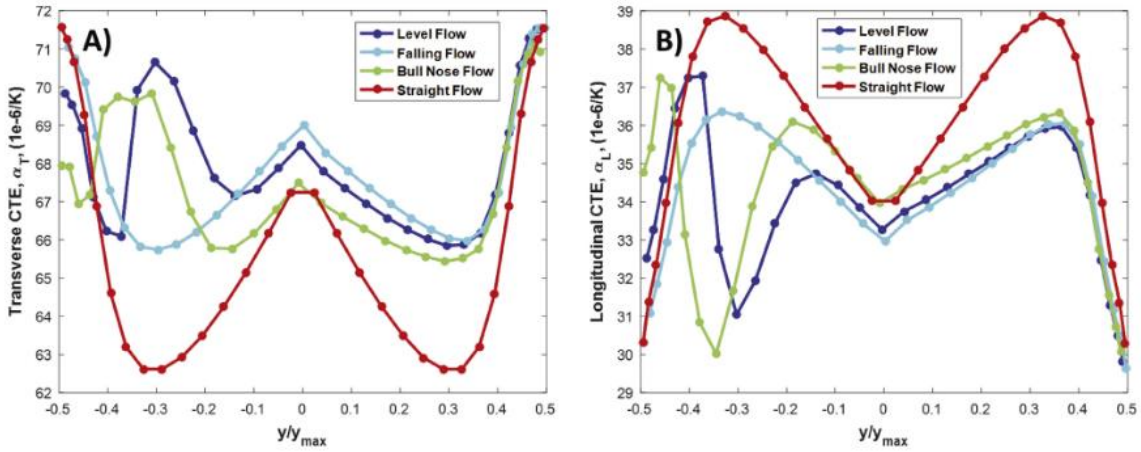

Figure 3.15. A) Longitudinal, and B) Transverse CTE in the Printed Bead for all Flow Regimes

Values of longitudinal modulus are approximately twice that of the transverse modulus which is expected in a highly aligned fiber filled polymer. Table 3.1 shows that the moduli for the four flow types are very close in magnitude, all of which fall within 5% of each other. The longitudinal and transverse coefficient of thermal expansion are also similar among all flow types. All values are within 5% for both the longitudinal and transverse coefficient of thermal expansion and the longitudinal coefficient of thermal expansion is nearly twice the transverse direction. The mechanical properties shown in the table above agree well with the properties measured by Duty, et al. [10] and predicted by Wang, et al. [9]. Duty reported an elastic modulus of 7.24 GPa with a standard deviation of 0.59 GPa and Wang predicted elastic moduli values ranging from 6.57 to 7.49 GPa for the different flow models, which are dependent on viscosity models used. Our predicted values for the deposition flow models are all within the standard deviation

presented by Duty, et al. [10] and within the range presented by Wang, et al. [9] While the average values for the principal moduli and coefficient of thermal expansion are all very close the properties through the thick-ness of the bead vary substantially as seen in Figures 3.14 and 3.15. This variation in the coefficient of thermal expansion through the bead thickness could contribute to differential contraction during part cooling, thus contributing to warping and delaminations in printed parts due to internal thermal stresses which increase the occurrence of these print failures.

Table 3.1. Calcualted Cross Section Average Mechanical Properties in Extruded Bead of Four Flow Regimes

	E_L (GPa)	E_L (GPa)	G_{12} (GPa)	ν_{12}	α_L (1E-6/K)	α_T (1E-6/K)
Level Flow	6.88	3.17	1.26	0.362	34.00	68.18
Falling Flow	6.85	3.17	1.26	0.362	34.13	67.99
Bull Nose Flow	6.82	3.18	1.27	0.364	34.32	67.59
Straight Flow	6.57	3.23	1.31	0.366	35.62	66.12

3.6.5 Conclusions from Planar Deposition Flow Model and Property Evaluation

This paper presents a computational method for evaluating the deposition of short fiber polymer composites for LAAM printing systems. An optimization method is presented which computes the shape of polymer deposition onto a print platform by minimizing the normal velocity of the deposited extrudate along the free surfaces. Fiber orientation within the polymer composite is then evaluated using the geometries obtained in the melt flow surface shape optimization. The fiber orientation evaluation shows that fiber alignment in the flow direction is high at the inlet, increases in the convergence zone, and then decreases slightly in the straight portion of the nozzle. It is seen that the fiber alignment in the extrudate directly below the nozzle exit exhibits different behavior for each of the flow types. For the three deposition models, the large decrease in the fiber

alignment in the y direction occurs as the fiber alignment in the x direction increases which occurs in the region where deposition flow turns below the nozzle exit. The highly aligned fiber orientation state in the beads longitudinal direction results in high longitudinal modulus with a value that is approximately twice that of the transverse moduli. It is understood from these results that the expected fiber orientation state in large area polymer deposition is highly aligned along the bead axis, resulting in a high longitudinal modulus of the deposited bead. The average of the principal moduli and coefficient of thermal expansion for all four models are within 5% of each other, however, the bull nose flow does have a substantially different alignment profile which may affect how the polymer composite behaves during cooling. It is also worth noting that even for a Newtonian flow model all fiber orientation and mechanical property evaluations are within that presented by the experimental measurements done by Duty, et al. [10] and the more complex non-Newtonian and viscoelastic models presented by Wang, et al. [9]. It is also worth noting that the three deposition flows have very similar results as compared to the straight flow indicating that the turning flow and nozzle height during deposition does not have a substantial effect on the final mechanical and thermomechanical properties of a printed fiber filled composite bead. This study shows that the nozzle geometry, nozzle height, and deposition onto a print plate during printing effects the fiber alignment state through the thickness of the bead. The average moduli are seen to have little variation with respect to nozzle print height. Further development of the flow models include the addition of viscoelastic fluids, non-isothermal effects, and fiber orientation coupling to better represent the printing process.

CHAPTER FOUR

Non-Newtonian Non-Isothermal Planar Deposition Flow Modeling of Fiber Filled Composites in Large Area Additive Manufacturing

In the previous chapter a planar deposition flow model for fiber filled composites in Large Area Additive Manufacturing was presented which analyzed Stokes flow of an isothermal Newtonian fluid being extruded from a nozzle onto a print platform [7]. It is understood that polymers do not behave as Newtonian fluids but are shear thinning fluids that can be modeled using a Generalized Newtonian Fluid (GNF) model or a viscoelastic fluid model. Wang, et al. [9] analyzed a similar axisymmetric model to that of Heller, et al. [6] for a LAAM extrusion nozzle, but took into consideration the swell of Power Law, Carreau-Yasuda, Simplified Viscoelastic, and Phan-Thien-Tanner models for polymer melts. Recently, Bertevas, et al. [122] modeled a planar deposition flow of an isothermal Carreau-Yasuda GNF for an FFF nozzle. All results were compared to the works done by the Baylor flow modeling group [6-9] with respect to flow shape and fiber orientation results. The flow models presented by Bertevas, et al. [122] are isothermal and use the Folgar-Tucker IRD function for fiber orientation, which are improved upon in the following chapter by the inclusion of a non-isothermal Carreau Yasuda GNF model and the use of the IRD-RSC model produced by Wang, et al. [17] which is considered the most accurate fiber interaction model to date.

In this chapter a non-isothermal, non-Newtonian deposition flow model will be presented. Fiber orientation will also be evaluated in a similar fashion to the work presented in Chapter Three, but the IRD-RSC model will be used and thermal

conductivity for misaligned fiber filled composites will be introduced for the first time. The thermal conductivity of fiber filled polymers is of great importance to the given model due to the non-isothermal problem being evaluated and the heat transfer model presented in the following chapter.

4.1 Non-Isothermal Non-Newtonian Planar Deposition Flow Model for Large Area Additive Manufacturing

In this study, the motion of the polymer melt flow is modeled as a two-dimensional planar Stokes flow of an incompressible Carreau-Yasuda generalized Newtonian fluid with temperature dependent viscosity which is modeled as an Arrhenius relation. The polymer melt flow is defined as a low Reynolds number flow with high viscosity. Conservation of mass and momentum equations for the Stokes flow of an incompressible Carreau-Yasuda fluid are given as

$$\nabla \cdot \mathbf{v} = 0 \tag{4.1}$$

and

$$\nabla \cdot \boldsymbol{\sigma} = 0 \tag{4.2}$$

where $\mathbf{v}$ is the velocity vector and $\boldsymbol{\sigma}$ is the stress tensor written as

$$\boldsymbol{\sigma} = -p\boldsymbol{I} + \mu[(\nabla \mathbf{v}) + (\nabla \mathbf{v})^{\mathrm{T}}] \tag{4.3}$$

In Equation 4.3, p is the pressure, $\boldsymbol{I}$ is the identity tensor, μ is the fluid viscosity which is defined for a Carreau-Yasuda GNF fluid as

$$\mu_C(\dot{\gamma}) = \mu_\infty + (\mu_0 - \mu_\infty)[1 + (\lambda\dot{\gamma})^2]^{\frac{n-1}{2}} \tag{4.4}$$

where μ_∞ is the viscosity at an infinite shear rate, μ_0 is viscosity at a zero shear rate, λ is the relaxation time of the polymer, $\dot{\gamma}$ is the shear rate, and n is the power index. In

Equation 4.4 the zero shear viscosity, μ_0, is temperature dependent which is modeled using an Arrhenius function given as

$$\mu_0(T) = \mu_{0C} e^{\left(\frac{E_a}{R}\left(\frac{1}{T}-\frac{1}{T_0}\right)\right)} \tag{4.5}$$

where μ_{0C} is the zero shear rate viscosity for an isothermal Carreau-Yasuda model, E_a is the activation energy of the polymer (for ABS 138-151 kJ/mol [123]), R is the universal gas constant, T is the temperature of the polymer, and T_0 is the reference temperature at which μ_{0C} is evaluated. It is assumed that the fluid is incompressible, no gravity, body forces, or surface tension is evaluated, and it is a Stokes flow with negligible fluid inertia.

The non-isothermal problem also necessitates the conservation of energy for the fluid flow domain which is given as

$$\rho C_p \mathbf{v} \cdot \nabla T - \nabla \cdot k \nabla T = \boldsymbol{\tau} : \nabla \mathbf{v} \tag{4.6}$$

where ρ is the fluid density, C_p is the heat capacity at constant pressure, k is the thermal conductivity, T is the temperature, and $\boldsymbol{\tau}$ is the viscous stress tensor defined for an incompressible fluid as

$$\boldsymbol{\tau} = 2\mu \boldsymbol{\Gamma} \tag{4.7}$$

In Equation 4.7 μ is the viscosity defined by Equations 4.4 and 4.5 and $\boldsymbol{\Gamma}$ is the rate of deformation tensor given in Chapter Three, Equation 3.11. Two assumptions are added with respect to the non-isothermal model that is presented such as heat transfer is quasi-steady state, and viscous dissipation is included. Viscous dissipation is thermal energy generation due to work done by a fluid undergoing shear forces in a polymer flow. Viscous dissipation is shown to increase the temperature of the polymer by approximately 2 °C in the current model.

The same free surface approach is used as in Chapter Three with two necessary boundary conditions, zero normal velocity and zero surface traction, along the free surface given as

$$\mathbf{n} \cdot \mathbf{v} = 0 \tag{4.8}$$

and

$$\boldsymbol{\sigma} : [\mathbf{nn}] = 0 \tag{4.9}$$

where ":" indicates the double contraction of the stress tensor with the outer product of the normal vector with itself, giving the stress traction along the free surface. The zero stress traction boundary condition is shown in Figure 4.1 (A).

There are two major differences due to the use of the temperature dependent Carreau-Yasuda GNF viscosity model. The stress tensor defined in Equation 4.3 will now be subject to a viscosity that is temperature and shear rate dependent, and the velocity along the free surface boundary will have more complex velocity profiles due to temperature and shear rate dependence. For this reason, the minimization will be more complex. Previous Newtonian fluid models ran in approximately 30 s whereas the non-isothermal Carreau-Yasuda models with the inclusion of the deposition plate run in approximately 150s, making the minimization process more time intensive.

The flow domain is again modeled for the Strangpresse Model 19 [19] extruder where the geometry is given in Figure 3.1. The extruder was found to deposit material at half the rate originally used in the analysis given in Chapter Three; therefore, in this chapter the plate speed will be set at $v_x = 50.8\, mm/s$ and $v_y = 0\, mm/s$ which is shown in Figure 4.1 (A). It is worth noting, the results for Chapter Three would be unchanged due to being a Newtonian fluid flow. The magnitude of the normal velocity along the free

surface boundaries scale linearly with fluid velocity and would thus result in lower magnitudes but not would not change the extrudate shape. Also, shear rate does not change the viscosity of a Newtonian fluid and thus the velocity gradients would remain unchanged.

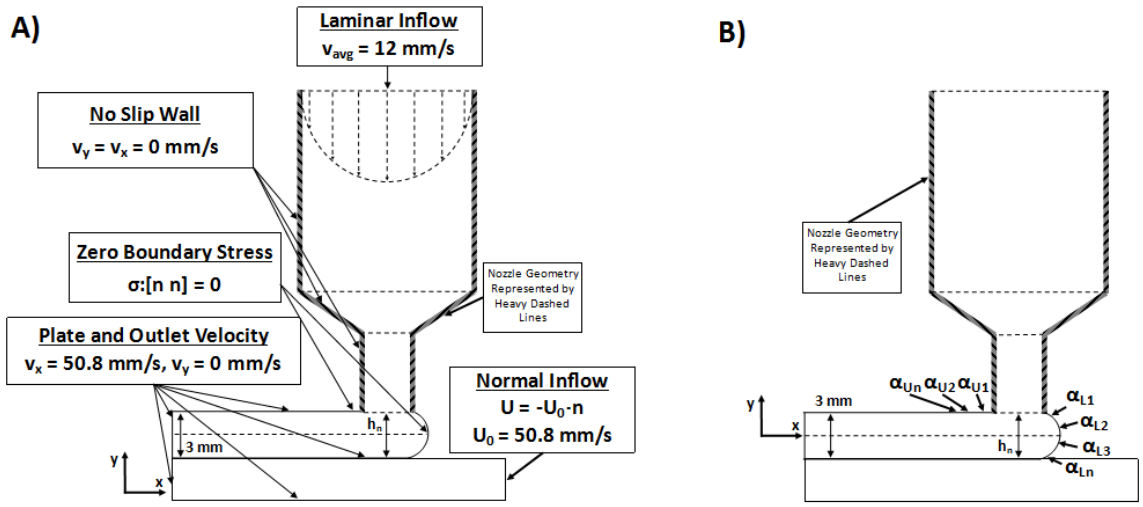

Figure 4.1. A) Boundary Conditions, B) Design Variables for Deposition Flow Models

In this work nozzle height, h_n, is always equal to 3 mm which is also the bead height, h_b, for the given models. Similar to models presented in the previous chapter, the outlet and plate velocities are set to be $v_x = 50.8\ mm/s$ and $v_y = 0\ mm/s$, which along with the volumetric flow rate defined at the inlet defines the deposited bead height for the deposition flow models. For the deposition flow simulations shown in Figure 4.1 (A), the lower surface of the extruded bead is moving at the plate velocity $v_x = 50.8\ mm/s$ with $v_y = 0\ mm/s$. The inlet of the nozzle is defined as a fully developed laminar flow profile with an average velocity, $v_{avg} = 12\ mm/s$ in all simulations. The polymer melt flow is assumed to have a no-slip boundary within the nozzle which is defined as $v_x = v_y = 0\ mm/s$. The properties used for the Stokes flow of a Carreau-Yasuda GNF fluid for the

finite element evaluations are given as, $\mu_{0C} = 3100\ Pa \cdot s$, $\mu_{\infty} = 0\ Pa \cdot s$, $\lambda = 0.11\ s$, $n = 0.445$, and $\mu_{plate} = 1E8\ Pa \cdot s$. The flow portion of the model must also be defined for the plate, which is done by applying a constant plate velocity which has been defined, and by setting the viscosity of the plate as a near infinite viscosity fluid, $\mu = 1E8\ Pa \cdot s$. This method has been used for fluid flow models in literature as it simplifies the finite element problem by neglecting the solid dynamics which would be needed for a solid plate model.

The plate geometry is included in the finite element models presented here unlike the models used in Chapter Three, which is necessary for the non-isothermal problem shown in Figure 4.2. The only parameters that are varied in this work is the addition of the non-isothermal problem and the plate material. There are three models evaluated here: isothermal deposition onto an aluminum plate, non-isothermal deposition onto an aluminum plate, and non-isothermal deposition on an ABS plate (represents deposition onto a previously deposited layer). The extrudate shape and updated fiber orientation and mechanical and thermomechanical properties is included for the Newtonian flow model from Chapter Three as a reference. For the non-isothermal models the plate is set at an initial temperature of 80 °C, which is used for the LAAM printer being modeled, and "flows" from right to left at the given plate speed. By setting an initial temperature the plate is allowed to heat upon deposition of the ABS beads through conduction and can cool through convection and radiation during the print process. The bottom of the plate is set at a fixed temperature of 80 °C which is set in reference to the heat held by the temperature controller in the Baylor Large Area Additive Manufacturing printer. The temperature of the ABS fluid is set at a temperature of 230 °C at the inlet of the nozzle

and the nozzle boundary conditions are set as thermal insulation which maintains this temperature through the interior of the nozzle. This is a simplification of the heat transfer conditions that occur in the nozzle, but due to the very short amount of pre-contraction nozzle that is modeled is considered acceptable. Immediately after deposition, the ABS bead is allowed to cool through conduction with the print plate, convection with ambient air, and radiation into ambient air. It is understood that for most situations conduction with the print plate will be the dominant heat transfer mechanism, but for completeness of the model convection and radiation are considered.

For all three models the values that are changed are the mechanical and thermomechanical properties of the deposition platform related to the non-isothermal problem, heat capacity at constant pressure, C_p, thermal conductivity, k, and density, ρ. The properties used for the non-isothermal portion of the flow model is given as, $C_{p,ABS} = 1680\, J/(kg \cdot K)$, $k_{ABS} = 0.2728\, W/(m \cdot K)$, $\rho_{ABS} = 1050\, kg/m^3$, $C_{p,AL} = 900\, J/(kg \cdot K)$, $k_{AL} = 208\, W/(m \cdot K)$, and $\rho_{AL} = 2700\, kg/m^3$.

As was previously stated, the minimization approach used in Chapter Three is exactly the same as what is used for the current work. Analysis of the minimization approach is; therefore, referred to that defined in Chapter Three.

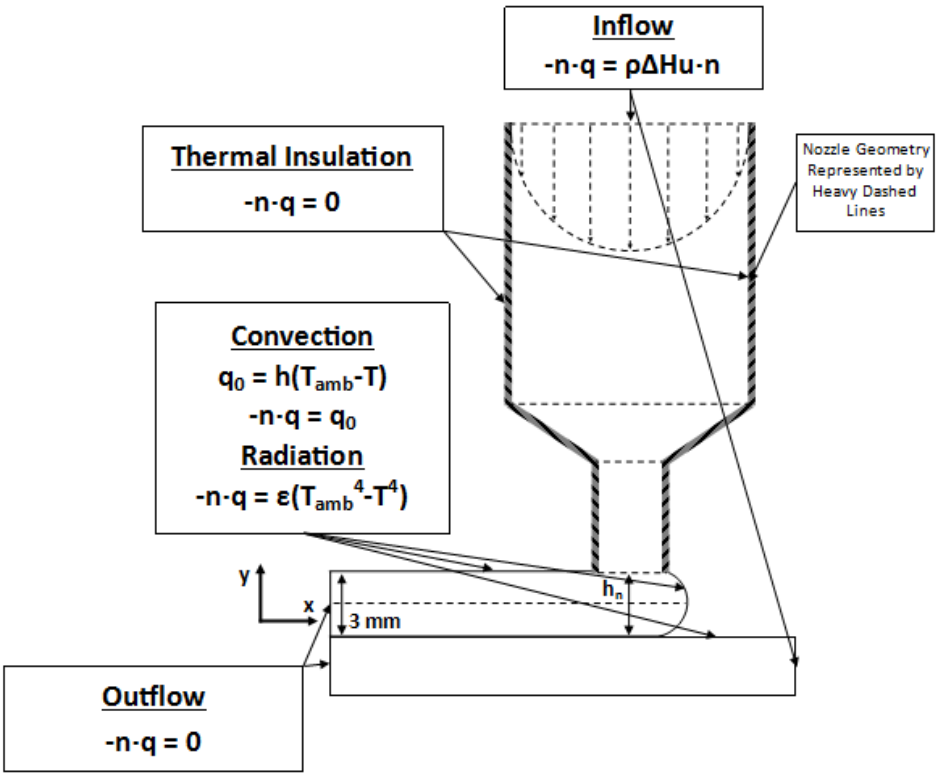

Figure 4.2. Non-isothermal Boundary Conditions

4.2 Fiber Orientation in the Non-Isothermal Non-Newtonian Planar Flow Deposition Model

Warping, delamination, and bond strength have become the main focus in polymer deposition additive manufacturing in recent years as it poses a substantial barrier to industrial viability of this technology. The addition of short carbon fibers to the polymer feedstock has substantially improved LAAM printing by decreasing the coefficient of thermal expansion and improving the bulk strength of printed materials. The improvement of these properties has been evaluated and is presented in Chapter Three of this dissertation, but the effect of short carbon fiber on thermal conductivity of the printed polymer has not yet been evaluated via finite element modeling. Fiber orientation and the resultant mechanical and thermomechanical properties of LAAM

printed beads will be analyzed again as in Chapter Three for the non-isothermal Carreau-Yasuda GNF planar flow deposition model as some change is expected from previously published results. The main additions to the fiber orientation evaluation will be the use of the IRD-RSC fiber interaction model and the evaluation of thermal conductivity for misaligned fibers via the orientation homogenization method.

The IRD-RSC model proposed by Wang, et al. [17] is used in this work due to its improved fiber interaction that is considered to be more accurate than the previously used Folgar Tucker [16] IRD model. The IRD-RSC model is given as

$$D_{IRD-RSC} = -2(1-\kappa)(\mathbb{L} - \mathbb{M}:\mathbb{A}):\boldsymbol{\Gamma} + 2\kappa C_I\dot{\gamma} \tag{4.11}$$

where $\mathbb{L}$ and $\mathbb{M}$ are analytical functions of the eigenvalues and eigenvectors of $\boldsymbol{A}$ which are defined respectively as

$$\mathbb{L} = \sum_{i=1}^{3} \lambda_i (e_i e_i e_i e_i) \tag{4.12}$$

and

$$\mathbb{M} = \sum_{i=1}^{3} e_i e_i e_i e_i \tag{4.13}$$

In Equation 4.11, κ is an empirical scaling parameter that ranges from 0 to 1. When κ reaches 1 the model reduces to the Folgar and Tucker IRD model.

4.2.1 Thermal Conductivity Property Evaluation for Misaligned Short Carbon Fibers

The orientation homogenization model for thermal conductivity of misaligned short fiber filled polymers is now presented. The derivation follows a similar approach as that presented in Jack and Smith [13]. First consider the Laplace series for the orientation distribution function given as

$$\psi(\theta,\phi) = \sum_{l=0}^{\infty} \alpha_l(\theta,\phi) \tag{4.14}$$

where α_l is an invariant subspace of the orientation distribution function, which is dependent on the angles of the principal fiber vector **p** given as θ and ϕ in Equation 2.8. The invariant subspace α_l is defined as

$$\alpha_l(\theta,\phi) = \sum_{l=0}^{\infty} C_l^m Y_l^m(\theta,\phi) \tag{4.15}$$

where Y_l^m are the l^{th} order complex spherical harmonic functions. It is worth noting that all odd invariant subspaces are zero due to the fiber orientation distribution function being symmetric. The invariant subspaces $\alpha_0(\theta,\phi)$ and $\alpha_2(\theta,\phi)$ can be cast as

$$\alpha_0(\theta,\phi) = \frac{1}{4\pi} \tag{4.16}$$

and

$$\alpha_2(\theta,\phi) = \frac{15}{8\pi}\left(p_i(\theta,\phi)p_j(\theta,\phi) - \frac{1}{3}\delta_{ij}\right)\left(a_{ij} - \frac{1}{3}\delta_{ij}\right) \tag{4.17}$$

The fourth, sixth, and all even ordered invariant spaces exist but can be truncated at the second ordered invariant subspace as shown by Jack and Smith [13] due to orthogonality of all increasing even ordered invariant subspaces. The second order fiber orientation distribution function can be stated as

$$\psi_2(\theta,\phi) = \alpha_0 + \alpha_2(\theta,\phi) \tag{4.18}$$

The thermal conductivity tensor for misaligned short fiber reinforced composites can be written in terms of rotation matrices. Using the rotation tensor

$$\boldsymbol{Q}(\theta,\phi) = \begin{bmatrix} \sin\theta\cos\phi & \sin\theta\sin\phi & \cos\theta \\ -\sin\phi & \cos\phi & 0 \\ \cos\theta\cos\phi & -\cos\theta\sin\phi & \sin\theta \end{bmatrix} \tag{4.19}$$

We also introduce the thermal conductivity tensor for unidirectional fiber filled composites which is given as

$$\boldsymbol{k}^{uni} = \begin{bmatrix} k_{11} & 0 & 0 \\ 0 & k_{22} & 0 \\ 0 & 0 & k_{33} \end{bmatrix} \tag{4.20}$$

Note that $k_{22} = k_{33}$ for unidirectional composites and is substituted in Equation 4.20. The orientation averaged thermal conductivity tensor for misaligned fibers can be written using rotation matrices presented in Equation 4.19, the thermal conductivity tensor for unidirectional short fiber composites given in Equation 4.20, and the orientation distribution function given in Equation 4.18, which is given as

$$\langle k_{ij} \rangle = \oint_{\boldsymbol{S}^2} Q_{mi}(\theta,\phi) Q_{nj}(\theta,\phi) k_{mn}^{uni} \psi_2(\theta,\phi) d\boldsymbol{S} \tag{4.21}$$

where $\boldsymbol{S}^2$ is the surface of the unit sphere. In terms of orientation tensor components and thermal conductivity components the thermal conductivity tensor can be written as

$$\langle k_{ij} \rangle = \begin{bmatrix} \beta_1 & A_{12}(k_{11}-k_{22}) & A_{13}(k_{11}-k_{22}) \\ A_{12}(k_{11}-k_{22}) & \beta_2 & A_{23}(k_{11}-k_{22}) \\ A_{13}(k_{11}-k_{22}) & A_{23}(k_{11}-k_{22}) & \beta_3 \end{bmatrix} \tag{4.22}$$

where β_1, β_2, and β_3 are defined as

$$\begin{aligned} \beta_1 &= \frac{1}{3}\left((1 + 2A_{11} - A_{22} - A_{33})k_{11} + (2 - 2A_{11} + A_{22} + A_{33})k_{22}\right) \\ \beta_2 &= \frac{1}{3}(-(-1 + A_{11} - 2A_{22} + A_{33})k_{11} + (2 + A_{11} - 2A_{22} + A_{33})k_{22}) \\ \beta_3 &= \frac{1}{3}(-(-1 + A_{11} + A_{22} - 2A_{33})k_{11} + (2 + A_{11} + A_{22} - 2A_{33})k_{22}) \end{aligned} \tag{4.23}$$

The thermal conductivity for misaligned short fiber filled polymers is expressed using the unidirectional thermal conductivity tensor for short fibers and the diagonal terms of the second order orientation tensor.

The micromechanics model used to evaluate the thermal conductivity of unidirectional short carbon fibers is the model presented by Halpin [79] where the thermal conductivities in the x_1 and x_2 direction, i.e., $k_{11}$and k_{22}, respectively, are defined as

$$k_{11}^{sfrp} = \frac{1 + 2\left(\frac{l}{d}\right)\mu_1 v_f}{1 - \mu_1 v_f} k_m \tag{4.25}$$

and

$$k_{22}^{sfrp} = \frac{1 + 2\mu_2 v_f}{1 - \mu_2 v_f} k_m \tag{4.26}$$

where l and d are the length and diameter of the respective fiber, and μ_1 and μ_2 are given as

$$\mu_1 = \frac{\frac{k_{f1}}{k_m} - 1}{\frac{k_{f1}}{k_m} + 2\frac{l}{d}} \tag{4.27}$$

and

$$\mu_2 = \frac{\frac{k_{f2}}{k_m} - 1}{\frac{k_{f2}}{k_m} + 2} \tag{4.28}$$

In Equations 4.27 and 4.28, k_{f1} and k_{f2} are the thermal conductivity of the fiber in the x_1 and x_2 directions. For the work done in this dissertation the carbon fiber is considered to be isotropic, therefore; the thermal conductivity in the x_1 and x_2 directions is considered to be equal.

The micromechanics model compared will also be used for the unidirectional short fiber filled thermal conductivity tensor used in the homogenization derivation for misaligned short fiber composite thermal conductivity.

4.3 Results

4.3.1 Non-Isothermal Non-Newtonian Planar Deposition Flow Models

The free surface minimization approach described in Chapter Three was employed to determine the extrudate shapes for deposition flows of an Isothermal Carreau-Yasuda fluid deposited onto the aluminum print plate (ICY on AL), a non-isothermal Carreau-Yasuda GNF onto the aluminum print plate (NICY on AL), and a non-isothermal Carreau-Yasuda GNF onto a previously deposited fiber filled ABS bead (NICY on ABS). In Figure 4.3 (A), the initial free surface shape for the NICY on AL minimization is shown and the minimized flow shape is shown in Figure 4.3 (B). The initial shapes for the deposition flows are defined by setting design variables downstream from the nozzle exit equal to the bead height and design variables leading the nozzle equal to the expected maximum x value for the flow front. For all flows analyzed the downstream design variables are set as y points equal to 3 mm and x is set as points ranging from -1.5875 mm to −8 mm with a distribution that allows more points near the nozzle exit. The leading curve is set with all x points equal to 3 mm and y points ranging from 3 mm to 0 mm with a distribution that puts more points near the nozzle exit and the translating plate (fewer in the middle of the flow shape).

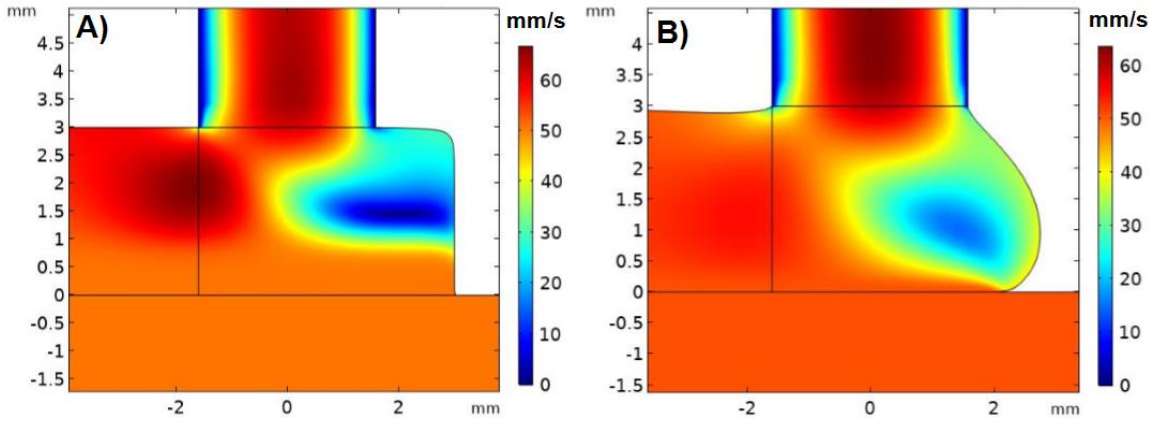

Figure 4.3. Flow Velocity for NICY on AL Flow Domain, A) Initial Extrudate Shape, and B) Final Extrudate Shape

The velocity plots shown in Figure 4.3 do not explicitly show the effect of the non-isothermal and shear dependence of the polymer viscosity, therefore; the plots of polymer viscosity and fluid temperature throughout the fluid domain for NICY on AL are shown in Figure 4.4. In Figure 4.4 (A) the dynamic viscosity of the fluid is presented for the flow domain to show the effects of non-isothermal and shear dependence on the fluid viscosity. In the convergence zone of the nozzle a decrease in fluid viscosity is seen due to increased shear rate. Also, in the straight portion of the nozzle after the convergence zone and upon deposition the viscosity is seen to vary spatially. After deposition, as the deposited bead moves away from the nozzle (this is not inherently true as the model uses a Eularian frame of reference) the viscosity of the fluid against the plate visibly increases with respect to distance from the nozzle as the bead cools through conduction with the plate. The viscosity of the top of the bead is also increasing due to cooling through convection and radiation with ambient conditions, but due to the velocity of the plate (50.8 mm/s) and the small fluid domain length (30 mm from the center of the nozzle) very little cooling has occurred and is not visible without very close inspection of the

upper surface. For an isothermal Newtonian fluid the viscosity plot would be solid for the nozzle and bead domains and solid for the plate with a greater magnitude. The viscosity of the plate appears to be very near the viscosity of the polymer as it cools in Figure 4.4 (A). This is simply due to the reduced range of viewed viscosities so that the temperature and shear dependence of the fluid can be seen. The viscosity of the plate is substantially higher set with a viscosity of $1E8\ Pa \cdot s$ which is far outside the given range. The temperature of the fluid is fairly uniform in the nozzle and immediately after the nozzle exit which is defined by the boundary conditions discussed earlier, but the effect of conduction with the plate is seen as the bead moves farther away from the nozzle exit where cooling of the bead is seen. As with Figure 4.4 (A) the upper portion of the bead is cooling through convection and radiation, but is barely visible without closer inspection due to the described short cooling time seen in this model. The change in temperature in Figure 4.4 (B) is directly related and can be seen in the viscosity in Figure 4.4 (A). The initial shapes for the three flow types studied yield objective function values for Equation 3.5, of 521.6 mm^2/s^2 for the NICY onto AL flow, 654.9 mm^2/s^2 for the NICY on ABS, and 184.1 mm^2/s^2 for the ICY on AL flow.

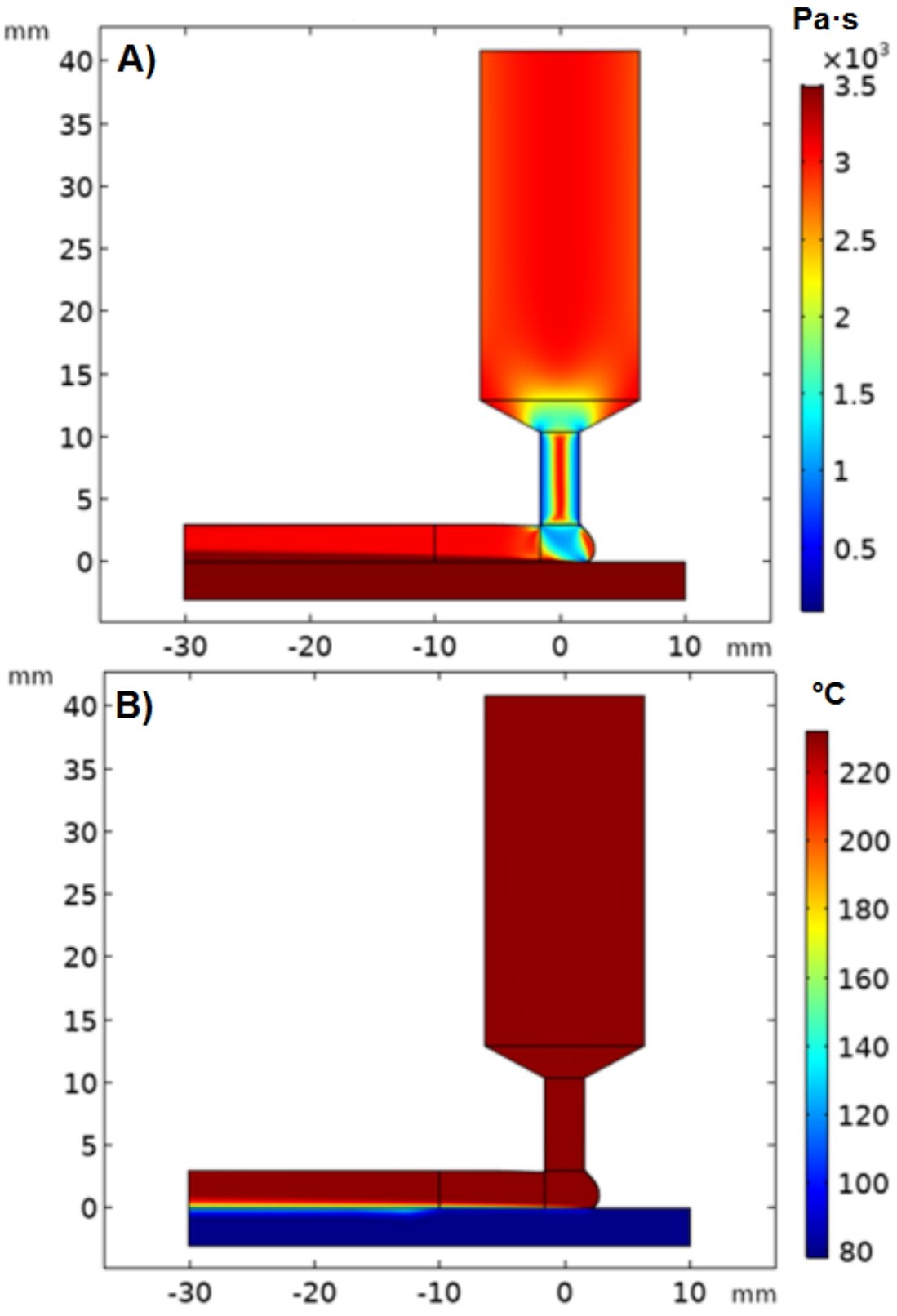

Figure 4.4. A) Viscosity, and B) Temperature distribution for NI-GNF Deposition onto AL Flow Domain

The value of the objective function $f(\underline{\alpha})$ in Equation 3.5 appears in Figure 4.5 as a function of optimization iteration number.

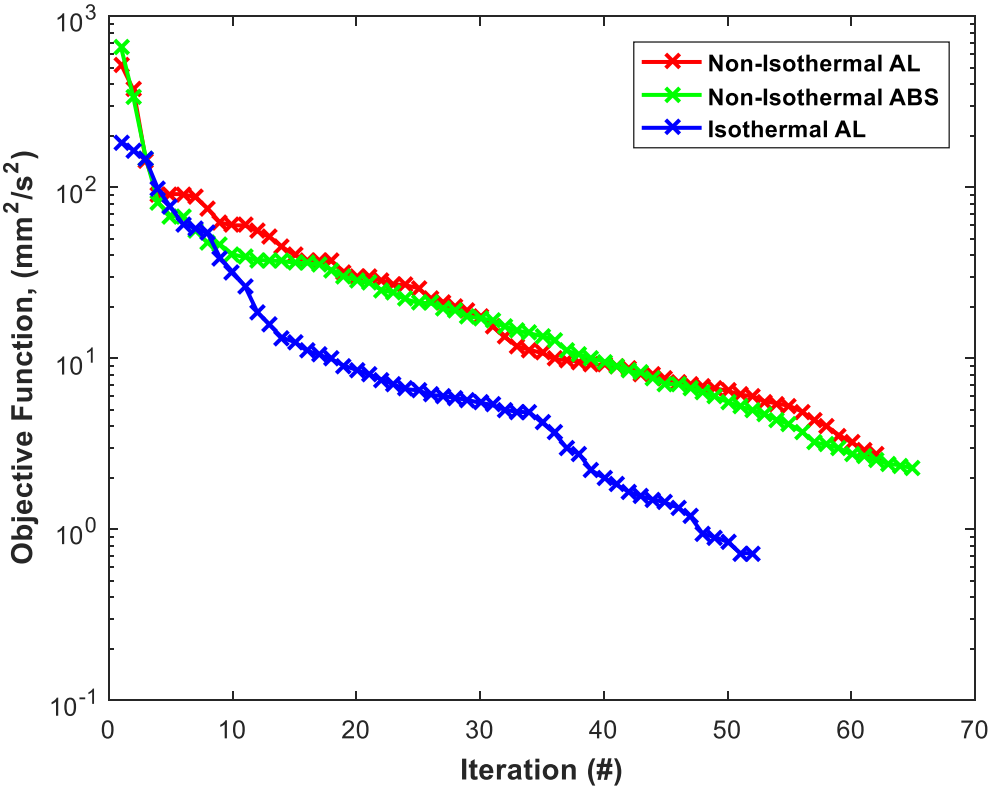

Figure 4.5. Objective Function Iteration History for Deposition Flow Minimizations

The respective objective function values for the three flow types after completion of the minimization are 2.7499 mm^2/s^2 for the NICY onto AL flow, 2.2632 mm^2/s^2 for the NICY on ABS, and 0.723 mm^2/s^2 for the ICY on AL flow, which represents reduction from intial guesses of 99.47%, 99.7%, and 99.6%. The reduction in objective function from the initial guess does not fully represent the accuracy of the minimized flow shape, therefore; the volumetric flow loss is calculated through the minimization boundaries. For the given flow models the percentage of volumetric flow loss through the minimization

boundaries is 0.6 % for the NICY onto AL model, 0.97% for the NICY onto ABS model, and 0.05% for the ICY on AL model. Non-zero minima of the objective function are seen which was explained in Chapter Three and exists in the current simulation as well.

The minimized flow domain shape for the three flow types presented here and the Newtonian result found in Chapter Three are shown in Figure 4.6 (A) and (B) for the leading and trailing boundaries. Increased swell or expansion with respect to the Newtonian flow result is seen for the leading curve for the ICY on AL model. Further expansion is seen when the non-isothermal problem is introduced. Also, there is almost no difference in the flow shapes of NICY on AL and NICY on ABS which is expected as the viscosity of a cooled ABS bead is much higher than the molten polymer that is being deposited making it very similar to the aluminum plate. As a note, while the extrudate swell does increase for the isothermal and non-isothermal Carreau-Yasuda GNF it is not by a substantial amount and will therefore not have a substantial effect on the fiber orientation analysis. The trailing curve for all flow types analyzed is very similar geometrically, therefore; it can be assumed that for the given flow model that increased swell with computationally restrictive viscoelastic models would be seen mostly in the leading curve after the nozzle exit. While the minimization shapes in Figure 4.6 (A) seem to vary more than is stated the range in value of the y axis is approximately 0.14 mm whereas the range in the x axis is approximately 8 mm.

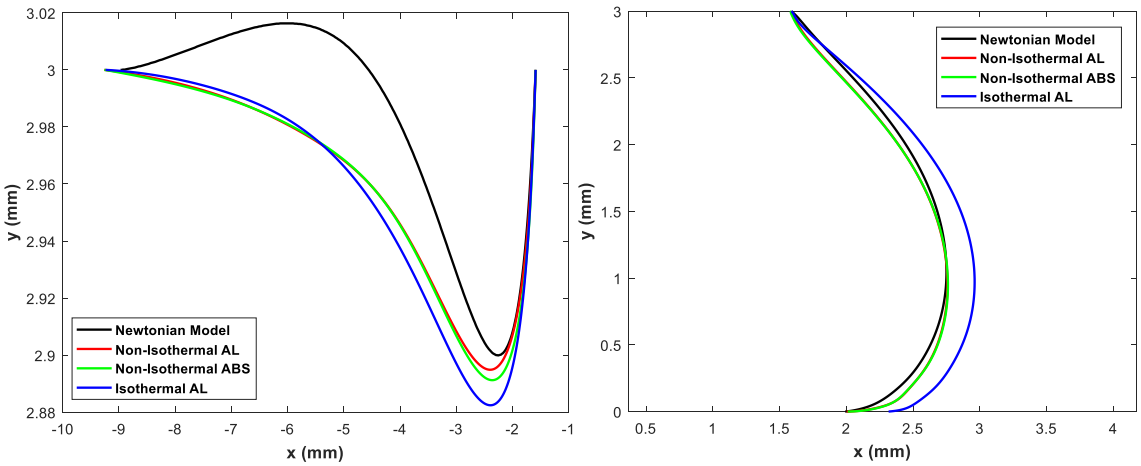

Figure 4.6. Computed Deposition Shape, A) Upper and B) Lower Curves

4.3.2 Fiber Orientation

Once the flow domains for the isothermal and non-isothermal Carreau-Yasuda GNF models have been defined through the described minimization method the fiber orientation throughout the fluid domain can be evaluated. Fiber orientation is evaluated in a very similar way to that presented in Chapter Three, but there are some differences that are introduced as the accuracy of the model has been improved. The first change is the use of the IRD-RSC fiber interaction model rather than the IRD model used in previous works. The RSC model is very similar to the IRD model except for the use of the orthogonal scaling factor kappa, κ, which slows the rate of fiber alignment throughout the flow domain. Accepted values for κ that have been used in literature are 1/30 and 1/10. For this work κ is set as 1/10. The other major changes in fiber orientation modeling have come through a better understanding of the fiber filled ABS material that is being used in the Baylor Large Area Additive Manufacturing printer. The volume fraction of carbon fiber used in previous studies was set as 13% (based on documentation in literature for common LAAM polymer composite materials) whereas the polymer composite material

that is now being used (AS-13CF/000 BLACK, PolyOne Corporation, Avon Lake, Ohio) has a weight fraction of 13%. Using the following equation the weight fraction of fibers can be related to a volume fraction given as

$$V_f = \frac{w_f}{\left(w_f + \left(1 - w_f\right)\frac{\rho_f}{\rho_m}\right)} \tag{4.29}$$

where w_f is the weight fraction of fibers, ρ_f is the fiber density, and ρ_m is the matrix density. For the AS-13F/000 BLACK material being used the ABS material is Lustran® 433 ABS (INEOS Olefins & Polymers, London, UK) which has a density, ρ_m, of 1050 kg/m^3 [124]. The carbon fiber used in the given material could not be defined exactly due to intellectual property issues, but is a PAN based fiber which for chopped fiber composites is expected to be a TORAYCA® T300 (Toray Industries, Tokyo, Japan) or a Hexcel® IM5 (Hexcel Corporation, Stamford, CT) fiber. For the current work we will consider a T300 carbon fiber which has a density, ρ_f, of 1750 kg/m^3 [121]. With the given properties the volume fraction is evaluated as, $V_f = 8.23\%$. Another change in the fiber orientation evaluation is the geometric aspect ratio of carbon fibers in the carbon fiber filled ABS. In a preliminary study by Russell, et al. [125] it was found that weight average of the geometric aspect ratio (length of the fiber divided by diameter of the fiber) of fibers in pellet form is 66.85 and in the printed bead is 53.59. It is expected that with better measurements in future studies that the weight average of the geometric aspect ratio will be in the range of 35-45, therefore for this work a median value of 40 is used. The change in geometric aspect ratio and volume fraction also results in changed C_I, λ, and β values, which using Equations 3.18, 3.12, and 3.13, is evaluated as, $C_I = 0.00405$, $\lambda = 0.9970$, $\beta = 25.732$.

With consideration to the changes stated the fiber orientation is evaluated in the same way as it was in Chapter Three. Forty-six streamlines which are evenly spaced at the inlet progress through the flow domain and are the paths along which the fiber orientation is evaluated. The streamlines are shown with streamline number in Figure 4.8 for the non-isothermal Carreau-Yasuda GNF flow model. The use of forty-six streamlines merits some explanation for the given evaluation. Due to the nature of streamlines several streamlines will terminate without traveling through the entire fluid domain, therefore; forty-six defined streamlines allows for forty streamlines to pass through the entire fluid domain at which the mechanical and thermomechanical properties are evaluated.

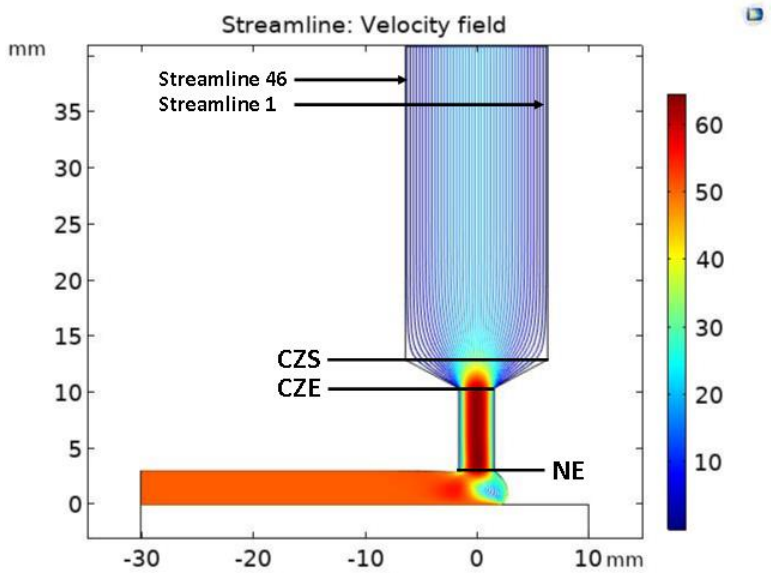

Figure 4.7. Forty-Six Evenly Spaced Streamlines for NICY on AL

Fiber orientation is evaluated throughout the fluid domain by evaluating the velocities and velocity gradients along each streamline. The velocity gradients are used in the evaluation of Equations 3.10 and 3.11, which is then used in to calculate the orientation tensors based on Equation 3.19. The velocities are also used in the evaluation

of pseudo-time development for the fiber filled polymer traveling through the fluid domain and to evaluate the distance, d, traveled along the streamlines in the fluid domain which is used for Figure 4.9.

In the given study four initial fiber orientation tensors are used in the evaluation of fiber orientation development throughout the fluid domain. Three of the initial orientation states that are used given the names $A_{ij,SS}$, $A_{ij,R}$, and $A_{ij,RIP}$ are given as

$$A_{ij,SS} = \begin{bmatrix} 0.0502 & 0.0552 & 0 \\ 0.0552 & 0.8375 & 0 \\ 0 & 0 & 0.1123 \end{bmatrix}$$

$$A_{ij,R} = \begin{bmatrix} 1/3 & 0 & 0 \\ 0 & 1/3 & 0 \\ 0 & 0 & 1/3 \end{bmatrix} \qquad A_{ij,RIP} = \begin{bmatrix} 1/2 & 0 & 0 \\ 0 & 1/2 & 0 \\ 0 & 0 & 0 \end{bmatrix} \tag{4.30}$$

In Equation 4.30 $A_{ij,SS}$ is an orientation tensor which is evaluated by extending the inlet geometry of the nozzle sufficiently far for the orientation tensor to become steady state in the flow domain, $A_{ij,R}$ is the random orientation tensor in the x_1-x_2-x_3 spherical domain, and $A_{ij,RIP}$ is the random orientation tensor in the x_1-x_2 plane. The fourth fiber orientation initial condition is the swirling flow condition which is named, $A_{ij,SF}$, which is the orientation tensor that is derived from the swirling flow model presented by Wang, et al. [60], where the orientation tensor is evaluated at the area in the swirling flow geometry where the inlet of the current model would begin. The orientation tensor values plotted in Figure 4.8 are symmetric about 0 which is due to the fact that the swirling flow model presented by Wang, et al. [60] is axisymmetric and the streamlines do not reach the line of symmetry or the outer radius of the nozzle. The swirling flow is considered the most accurate representation of the extruder based large area additive manufacturing nozzle used in the printing process.

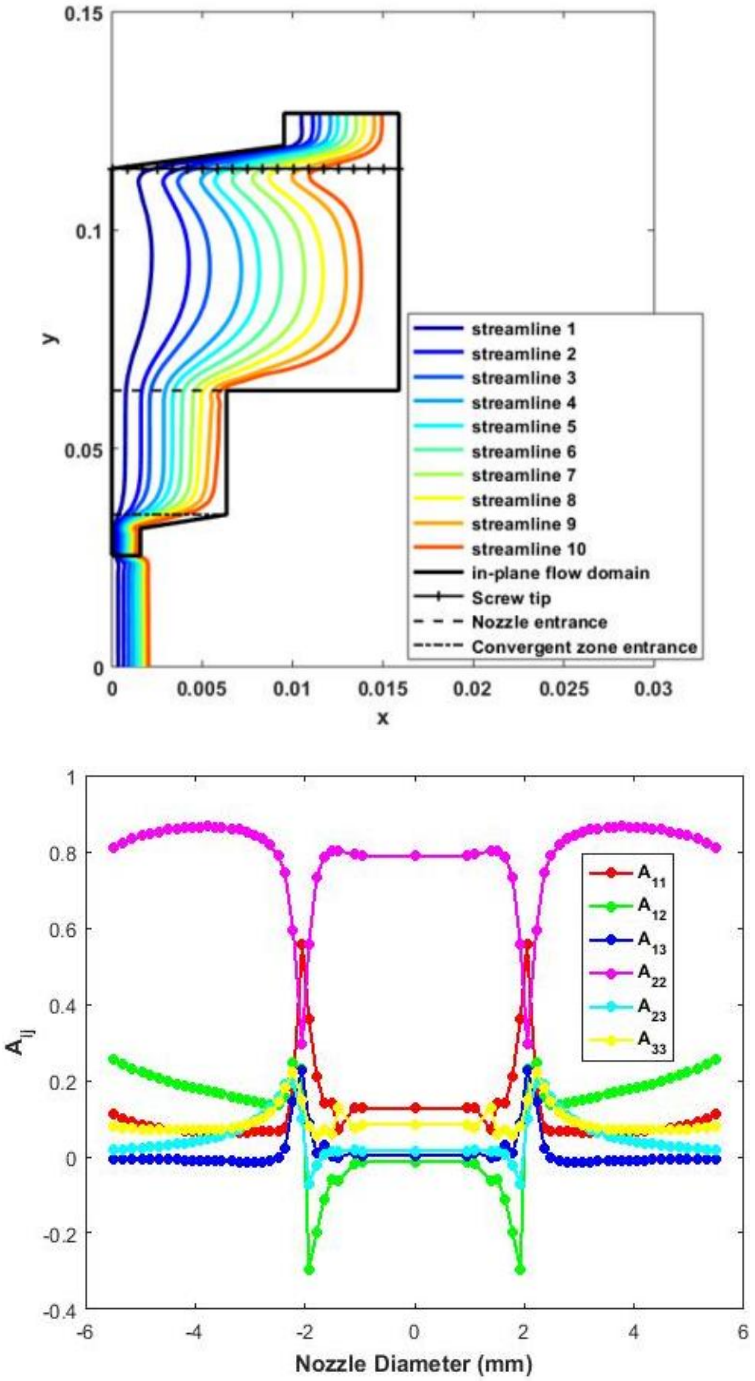

Figure 4.8. A) Swirling Flow Model, Wang, et al. [60], B) A_{ij} with Respect to Nozzle Entrance Diameter

In Figure 4.9 the steady state orientation tensor, $A_{ij,SS}$, is used as it allows for the effects of flow geometry on fiber orientation to be presented most clearly. The A_{22}

component of the orientation tensor which represents the fiber alignment in the x_2 direction is shown in Figure 4.9 (A) starts highly aligned at the nozzle inlet. The fiber alignment increases slightly in the convergence zone of the nozzle (CZS to CZE) from a value of $A_{22} = 0.7751$ to $A_{22} = 0.7883$. There is then a slight decrease in the straight portion of the nozzle after the CZE to NE which is due to pure shear flow that exists in this area. The fiber alignment in this region is trending toward the steady state value set as the inlet condition, which occurs in pure shear flow. There is then a substantial decrease in the fiber alignment in the x_2 direction after the nozzle exit during deposition flow. This substantial decrease in the A_{22} component or the fiber alignment in the x_2 direction corresponds to a substantial increase in the A_{11} component or the fiber alignment in the x_1 direction after the nozzle exit which represents a highly aligned orientation state in the deposited bead. The average fiber alignment value in the deposition direction is, $A_{11} = 0.8029$.

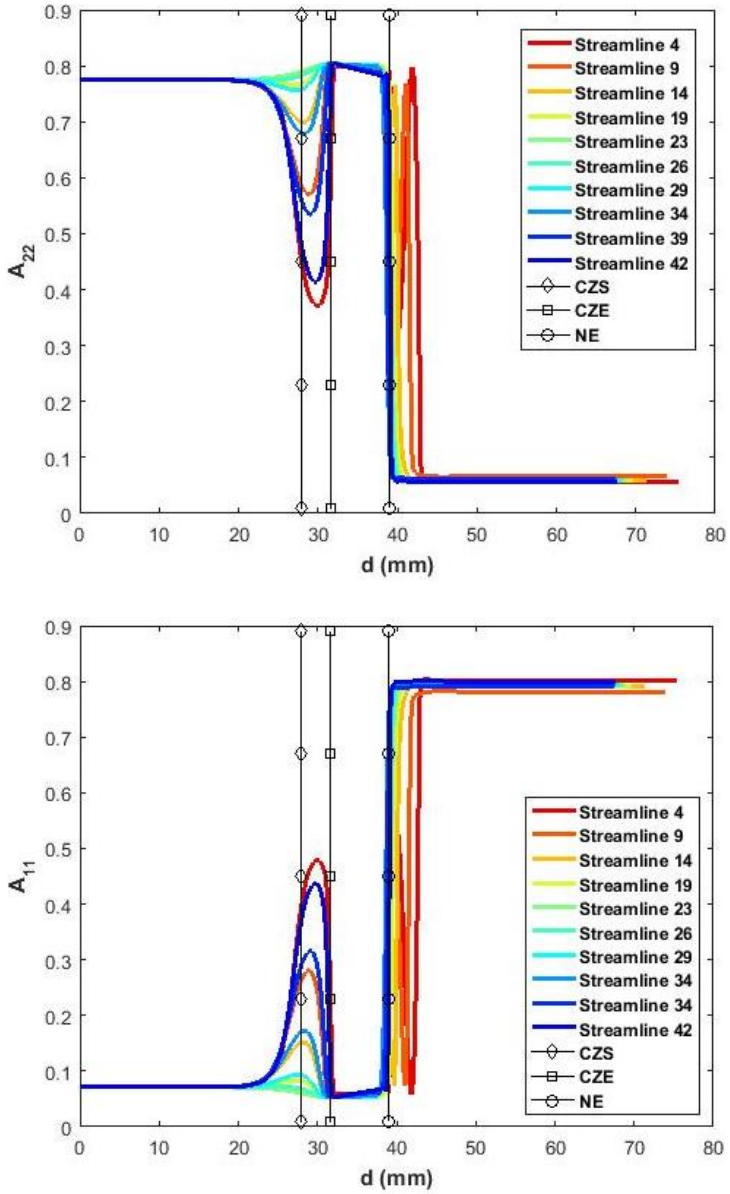

Figure 4.9. A) Fiber Alignment in the y Direction for Level Flow, A_{22}, B) in the x Direction for Level Flow, A_{11}

4.3.3 Mechanical and Thermomechanical Property Evaluation

Once the fiber orientation is evaluated throughout the fluid domain the mechanical and thermomechanical properties of the deposited bead are evaluated using the mechanical and thermomechanical properties of the matrix and fiber constituent materials and the carbon fiber volume fraction, $V_f = 8.23\%$. The matrix material is

Lustran® 433 ABS (INEOS Olefins & Polymers, London, UK) which has a Poisson's ratio, $\nu_m = 0.35$, a Young's modulus, $E_m = 2.55\ GPa$, a linear coefficient of thermal expansion, $\alpha_m = 90\ 1E-6/K$, and a thermal conductivity, $k_m = 0.175\ W/(m \cdot K)$ [124]. The carbon fiber is considered a TORAYACA® T300 (Toray Industries, Tokyo, Japan) PAN based carbon fiber which has a Poisson's ratio, $\nu_f = 0.2$, a Young's modulus, $E_f = 230\ GPa$, a linear coefficient of thermal expansion, $\alpha_f = -0.6\ 1E-6/K$, and a thermal conductivity, $k_f = 3.06\ W/(m \cdot K)$ [121]. Figure 4.10 shows the six independent components of the second order orientation tensor through the bead thickness at the end of the flow domain in the deposited bead.

The six independent orientation tensor components shown in Figure 4.10 for each flow type along with the unidirectional stiffness and coefficient of thermal expansion tensors are used to evaluate the mechanical and thermomechanical properties for all four flow types (NICY on AL, NICY on ABS, ICY on AL, and Newtonian) using Equations 3.24 and 3.25 which are derived using the orientation homogenization method derived by Jack and Smith [13] which has been completed in similar studies [6-9].

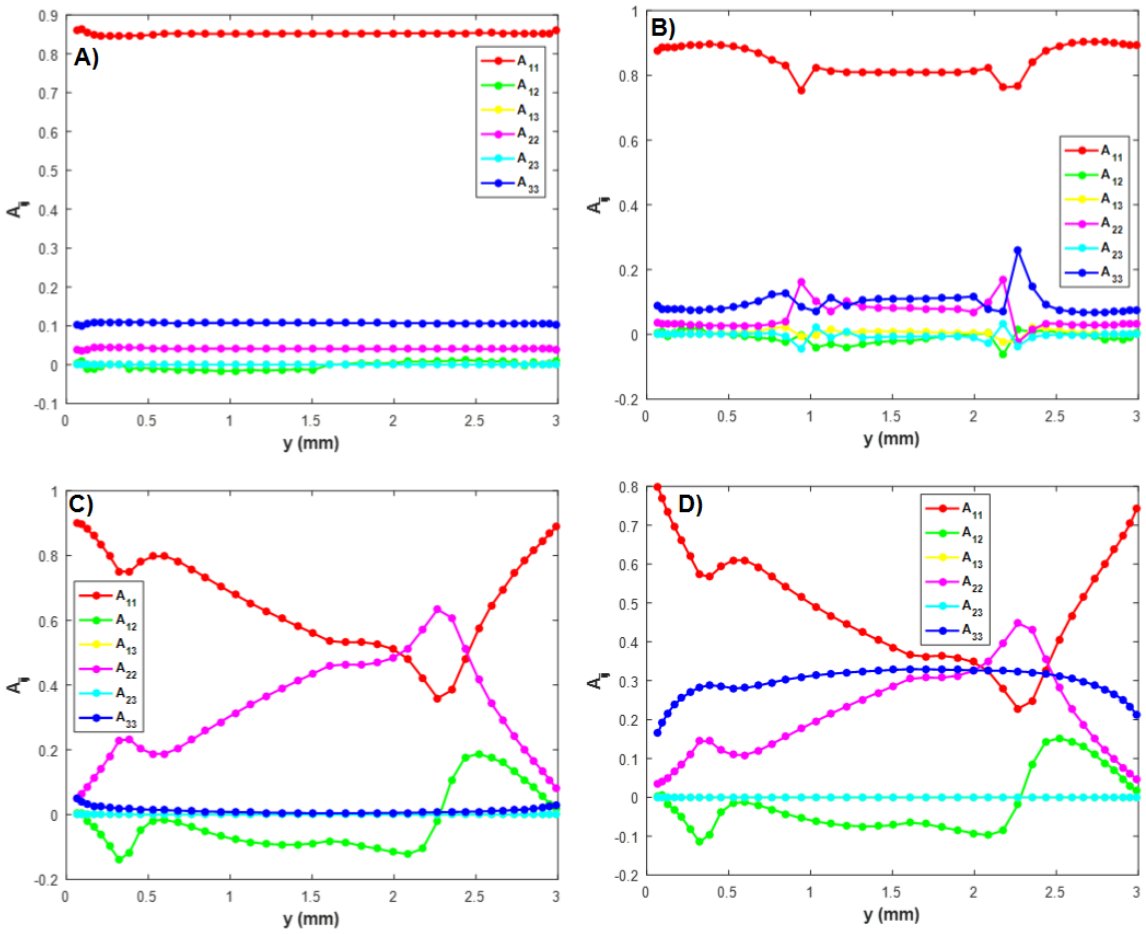

Figure 4.10. A_{ij} Components for NICY on AL in Steady State at End of Deposited Bead for A) $A_{ij,SS}$, B) $A_{ij,SF}$, C) $A_{ij,RIP}$, D) $A_{ij,R}$

In Figures 4.11 and 4.12 the longitudinal and transverse moduli and coefficient of thermal expansion through the bead thickness are shown for the NICY on AL flow type and for the four initial inlet orientation states shown in Equation 4.30 and Figure 4.8. It is known that due to the reduced fiber motion that occurs when using the IRD-RSC fiber interaction model that the initial orientation inlet condition is very important as it strongly influences the final orientation state in the completed part. The highest average longitudinal modulus occurs using the swirling flow initial condition which is considered in this work to be the most accurate initial guess and the lowest average longitudinal

modulus is given by the random orientation initial condition. The opposite is true for the tangential modulus in the deposited bead as is expected for high fiber alignment in the longitudinal direction. The moduli values through the bead thickness for the swirling flow are the most random of all the initial inlet fiber orientation states which is due to the orientation effects of the swirling flow before reaching the nozzle start. Also, for the steady state inlet orientation condition it is seen that there is very little variation through the thickness of the bead. This is due to all streamlines having the same initial A_{11} and A_{22} at the inlet and very little variation in the velocity gradients experienced throughout the flow domain.

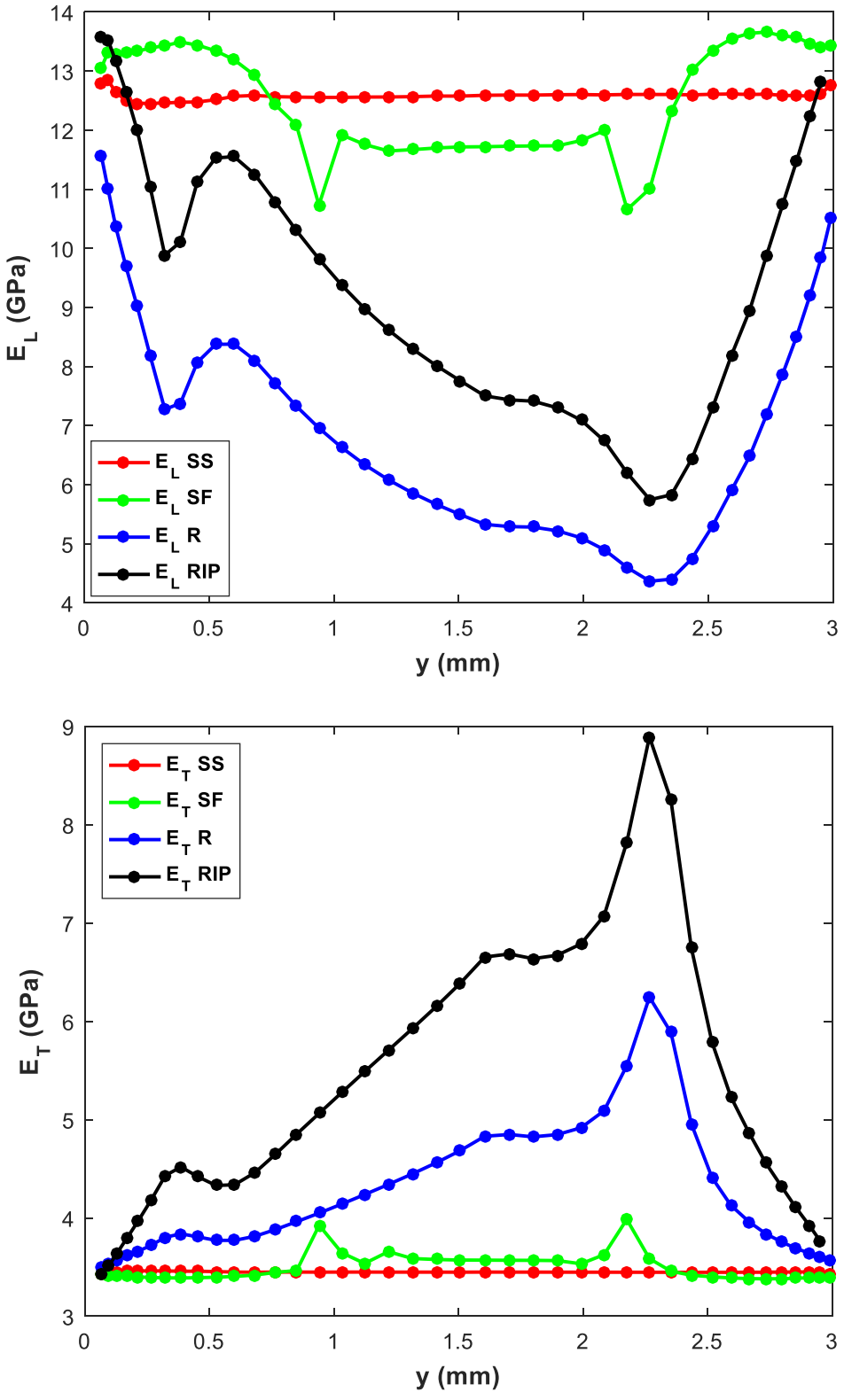

Figure 4.11. A) Longitudinal, and B) Transverse Moduli in the Printed Bead for all Initial Orientation States

The longitudinal and transverse coefficient of thermal expansion for all four initial inlet fiber orientation states are computed using Equation 3.26 are shown in Figure 4.12. It is worth noting the substantial difference between the coefficient of thermal expansion between the Lustran® 433 ABS, $\alpha_m = 90\ E-6/K$ [124], and the TORAYACA® T300 carbon fiber, $\alpha_m = -0.6\ E-6/K$ [121], has been one of the most substantial improvements to the viability of Large Area Additive Manufacturing. The high fiber alignment in the longitudinal direction for the steady state and swirling flow causes a substantial decrease in the coefficient of thermal expansion in the longitudinal direction. The random and in plane random initial fiber orientation conditions see a decreased coefficient of thermal expansion in the longitudinal direction, but it is far less than the other two initial fiber orientation conditions. The transverse coefficient of thermal expansion is reduced due to the inclusion of the chopped carbon fiber but it is to a much lesser degree than the longitudinal coefficient of thermal expansion.

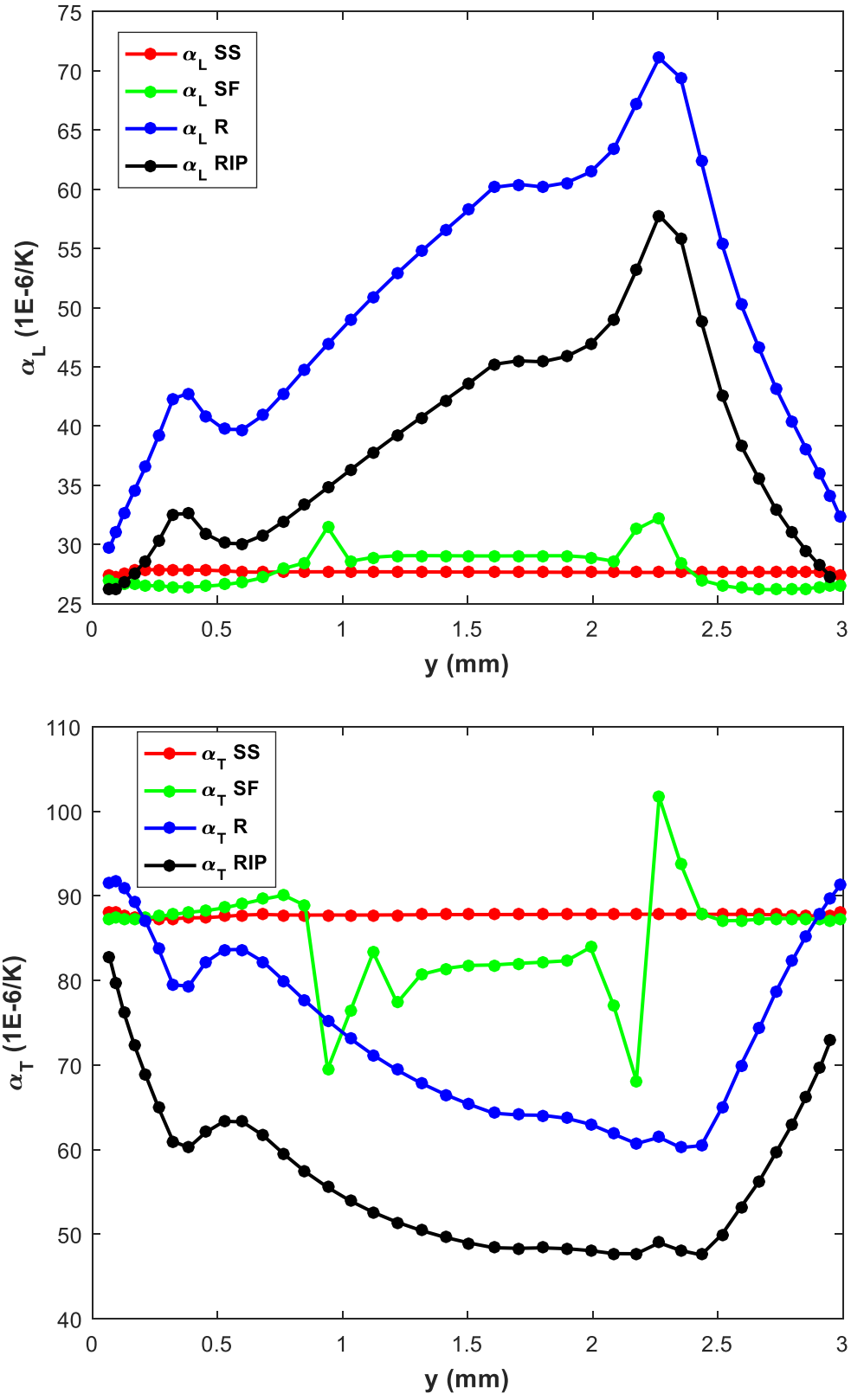

Figure 4.12. A) Longitudinal, and B) Transverse CTE in the Printed Bead for all Initial Orientation States

The thermal conductivity of misaligned fibers in a short fiber filled composite via the orientation homogenization method is evaluated for the first time in the following paragraphs.

The Halpin [79] thermal conductivity micromechanics model for unidirectional short fibers is used in combination with the orientation tensor through bead thickness to evaluate the thermal conductivity tensor for short misaligned fibers using Equations 4.22 and 4.23. In Figure 4.13 (A), the longitudinal thermal conductivity is seen to behave similarly to previous property evaluations for all four initial inlet fiber orientations. The steady state and swirling flow initial conditions return the highest longitudinal thermal conductivity with the random in plane and random orientation initial conditions having successively lower longitudinal thermal conductivity values through the bead thickness. The transverse thermal conductivities for all four fiber orientation initial conditions show average values above 0.21 which is ≈17% higher than values given in literature [31] for Large Area Additive Manufacturing printed beads. The thermal conductivity is still fairly low for the fiber filled composite in comparison to common engineering materials, but a 17% increase to previously published values is non-negligible. This effect can only increase for higher thermal conductivity carbon fiber fillers. TORAYACA® T300 fibers are at the very low end of the range of thermal conductivities (3.06 W/m·K) available for carbon fiber fillers which can see thermal conductivities as high as 1000 W/m·K for commercially available fibers [121].

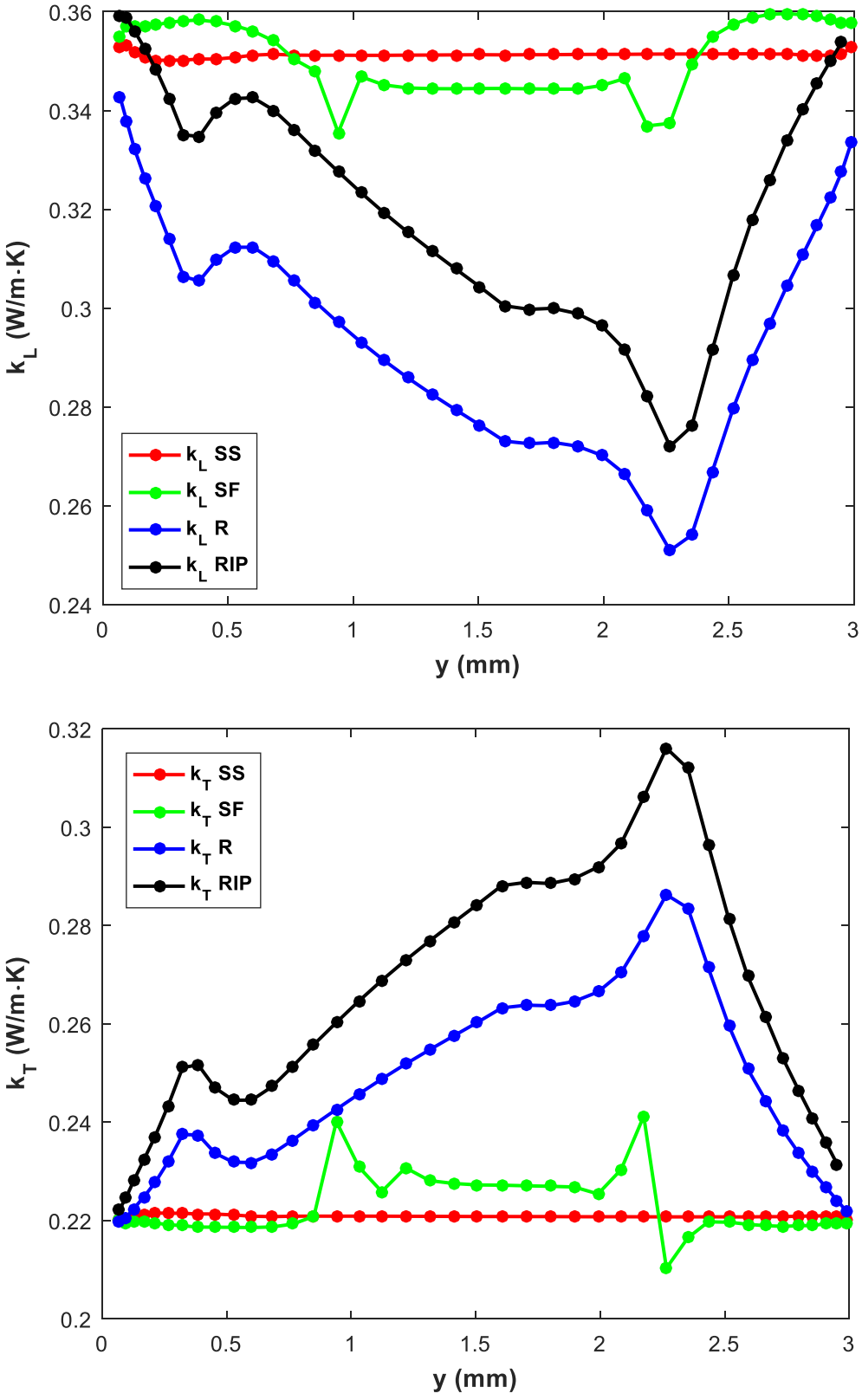

Figure 4.3. A) Longitudinal, and B) Transverse Thermal Conductivity in the Printed Bead for all Initial Orientation States

The average longitudinal and transverse moduli, coefficient of thermal expansion, and thermal conductivities for the four flow types (ICY on AL, NICY on AL, NICY on ABS, and Newtonian), and four initial inlet fiber orientation states (Steady State, Swirling Flow, Random, and In Plane Random) are shown in Table 4.1. The largest variation in properties is shown to be dependent on the initial inlet fiber orientation state which is expected when using the IRD-RSC fiber interaction model. Very little variation is seen in the average properties with respect to flow type which is also expected when looking at the flow shape variation between the four flow models evaluated. Fiber orientation is very slightly effected by the small changes in the amount of extrudate swell after the nozzle exit and this effect is further mitigated by the averaging of properties over the bead thickness. This expectation of very little change was stated in the work by Heller, et al. [7] and is seen in Table 4.1.

Table 4. 1 Mechanical and Thermomechanical Properties in Deposited Bead for all Flow Types and Initial Inlet Orientation Conditions

Flow Model	E_L (GPa)	E_T (GPa)	α_L (1E-6/K)	α_T (1E-6/K)	k_L (W/m·K)	k_T (W/m·K)
NINN CY AL Flow SS	12.47	3.46	27.84	74.45	0.35	0.22
NINN CY AL Flow SF	11.99	3.46	29.57	77.58	0.35	0.22
NINN CY AL Flow R	7.23	4.19	47.38	70.90	0.30	0.24
NINN CY AL Flow RIP	9.78	5.20	33.43	61.51	0.33	0.26
NINN CY ABS Flow SS	12.47	3.46	27.84	74.45	0.35	0.22
NINN CY ABS Flow SF	11.99	3.46	29.57	77.58	0.35	0.22
NINN CY ABS Flow R	7.23	4.19	47.38	70.90	0.30	0.24
NINN CY ABS Flow RIP	9.78	5.20	33.43	61.51	0.33	0.26
INN CY AL Flow SS	11.63	3.51	29.39	74.78	0.34	0.22
INN CY AL Flow SF	12.03	3.41	29.58	76.97	0.35	0.22
INN CY AL Flow R	7.36	4.19	47.00	70.71	0.30	0.24
INN CY AL Flow RIP	9.87	5.17	36.35	61.66	0.33	0.26
Newtonian Flow SS	11.57	3.51	29.47	74.81	0.34	0.22
Newtonian Flow SF	11.97	3.46	29.62	77.30	0.35	0.22
Newtonian Flow R	7.34	4.18	46.73	70.67	0.30	0.24
Newtonian Flow RIP	9.85	5.13	36.25	61.87	0.33	0.26

4.4 Conclusions from Non-Isothermal Non-Newtonian Planar Deposition Flow Model and Property Evaluation

This study presents a computational method for the evaluation of extrudate flow shape for isothermal and non-isothermal Carreau-Yasuda GNF fluids in Large Area Additive Manufacturing. The free surface minimization approach used in previous studies is shown to be effective for non-isothermal non-Newtonian flows. The change in extrudate swell is seen to be greatest for the isothermal Carreau-Yasuda GNF flows with respect to a Newtonian fluid, and to a lesser degree for non-isothermal Carreau-Yasuda GNF flows. The increase in extrudate swell while shown to occur is not substantial when compared to the Newtonian flow shown in previous works. Fiber orientation is evaluated using the IRD-RSC fiber interaction model which greatly reduces the rate of change in fiber alignment and is shown to rely heavily on the initial inlet fiber orientation state. Several initial inlet fiber orientation states are used which represents a range of possible initial orientation states with the swirling flow initial fiber orientation expected to be the most accurate representation of what occurs in the Baylor Large Area Additive Manufacturing printer. Due to the larger aspect ratio (in comparison to previous studies [6, 7]) of fibers in the polymer composite the moduli values are greater than those reported in previous works. The closest moduli values to reported values is that given by the random initial orientation condition, but this is not expected to be the most accurate initial fiber orientation state. The thermal conductivity for misaligned short fibers is evaluated for the first time via the orientation homogenization method. The most important current issue in LAAM printing is the bonding between inter- and intra-laminar deposited beads which has a dependence on the thermal conductivity of the fiber filled composite. Even with very low thermal conductivity carbon fibers, TORAYACA® T300

carbon fibers, values are ≈17% greater in the transverse direction than what has been reported in literature to this point. With higher thermal conductivity carbon fibers the cooling and bonding between successively printed beads will become even more complex.

CHAPTER FIVE

Bead Stack Heat Transfer Analysis in LAAM Polymer Deposition

In this chapter transient heat transfer models for successively deposited beads with and without the addition of infrared preheating are presented. Several bead stack heat transfer models have been created in the past for the polymer deposition process [29-31], but are over-simplified using rectangular elements to represent a bead. Bead stack heat transfer models have been limited to small scale deposition [29, 30], which does not experience the same temperature histories as LAAM due to very small deposition volume. Due to the low thermal conductivity of polymers, the much larger volume of material in LAAM deposition substantially increases the cooling time of deposited beads. Compton, et al. [31] proposed a heat transfer model for fiber filled LAAM polymer deposition parts using a rectangular element stack, but do not include the effect of increased thermal conductivity of fiber filled polymers nor the internal anisotropy existing with highly aligned short carbon fiber filled materials, which will affect the cooling direction and rate of deposited beads.

Infrared heating has been shown to improve bond strength in polymer deposition additive manufacturing [20, 32, 33], but has been applied experimentally. There has yet to be a modeling effort to provide a more fundamental understanding of how heating effects deposition. Results have varied with respect to the improvement of properties and includes the occurrence of strength reduction due to possible polymer degradation. An accurate model for infrared preheating in Large Area Additive Manufacturing is needed

for a basic understanding of the effects on temperature distribution in the heated beads and possible degradation of the polymer at very high temperatures.

5.1 Heat Transfer Model for Multi-bead Deposition and Infrared Heating

In this study, a time dependent heat transfer in solids model is created to analyze the cooling of successively deposited beads in a LAAM printed bead stack. The conservation of energy equation for the transient heat transfer study is given as

$$\rho C_p \frac{\partial T}{\partial t} + \rho C_p \mathbf{v} \cdot \nabla T - \nabla \cdot k \nabla T = 0 \tag{5.1}$$

where ρ is the fluid density, C_p is the heat capacity at constant pressure, k is the thermal conductivity, and T is the temperature which varies with respect to time, t. The properties in Equation 5.1 used in the model are $C_{p,AL} = 896\, J/(kg \cdot K)$, $C_{p,ABS-FF} = 1470\, \frac{J}{(kg \cdot K)}$, $C_{p,IR} = 850\, J/(kg \cdot K)$, $\rho_{AL} = 2700\, kg/m^3$, $\rho_{ABS-FF} = 1050\, kg/m^3$, $\rho_{IR} = 3400\, kg/m^3$, $k_{AL} = 180\, W/(m \cdot K)$, $k_{IR} = 150\, W/(m \cdot K)$,

$$k_{ABS-FF} = \begin{bmatrix} 0.2169 & -0.0027 \\ -0.0027 & 0.2398 \end{bmatrix}.$$

In this study, the two-dimensional simulation domain defined in the heat transfer model includes the aluminum print plate and four carbon fiber filled ABS beads. The geometry of the beads in the single and multiple bead stacks is defined by measurements taken from beads deposited by the Strangpresse Model 19 extruder in the Baylor Large Area Additive Manufacturing printer. A single bead geometry is shown in Figure 5.1 with dimensions of the bead given in mm.

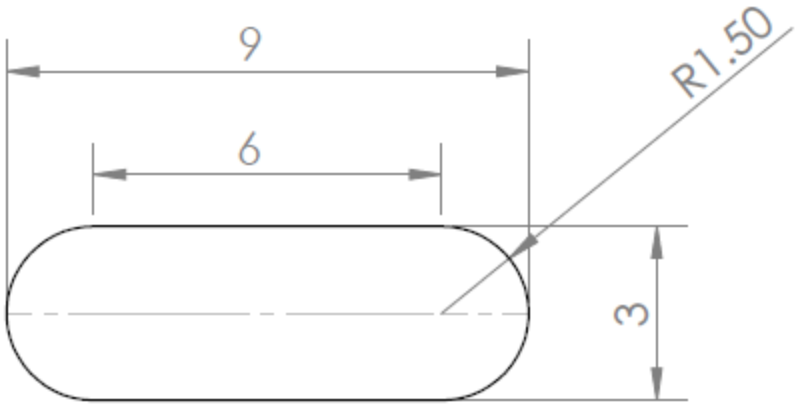

Figure 5.1. Geometry of Typical Bead Deposited by Baylor LAAM Printer, Dimensions are in mm

Each bead is successively added during the simulation one at a time, which is shown in Figure 5.2 using a cross section of a printed specimen, and represented by the dotted lined beads (2, 3, and 4) in Figure 5.3.

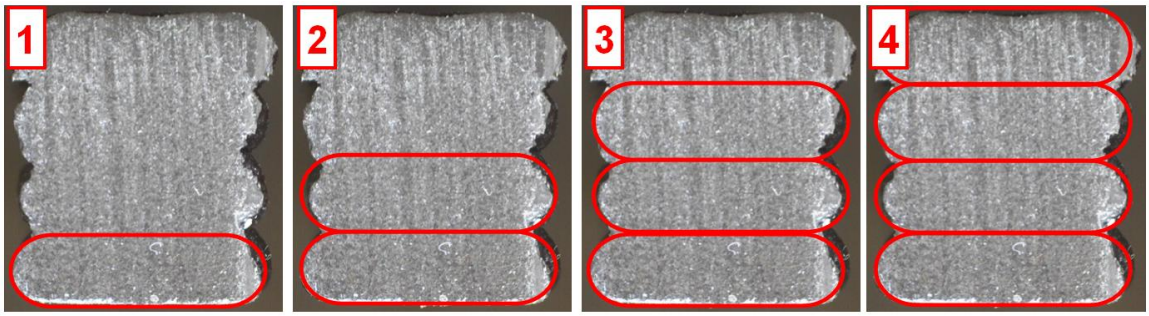

Figure 5.2. Cross Section of a Printed Specimen with Deposition Addition Steps

Between each addition of a bead, we assume a time delay of 40 seconds to allow for cooling as the extruder travels over the print surface, returning to its original position as in the single lap shear sample printing process described in Section 6.2 below. During the cooling process between individual bead depositions, the exterior of the deposited

beads and the aluminum plate cool via convection and radiation heat transfer. The convective heat flux at external surfaces of the bead and print plate is given as [126]

$$-n \cdot q = h(T_{amb} - T) \tag{5.2}$$

where h is the convective heat transfer coefficient from Newton's law of cooling, T_{amb} is the ambient temperature, n is the normal vector from the surface, and T is the surface temperature of the bead and aluminum plate. The radiation heat flux at external surfaces of the bead and print plate is given as [126]

$$-n \cdot q = \varepsilon\sigma\left({T_{amb}}^4 - T^4\right) \tag{5.2}$$

where ε is the emmisivity of the radiative surface, and σ is the Stephan-Boltzmann constant.

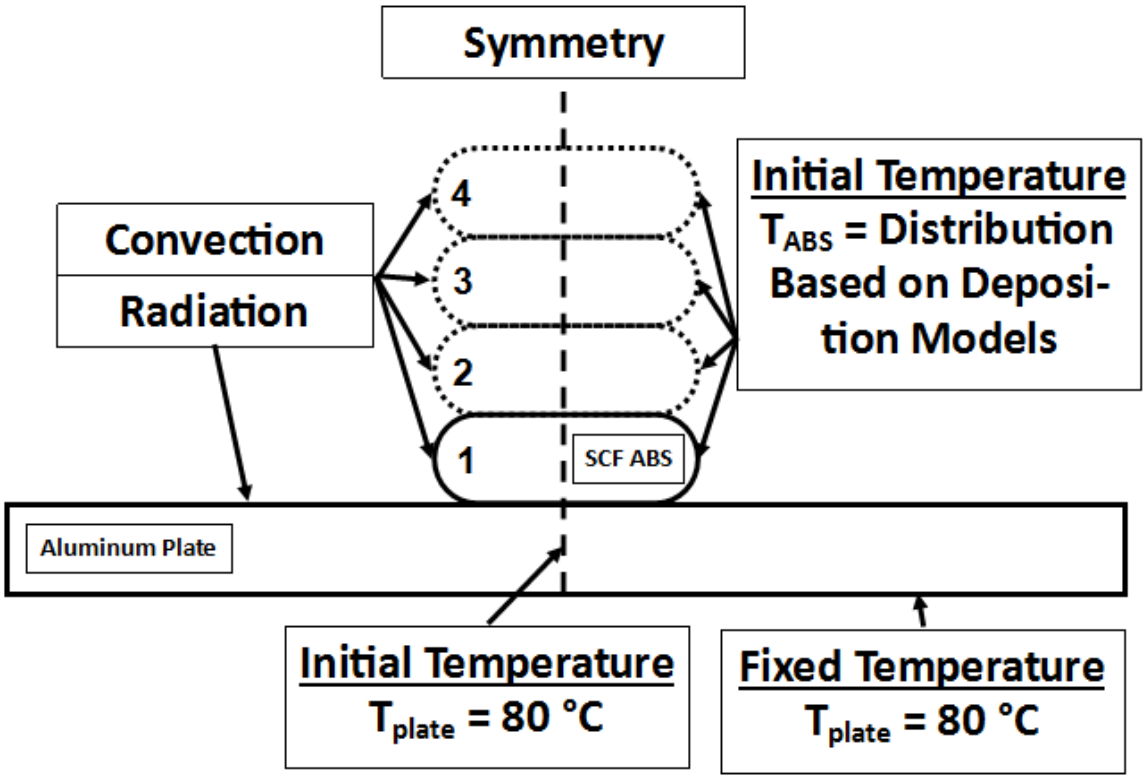

Figure 5.3. Boundary Conditions and Geometry for Multi-Bead Heat Transfer Model

Boundary conditions and a line of symmetry also appear in Figure 5.3 for the transient heat transfer model. Here we only consider a single column of printed beads such that the half symmetry model shown is employed which reduces the computation expense. Convection and radiation is imposed on all external surfaces open to ambient conditions. The convective heat transfer coefficient, h, is set as 13 W/m^2·K. Typical convection heat transfer coefficients for free convection into air are given a range of 2-25 W/m^2·K [126]. A value of 13 W/m^2·K is chosen here which provides for the most accurate comparison with infrared thermography results as shown below. The emissivity for radiation to ambient conditions on the external surfaces in Figure 5.3 are defined as 0.09, for the polished aluminum plate [127], and 0.95, for the black plastic fiber-filled ABS material [127]. An initial temperature is imposed for the aluminum plate at 80 °C and for the deposited fiber filled ABS is defined by the NINN CY AL SF flow model presented in Chapter Four, which is considered to be the most accurate fiber orientation initial condition. The bottom of the plate is set at a fixed temperature of 80 °C to represent the plate heating elements used on the Baylor Large Area Additive Manufacturing printer. In the simulation, each new bead is added at the time of deposition and assigned an initial temperature defined by the NINN CY ABS model presented in Chapter Four. The process used for the addition of sequential layers is shown in Figure 5.5, and described in Table 5.1.

The heat transfer model is initialized by taking the temperature distribution in the y axis through the thickness of the deposited bead which is assigned using the non-isothermal Carreau-Yasuda model that deposits onto the aluminum print plate with the swirling flow initial fiber orientation condition (NINN CY AL SF). The temperature

distribution is then converted to a rectangular plane with the temperature remaining constant in the x axis and follows the distribution given from the NINN CY AL SF in the y axis, which is shown in Figure 5.4 (A). This temperature plane is then used as the initial condition for the first bead of the transient heat transfer bead stack model. The bead is then allowed to cool for 40 seconds (the time it takes to make one pass with the given print geometry that is used in the lap shear tensile testing bond analysis. After, the 40 second cooling time a second layer is added. The temperature field from the single bead model is used as the initial condition for the two bead model, shown in Figure 5.4 (C). The initial condition for the second bead in the stack is evaluated from the non-isothermal Carreau -Yasuda model depositing onto ABS with the swirling flow initial condition for fiber orientation (NINN CY ABS SF). The plate temperature (temperature of the previously deposited bead) is given by a similar temperature plane process as before using the temperature distribution in the y axis from the single bead model, shown in Figure 5.4 (B). This process is repeated until four layers have been deposited and allowed to cool for 40 seconds each. The process is described in Table 5.1 and shown in Figure 5.5. The temperature distribution in steps 1, 3, 5, and 7 in Figure 5.5 appear very similar, but the temperature of the plate is seen to change for each step as it relates to the temperature of the previous bead after 40 seconds of cooling. The temperature of the bead changing for each of the described steps will affect the temperature of the deposited bead and must be considered.

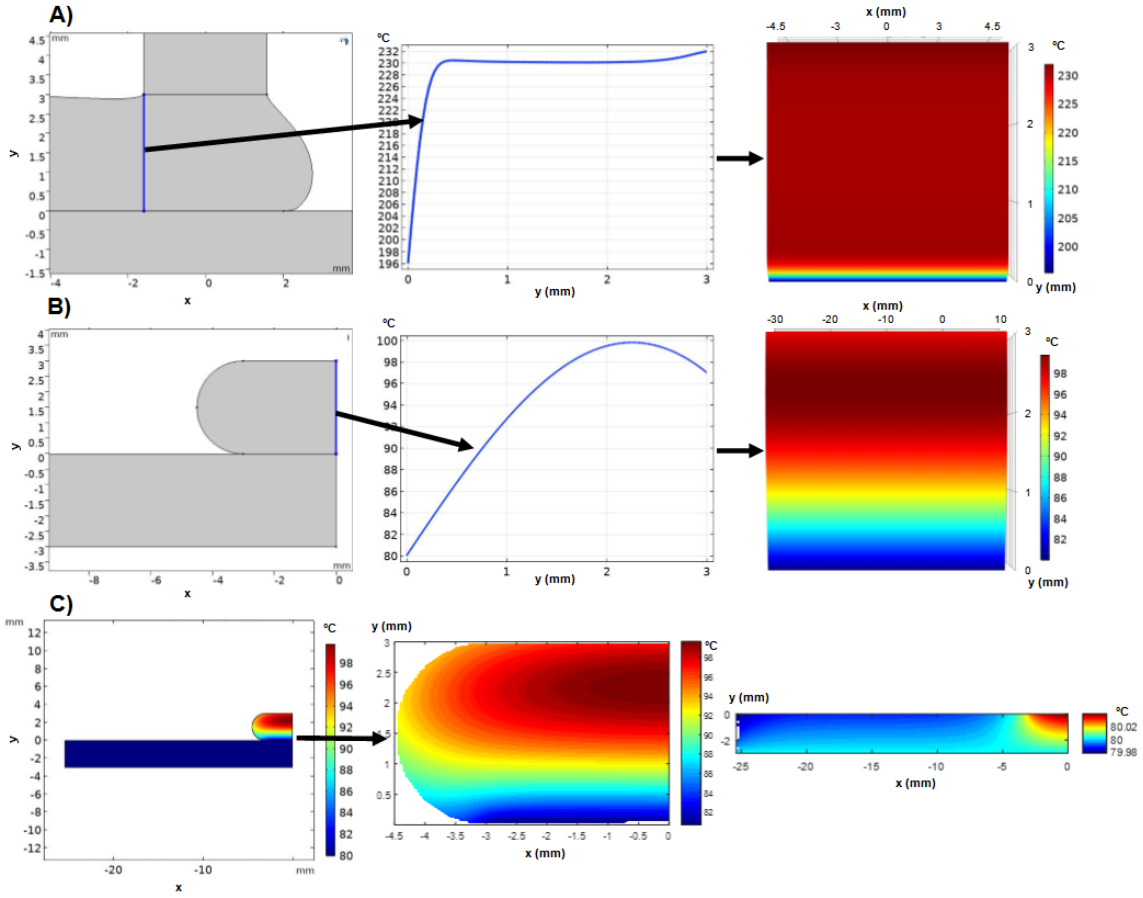

Figure 5.4. A) Temperature Line to Plane Process from NINNCY ABS SF, B) Temperature Line to Plane from Deposited and Cooled Bead, C) Temperature Planes of Bead and Plate from Cooled Bead as Initial Condition to Next Layer

Table 5.1 Heat Transfer Bead Stack Model Process

Step	Time (s)	Step Type
1	0	Temperature Line to Plane from NINN CY AL SF to First Bead, Figure 5.4 (A)
2	0-40	Cooling of First Bead
3	40	Temperature Line to Plane from Bead to NINN CY ABS SF, Figure 5.4 (B)
4	40	Temperature Planes from Bead and Plate as Initial Condition to Second Bead, Figure 5.4 (C)
5	40	New Bead Temperature Evaluated Using NINN CY ABS SF
6	40	Temperature Line to Plane from NINN CY ABS SF to Second Bead, Figure 5.4 (A)
7	40-80	Cooling of Second Bead
		Steps 3-7 Repeated Until Four Layer Stack is Achieved

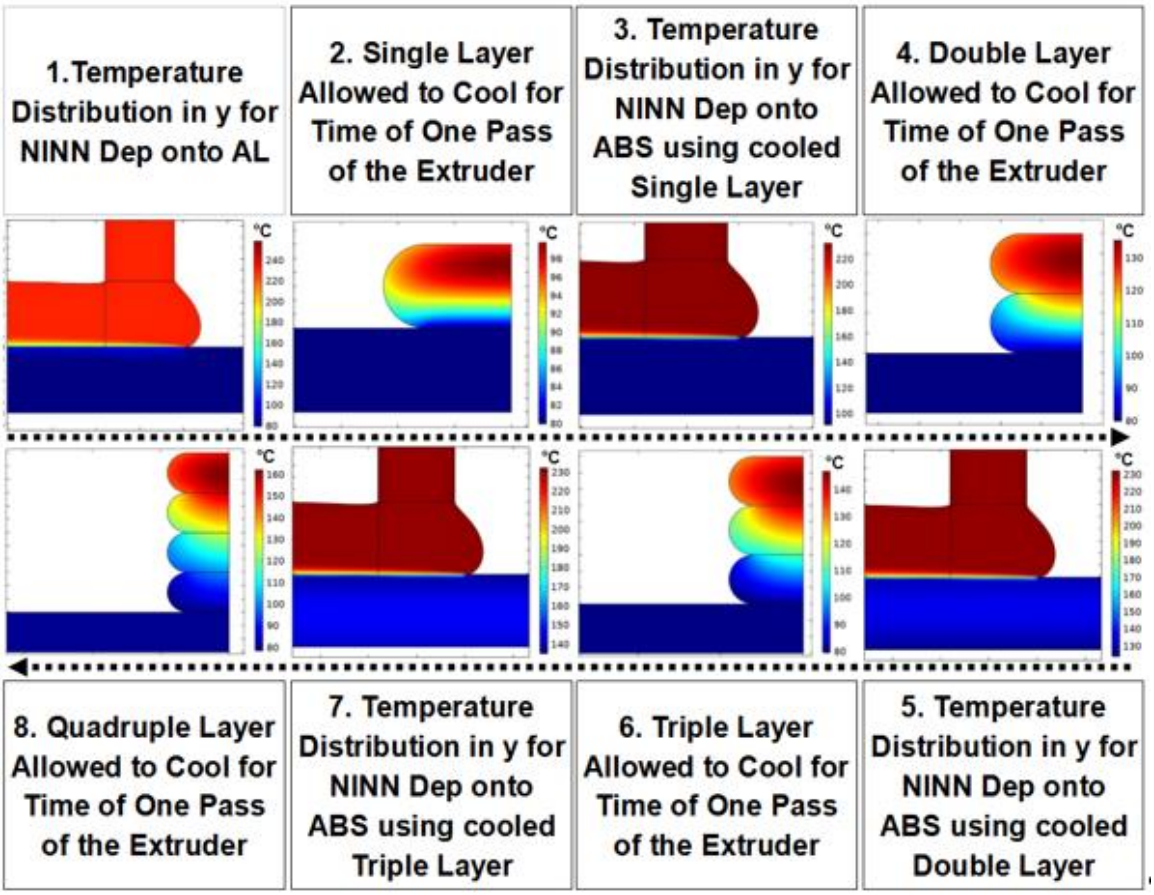

Figure 5.5. Transient Heat Transfer Model for Four Bead Stack Process

Infrared heating of polymer deposition printed beads has been analyzed by several researchers, but only through experimental testing [31-33]. Infrared heating has been shown to cause polymer degradation when not properly controlled and actually decreases bond strength between deposited layers in this case. Therefore, a model is needed that includes the effects of infrared heating that can be used to determine optimum processing conditions for depositing LAAM beads using IR heating.

A second heat transfer model is created to include the addition of infrared heating using a surface-to-surface radiation heat transfer model. An addition to the model in Figure 5.3 is made to include a ceramic infrared heater which is set above the bead stack

and radiates onto the deposited beads and the heated aluminum plate, which is shown in Figure 5.6.

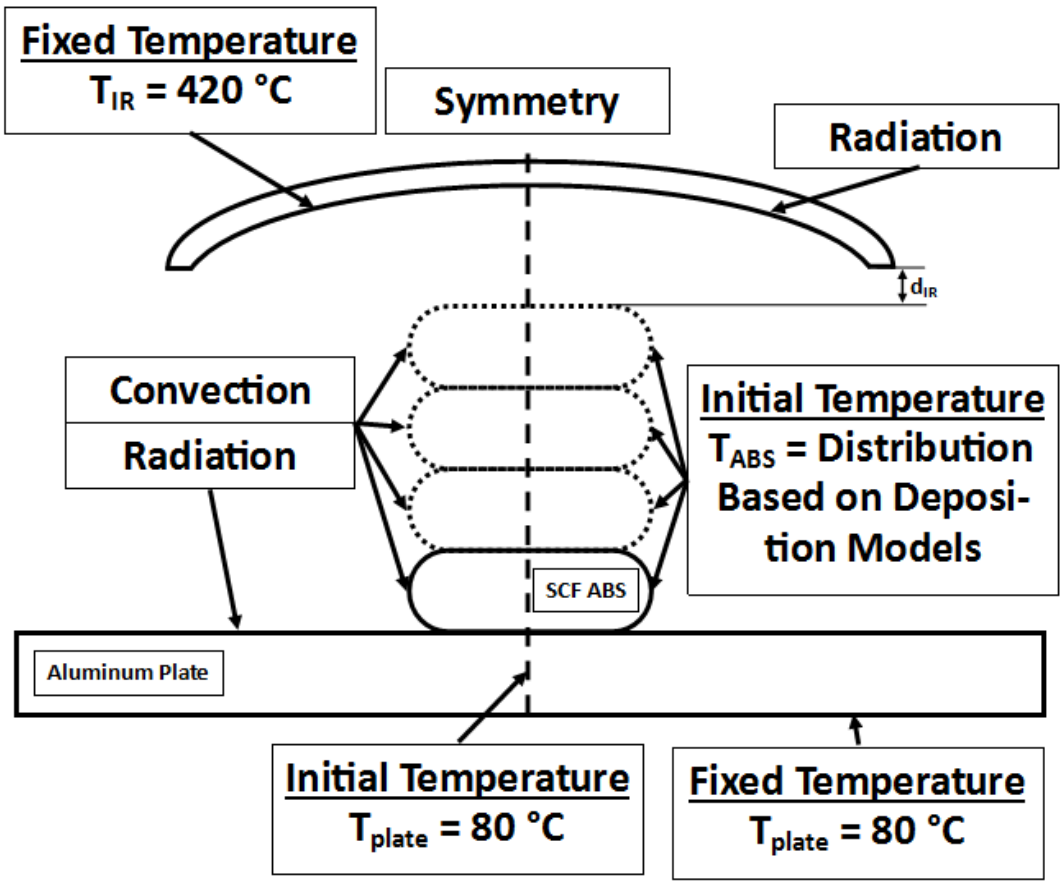

Figure 5.6. Boundary Conditions and Geometry for Multi-Bead Heat Transfer Model with Infrared Heater

The domain and boundary conditions for the infrared heater transient heat transfer model are as given in Figure 5.3 except that elements are added to represent the infrared heater, which is set at a fixed temperature of 420 °C as shown in Figure 5.6. The successive addition of beads described above is modified to account for the time it takes for the heater to pass over a single slice of the bead stack on the print plate. The translation speed of the extruder and the infrared heater is the same as in the deposition

models in Chapter Four as 50.8 mm/s. The infrared heater simulated in the bead heat transfer model developed here is 245 mm in length (based on the Tempco CRB10025, 650 W, Tempco Electric Heater Corporation, Wood Dale, IL), which gives an infrared heating time of approximately 4.8 seconds and a cooling time of 35.2 seconds at an extruder speed of 50.8 mm/s. The deposition of a new bead in our model occurs immediately following the end of radiative heating provided by the infrared heater. The emissivity of the infrared heater is assigned a value of 1 which represents a black body source (defined by Tempco). The infrared heater in Figure 5.6, is defined with a fixed temperature boundary condition, which is set at the maximum attainable temperature in the Baylor LAAM printing device, $T_{IR,M}$ = 420 °C. The infrared heater is fixed at a distance, d_{IR}, from the top of the previously deposited bead, which is set as it is used in the printing apparatus at 12.7 mm, shown in Figure 5.6.

Similar to the transient heat transfer model shown in Figure 5.3, the initial bead temperature is defined using deposited fiber filled ABS from the NINN CY AL flow model presented in Chapter Four. Layers 2-4 are defined by the NINN CY ABS model presented in Chapter Four, but due to the addition of the infrared heater in the model there are extra steps in the process of adding successively deposited beads shown in Figure 5.7 and described in Table 5.2.

The infrared heated bead stack model is completed in much the same way as the previously described method, but there are a few more steps due to the inclusion of the infrared heater. The first layer is allowed to cool for 35.2 seconds, which is the time of the print path (40 seconds) minus the time it takes for the infrared heater to pass over the deposited material (4.8 seconds). The cooled single bead is then used as an initial

condition for the infrared heat transfer model, which is shown in Figure 5.4 (C). The single bead is heated for 4.8 seconds in the model using the infrared heated transient heat transfer model. The temperature distribution in the y axis normal to the deposition table for the infrared heated bead is then transferred into the deposition onto ABS model (NINN CY ABS SF) model using the plane method described before, shown in Figure 5.4. (B). The temperature of the deposited bead is then applied as an initial condition to the second bead in the 2-dimensional bead stack cross section which is allowed to then cool for the specified 35.2 seconds. This process is repeated until the four bead stack is completed. The process described is shown in Figure 5.7 and described in Table 5.2.

Computed temperatures from the two models described above are used to calculate the interlayer temperature between layers 2 and 3, which is where the bond strength will be analyzed experimentally with the single lap shear tensile specimens in Chapter 6.

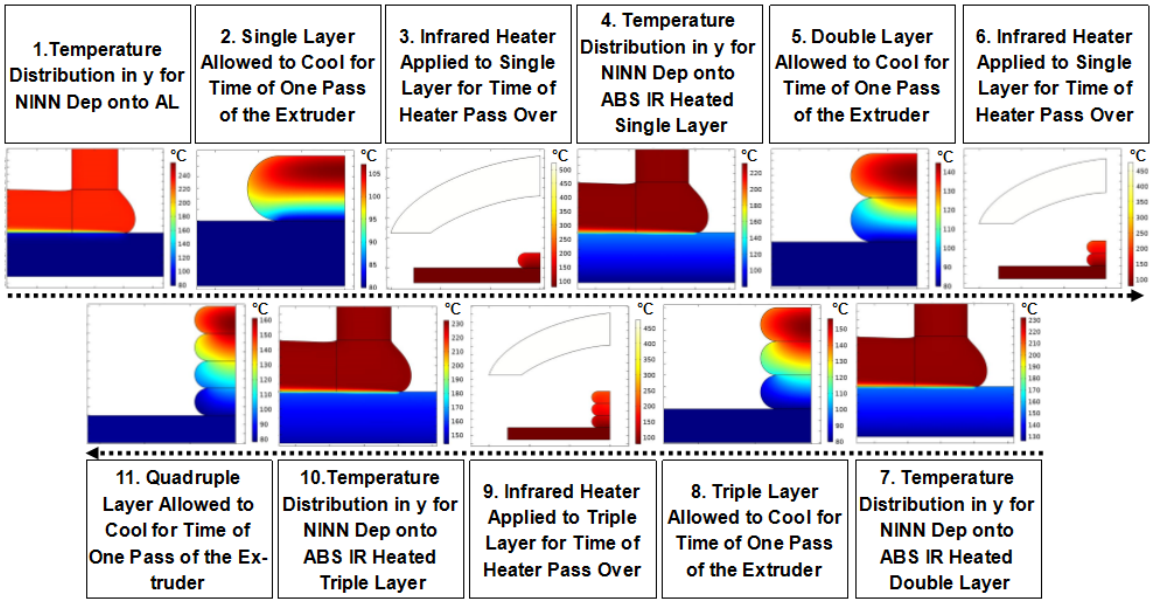

Figure 5.7. Transient Heat Transfer Model for Four Bead Stack Process

Table 5.2 Heat Transfer Bead Stack Model Process with Infrared Preheating

Step	Time (s)	Step Type
1	0	Temperature Line to Plane from NINN CY AL SF to First Bead, Figure 5.4 (A)
2	0-35.2	Cooling of First Bead
3	35.2	Temperature Planes from Bead and Plate to IR Heating First Bead, Figure 5.4 (C)
4	35.2-40	Heating of First Bead with IR Heater
4	40	Temperature Line to Plane from IR Heated Bead to NINN CY ABS SF, Figure 5.4 (B)
5	40	New Bead Temperature Evaluated Using NINN CY ABS SF
6	40	Temperature Line to Plane from NINN CY ABS SF to Second Bead, Figure 5.4 (A)
7	40	Temperature Planes from IR Heated Bead and Plate as Initial Condition to Second Bead, Figure 5.4 (C)
8	40-75.2	Cooling of Second Bead
		Steps 3-8 Repeated Until Four Layer Stack is Achieved

5.2 Results

5.2.1 Heat Transfer Model for Multi-bead Deposition

The temperature distribution for each layer is shown in Figure 5.8. The first layer cools quickly due to conduction with the aluminum plate beneath it. Convection, which cools the bead much more slowly than conduction in this simulation, acts on the portion of the bead open to ambient conditions. The near linear temperature distribution in the y axis in Figure 5.8 (A) occurs due to the substantial conduction with the aluminum plate. The two bead stack in Figure 5.8 (B), has a substantially different temperature gradient than the first layer during cooling. Conduction with a previously deposited ABS layer cools the second bead much more slowly than what was seen when conducting with the aluminum plate. Convection and radiation cool the second bead, but because it does so much more slowly more thermal energy is stored in the second bead. Beads three and four behave very similarly to the second bead and each retains more of the thermal energy over the 40 second cooling time. It is expected that the increased temperature in

beads two through four will allow for increased bond strength due to elevated temperatures for greater periods of time.

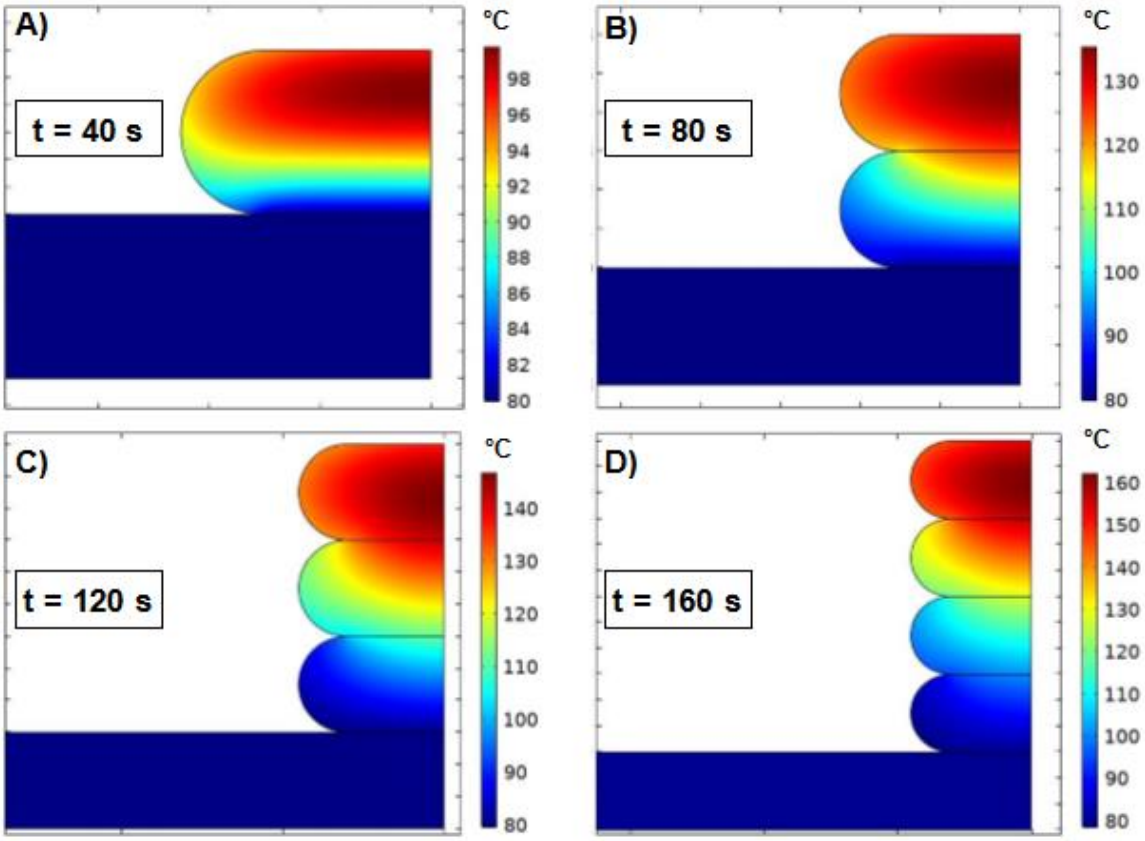

Figure 5.8. Beads 1-4 Cooled for 40 Seconds Each Without Infrared Heater

The temperature history, which is evaluated as the average temperature along the upper boundary of each successively deposited bead, is shown in Figure 5.9. This also represents the interlayer temperature between beads 1-2, 2-3, and 3-4, which is important for interlayer bond evaluation in the LAAM process. The top of each bead starts at approximately 232 °C. This is slightly higher than the defined temperature of 230 °C due to viscous dissipation which occurs in the high shear state regions near the edges of the nozzle at the nozzle exit. The first layer cools to an average linear temperature of 92.7 °C

after 40 seconds. The addition of the second layer increases the temperature at the interlayer line initially then cools for the remainder of the 40 second cooling time between depositions. A decrease in the cooling rate slope is seen at the 1-2 interlayer line with the deposition of the third and fourth beads, but the effect of these beads decreases as the number of layers increases. A similar trend is seen for the interlayer lines 2-3, 3-4, and the top of bead 4 except that the layers cannot cool to the 92.7 °C seen for interlayer line 1 due to conduction with previously deposited fiber filled ABS beads discussed previously. The minimum temperature for the top of each cooled bead before deposition of the next layer is seen to increase in a decaying fashion which leads us to believe a steady state minimum temperature would be reached with the evaluation of more beads in the bead stack.

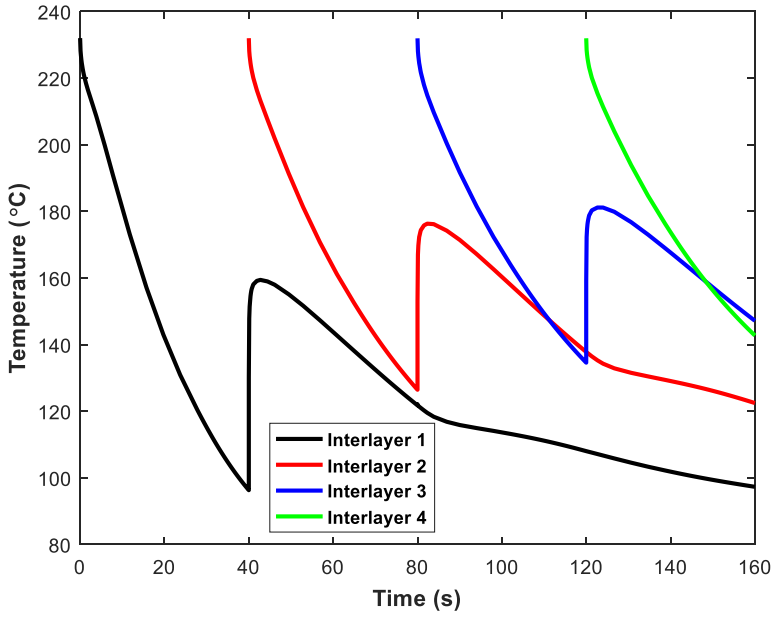

Figure 5.9. Temperature History at Interlayer Bondline for Four Sequentially Deposited Layers

To test the validity of our bead cooling model infrared thermography is used to analyze temperature of the beads during the printing process. A FLIR E95 (FLIR Systems, Wilsonville, OR) infrared camera is mounted above the print platform and the temperature target point is centered on the deposited bead. In Figure 5.10, the FLIR E95 images are compared to the bead stack heat transfer model at a cooling time of 34.2 seconds after deposition. The full cooling time of 40 seconds is not used because the infrared heater impedes the view of the bead after 35.2 seconds and images are taken one second earlier so there are no effects seen from the infrared heater. While the heater is not on at this time it is possible that the much cooler object might distort the image and reading taken by the infrared camera.

The temperatures seen in the infrared heater images in Figure 5.10 differ from the bead stack heat transfer model. This is expected to be due to several issues that make exact modeling difficult, which include changing ambient temperatures immediately around the bead that are most likely greater than room temperature, variation in the actual extrusion temperature, and uncertainty of the FLIR E95 camera which is +/- 2 °C. The exact convection heat transfer coefficient at the bead surface in the Baylor LAAM printer is not known, but is set at 13 W/m·K to match the FLIR E95 images as closely as possible.

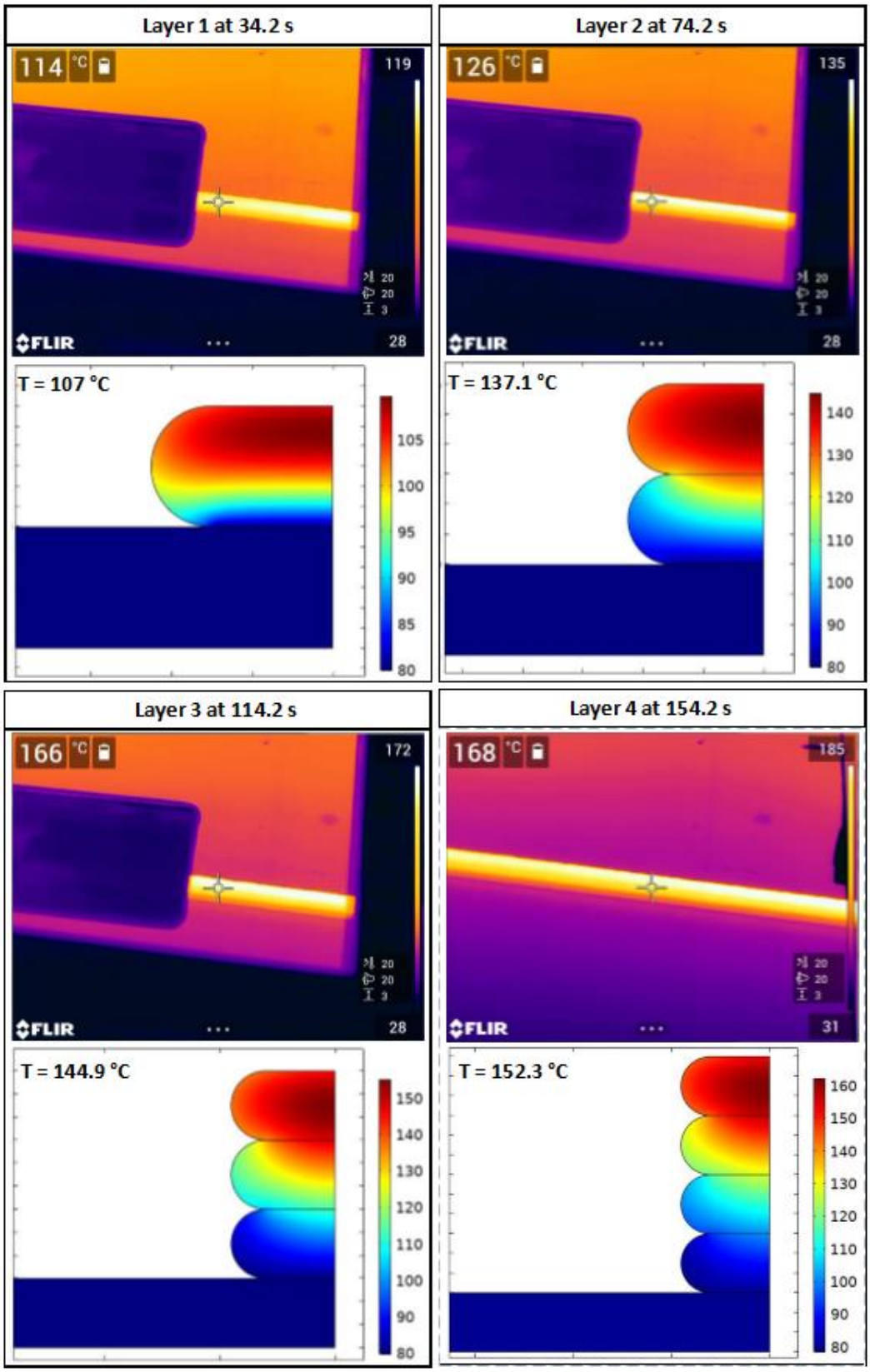

Figure 5.10. Thermography Comparison to Bead Stack Heat Transfer Model

Table 5.3 Percent Difference in Calculated and Measured Temperatures

Layer #	Calculated Temperature (°C)	Measured Temperature (°C)	Percent Difference (%)
Layer 1	107.0	114.0	6.3
Layer 2	137.1	126.0	8.4
Layer 3	144.9	166.0	13.6
Layer 4	152.3	168.0	9.8

5.2.2 Heat Transfer Model with Infrared Heating for Multi-bead Deposition

The temperature distribution with the applied infrared heating is shown for layers one through three in Figure 5.11. The fourth bead in the stack is not analyzed for infrared heating in this model as it is the last layer in the stack and will not undergo heating for the given print process. The temperatures in the bead immediately before the deposition of the following layer are seen to be substantially higher than those in the previous model, as expected. Higher temperatures are seen in the model and it is expected that the increased temperature will improve bonding between the successively deposited layers.

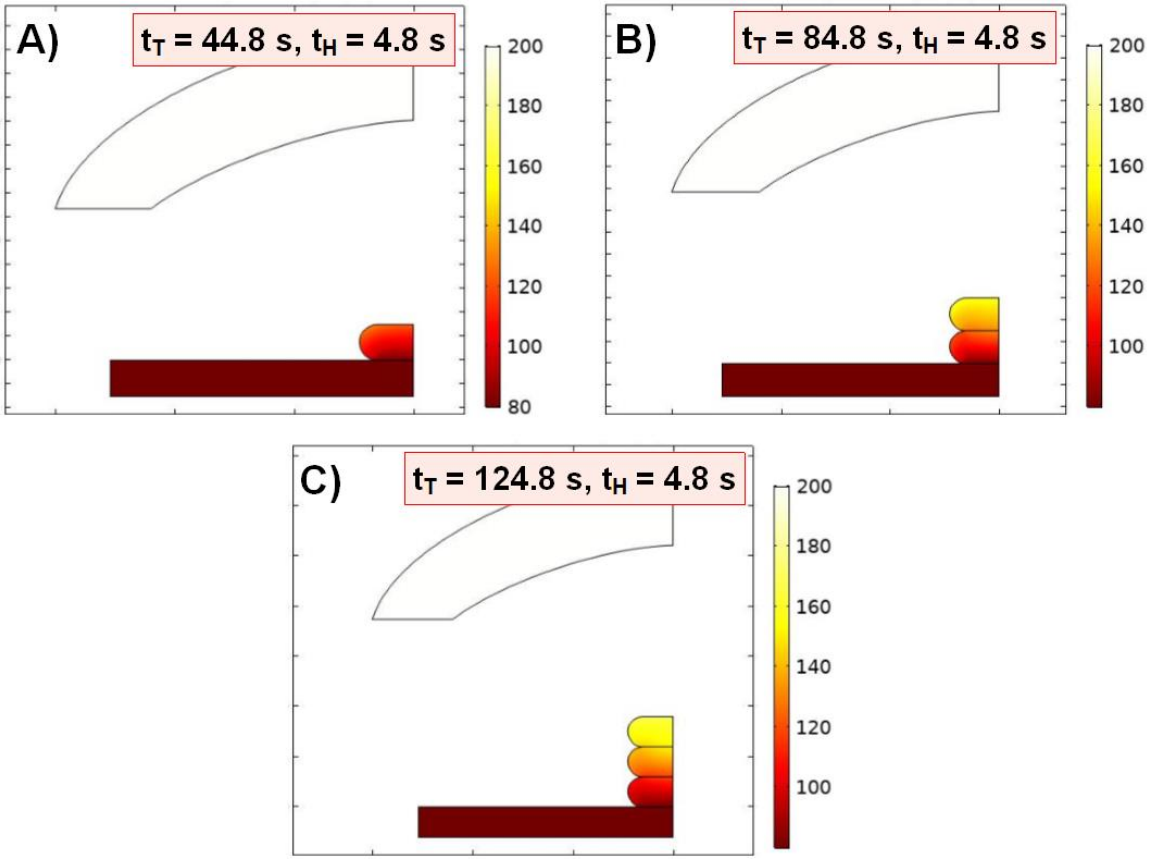

Figure 5.11. Cooling of Four Bead Stack with Infrared Heater

The temperature history of the top of each successively deposited bead is calculated again for the infrared preheated beads as shown in Figure 5.12. Similar to the previously discussed results, the top of each bead starts at approximately 232 °C. The first layer cools to a temperature of 103.6 °C after 35.2 seconds. The addition of the infrared heater increases the pre-deposition temperature to 120.7 °C. The addition of the second layer increases the temperature at the interlayer line initially then cools for the remainder of the 35.2 second cooling time between infrared heating and deposition of the next layer. The infrared heater is seen to have little effect on the 1-2 interlayer temperature after the deposition of the second bead. A similar trend is seen for the interlayer lines 2-3, 3-4, and the top of bead 4 except that the layers cannot cool to the

103.6 °C seen for interlayer line 1 due to conduction with previously deposited fiber filled ABS beads discussed previously.

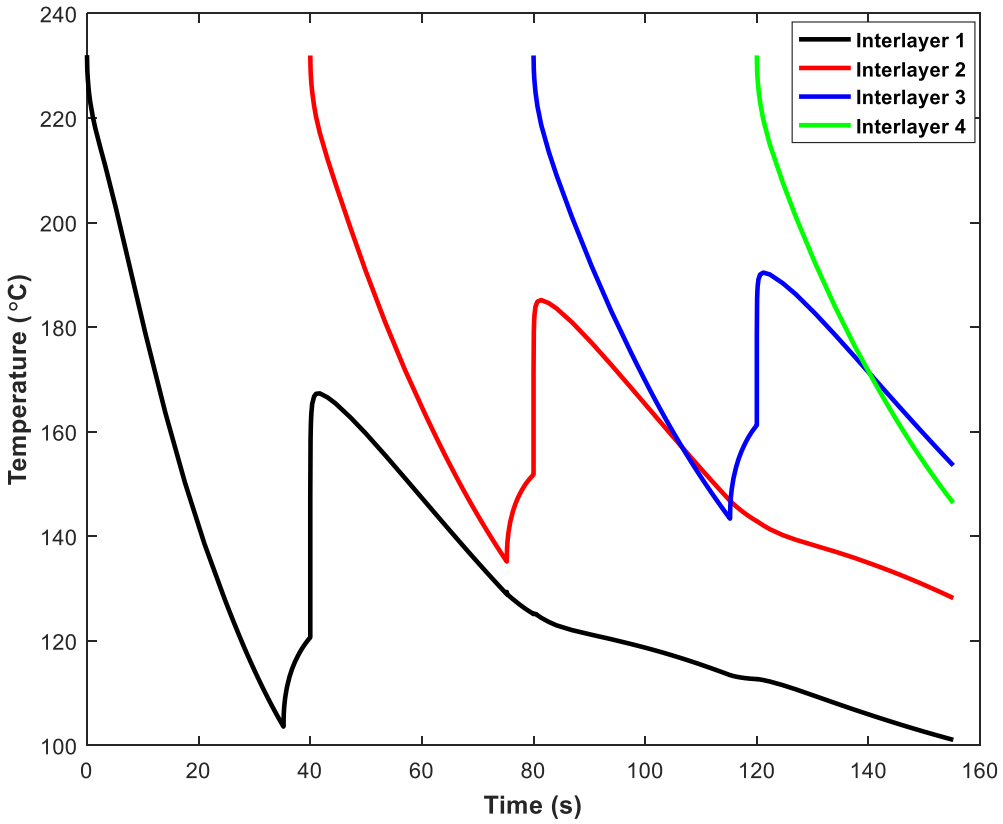

Figure 5.12. Temperature History at Interlayer Bondline for Four Sequentially Deposited Layers

Similar to the previous model, the temperatures evaluated in the model are validated using the FLIR E95 infrared camera. The temperature of the center of the top layer is taken at 34.2 seconds in the same way it was done for the previous model.

The temperatures shown by the model at 34.2 seconds of cooling in Figure 5.13 are again lower than the images captured by the FLIR E95 infrared camera. The previously discussed possible variations exist here, but another consideration must be made when infrared preheating is used. Infrared heating of polymers is affected by

pigments and especially the inclusion of chopped carbon fiber. Carbon fiber filled polymers show increases in temperature due to decreasing the transmission of heat into the polymer [112-114]. This creates a higher temperature shell on the exterior of the fiber filled polymer with the increased heat not reaching the inner portion of the bead. This increased temperature due to decreased transmission of heat in carbon fiber filled polymers is not taken into account for the given model, which causes the prediction to be lower than what is seen with the infrared thermography results. The difference in temperatures again will affect the bond strength analysis in the following chapter.

Another interesting result seen in the thermography images is that the fourth layer actually decreases in temperature in comparison to the third bead. This is considered to occur due to the decreased difference between the deposition temperature and the temperature of the previously deposited bead after infrared heating.

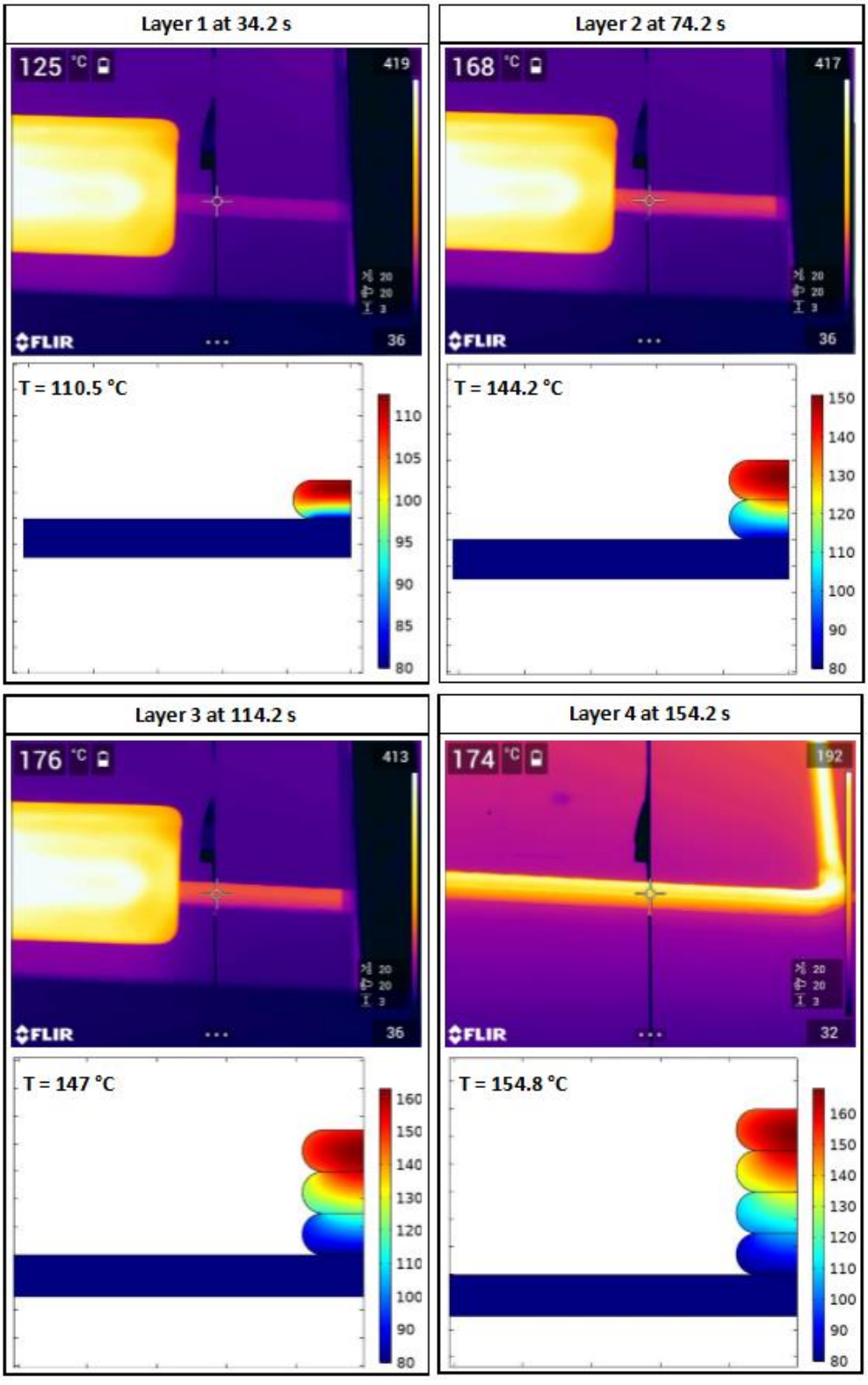

Figure 5.13. Thermography Comparison to Infrared Heated Bead Stack Heat Transfer Model

Table 5.4 Percent Difference in Calculated and Measured Temperatures with Infrared Preheating

Layer #	Calculated Temperature (°C)	Measured Temperature (°C)	Percent Difference (%)
Layer 1	110.5	125.0	12.3
Layer 2	144.2	168.0	14.8
Layer 3	147.0	176.0	18.0
Layer 4	154.8	174.0	11.7

5.3 Conclusions from Bead Stack Heat Transfer Models

This study presents a transient heat transfer model for simulating the temperature response during the deposition of four beads with and without the infrared preheating before the deposition of the next bead. Unlike calculations performed in Compton, et al. [31], the models developed here include the anisotropic thermal conductivity for highly aligned short carbon fiber filled polymers considered in Chapter Four of this dissertation. The actual bead geometry is also used without reducing to rectangular elements.

The first bead deposited is seen to cool quickly due to conduction with the heated deposition plate. As successive layers are deposited the cooling rate slows substantially due to conduction with previously deposited layers of carbon fiber filled ABS which has a much lower thermal conductivity than the aluminum print plate. The infrared preheated layers show increased interlayer temperatures for all deposited beads which will increase the calculated bond strength.

Variation is seen between the heat transfer models and the infrared thermography results captured with the FLIR E95 infrared camera. The differences between computed and measured temperatures may be due to several different factors including the ambient temperature, T_{amb}, greater than room temperature which is used in the given models, variation in deposition temperatures by the extruder in the Baylor Large Area Additive

Manufacturing printer, and uncertainty inherent to the FLIR E95 camera. The addition of infrared preheating of previously deposited layers shows increased difference in bead temperatures which is expected to be due to decreased transmission of infrared heat into the deposited bead creating a hot shell on the heated bead which has been discussed in literature and is not considered in the current model.

The discrepancy in predicted and experimental temperature analysis is expected to have an effect on bond strength evaluation which is analyzed in the next chapter, but the proposed models give an initial platform for the evaluation of cooling in deposited beads.

CHAPTER SIX

Interlayer Bond Strength Evaluation and Experimental Testing for Large Area Additive Manufacturing of Polymer Composites

The strength of large area additive manufactured parts has been to shown to be the weakest in the direction normal to the build platform. This is primarily due to poor bond strength between successively deposited layers which relies solely on temperature and time for the creation bond strength. Prior studies have analyzed the bond strength growth between successively printed layers in FFF printed parts [21, 26], but influence of the temperature history on interlayer bead bonding has not yet been considered for Large Area Additive Manufacturing. In this chapter the bond strength between successively printed layers is evaluated using the computed temperature results from the heat transfer models shown in Chapter Five.

Modifications to the printing process have been employed to increase the bond strength between successively printed layers [10, 20, 31-34], which include pressure application (ORNL z tamper) and heat application (infrared heater, ultraviolet laser, and heated air impingement). In this chapter the addition of a post deposition smooth roller, post deposition textured roller, and infrared pre-deposition heating are considered to improve the strength between successively printed beads through increased bonding and the inclusion of mechanical interlock for the textured roller. The bond strength of Large Area Additive Manufactured printed parts is tested using lap joint specimens printed using the large scale printer that was built at Baylor University. Infrared heating and pressure application after deposition has been utilized in experimental studies [10, 20, 31,

32], and has been used in tandem in large area additive manufacturing on the BAAM system at Oak Ridge National labs [31]. An increase of 200% to the tensile strength of a part built in the z direction was found by Compton, et al. [31], and an increase in 50% in tensile strength was achieved by Ravi, et al. [32]. To the authors knowledge texturing of printed bead surfaces for the creation of mechanical interlock has never been studied in Large Area Additive Manufacturing.

The bond strength improvement between successively printed beads for both models (non-IR heated and IR heated) is evaluated using polymer chain diffusion and intimate contact models from literature [41-43]. Single lap shear tensile specimens printed with a Large Area Additive Manufacturing printer are used to analyze the improvement of bond strength with the print process additions.

6.1 Interlayer Bond Formation Analysis from Heat Transfer Model

Poor interlayer bond strength between stacked layers is one of the most significant issues in polymer and polymer composite deposition additive manufacturing [31], which results in low strength in the direction normal to the print surface. The bond strength, σ, between two of the printed beads in the given study may be defined as a function of temperature, T, pressure, p, and time, t, [42] given as

$$\sigma = f(T, p, t) \tag{6.1}$$

The polymer extrusion deposition printing process creates negligible pressure at the bead-to-bead interface by itself, which hinders the growth of bond strength; therefore, bonding strength is expected to be a function of temperature and time alone without additions to the printing process.

Bond strength growth is defined by healing between mating surfaces between two polymer layers which is governed by the reptation time of the given polymer. Reptation time is defined as the time it takes a polymer chain to traverse an imaginary tube whose boundaries are defined by other polymer chains and additives such as carbon fiber, which is shown in Figure 2.1.

Several models have been proposed for predicting interlayer bond strength between two mating surfaces of layers of the same polymer [25-27]. Wool, et. al. [26, 27] introduced an isothermal relation for the degree of bond strength, D_h, between polymer layers with respect to the ultimate tensile strength of the bonding materials, σ_∞, at a constant temperature, which is defined as

$$D_h(t) = \frac{\sigma}{\sigma_\infty} = \left(\frac{t}{t_r}\right)^{\frac{1}{4}} \tag{6.2}$$

where σ is the strength of the bond, t is the time of bonding, and t_r is the reptation time of the given polymer.

This model is only applicable for a polymer interface that is held at constant temperature during the bonding process, but for many processes such as LAAM printing the polymer cools as bond growth is occurring. Bastien and Gillespie [41] introduced an improved model for polymer bonding via reptation that breaks the bonding time into a number of time intervals, q. During each time interval, $\Delta t = t_{i+1} - t_i$, the average reptation time over the interval, t_r^*,is calculated using the average temperature over the interval, T^*. The improved isothermal model is given as

$$D_h^{BG}(t) = \frac{\sigma}{\sigma_\infty} = \left[\sum_0^{t/\Delta t}\left(\frac{t_{i+1}^{\frac{1}{2}} - t_i^{\frac{1}{2}}}{t_r^*(T^*)^{\frac{1}{2}}}\right)\right]^{\frac{1}{2}} \tag{6.3}$$

The improved model in Equation 6.3 accommodates the evaluation of polymer bond strength with changing temperature with respect to time, but still includes an isothermal approximation over each time interval. Yang and Pitchumani [42] derived a non-isothermal model of polymer bond strength growth via reptation time given as

$$D_h^{PY}(t) = \frac{\sigma}{\sigma_\infty} = \left[\int_0^t \frac{1}{t_r(T)}\,dt\right]^{\frac{1}{4}} \tag{6.4}$$

The integral representation removes the need for isothermal step averaging and more accurately represents the non-isothermal nature of the bonding process. Note that values from Equation 6.3 will approach the values of Equation 6.4 as the time interval, Δt approaches zero, but due to using a time dependent heat transfer finite element model very small time steps will increase computational expense.

The reptation time, t_r, is temperature dependent due to being a polymer chain diffusion process, as is shown in Figure 6.4. Reptation time between a cooling bead-to-bead interface is, therefore; also time dependent based on the rate of cooling

The models discussed previously assume that the bonding surfaces are completely wetted or have intimate contact over the entire surface, and are therefore not applicable when wetting is not insured. This is not the case in almost all fusion bond processes and is especially untrue for polymer deposition additive manufacturing processes. The extrusion process applies negligible pressure at the bond surface which makes the process a temperature and time driven process. The bond growth then must be defined as a function of polymer diffusion through reptation of polymer chains and growth of intimate

contact area, also called wetting. Butler, et al. [43] introduced a model which takes into consideration both wetting and polymer diffusion through reptation which is given as

$$D_h(\tau) = D_{ic}(0)\left(\tau^{1/4}\right) + \frac{\Omega}{5}\int_0^{\tau}(\tau - \tau')^{1/4}\tau'^{-4/5}d\tau' \tag{6.5}$$

where τ is the time of bonding scaled with the reptation time of the polymer given as

$$\tau = \frac{t}{t_r(T)} \tag{6.6}$$

In Equation 6.5, $D_{ic}(0)$ is the normalized bond strength at time, $t = 0$, between the bonding surfaces defined as [128]

$$D_{ic}(0) = \frac{1}{1 + {w_0}/{b_0}} \tag{6.7}$$

where w_0 and b_0 are roughness parameters shown in Figure 6.1.

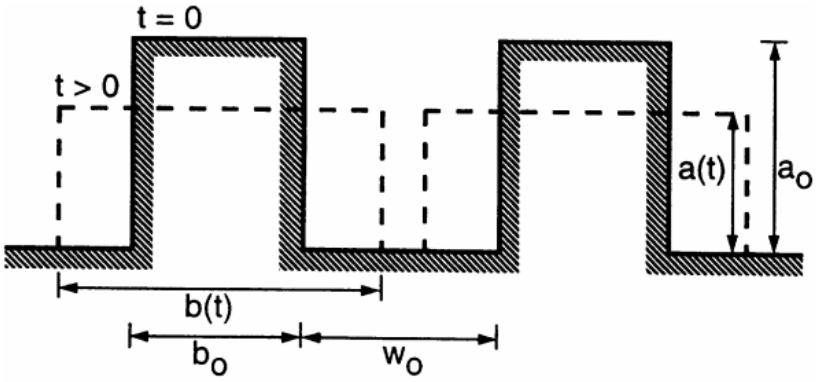

Figure 6.1. Roughness of a Bonding Surface Equivalent Rectangle Model [128]

Also, in Equation 6.5, Ω is defined as a dimensionless parameter that describes the relationship between the characteristic time for full healing and full intimate contact given as

$$\Omega = \left(\frac{Pt_r(T)}{\mu(T)}\right)^{1/5} R_c \tag{6.8}$$

where P is the pressure applied at the contact surface, $\mu(T)$ is the temperature dependent viscosity at the contact surface, and R_c is the roughness parameter based on geometry of the contacting polymers at the bond interface. The Ω function in Equation 6.8 describes the driving force behind the bonding process. If $\Omega > 1$ the bond strength growth is healing through polymer chain diffusion dominated whereas, $\Omega < 1$, implies that the bond strength growth is dominated by the growth of intimate contact.

It is worth noting that integral in Equation 6.5 can be simplified to a closed form solution. The closed form solution was solved in Mathematica (Wolfram Research, Champaign, Il.), and is given as

$$D_b(\tau) = D_{ic}(0)\left(\tau^{1/4}\right) + \frac{\Omega}{5}\left(\frac{\tau^{9/20}\boldsymbol{\Gamma}\left(\frac{1}{5}\right)\boldsymbol{\Gamma}\left(\frac{5}{4}\right)}{\boldsymbol{\Gamma}\left(\frac{29}{20}\right)}\right) \tag{6.9}$$

where $\boldsymbol{\Gamma}$ is the complete gamma function defined as

$$\boldsymbol{\Gamma}(z) = \int_0^\infty t^{z-1}\, e^{-t} dt \tag{6.10}$$

The closed form solution greatly reduces the complexity of Equation 6.5 and allows for easy solution of the bond strength.

6.2 Single Lap Shear Tensile Testing for Bond Strength of LAAM printed Parts

Three additions to the LAAM deposition printing process are proposed in the current work to improve the bond strength in printed bead stacks, and the expected contribution to bond strength is discussed. The first addition to the printing process considered here is the addition of a smooth roller that applies pressure to the deposited

bead immediately after deposition, as shown in Figure 6.2. The effect of the applied pressure can be directly related to the bond strength growth evaluation as shown in Equations 6.8 and 6.9. The smooth roller is also expected to decrease the surface roughness of the printed bead which will aid in the bond strength growth rate as is shown in Equations 6.5 and 6.8. Pressure application to printed surfaces has been investigated by Oak Ridge National Laboratories, where a tamping device applies a rapid and substantial pressure to the printed bead immediately after deposition [10, 20, 31]. Other examples of pressure applications for the printing process are known to exist but have not been discussed in published literature to the authors knowledge and are thus excluded from discussion.

The second addition to the polymer deposition printing process considered here is an infrared heater that precedes the deposition of each new layer of polymer, as shown in Figure 6.2. Infrared heating [31, 32] has been shown to be very effective for improving bond strength by increasing temperature at the bead-to-bead interface. Polymer degradation has been reported to occur with excessive heat application, therefore; care must be taken when adding infrared heating to the print process [31, 32]. The addition of infrared heating is expected to improve bond strength growth in two ways: 1) increased temperature at the polymer interface increases the polymer chain diffusion rate (reducing reptation time) and 2) increased surface temperature decreases the viscosity of the polymer melt which increases the wettability and improves the intial intimate contact area and rate of intimate contact area growth.

The last addition made to the printing process is a textured roller immediately following the smooth roller, as shown in Figure 6.2. To the authors knowledge the

texturing of a polymer deposition process has not been attempted. It is expected that a textured roller will increase the bonding area along the length of the bead. It is also expected that the applied texture will provide a mechanical interlock between layers in the z direction improving the bond strength over the given area.

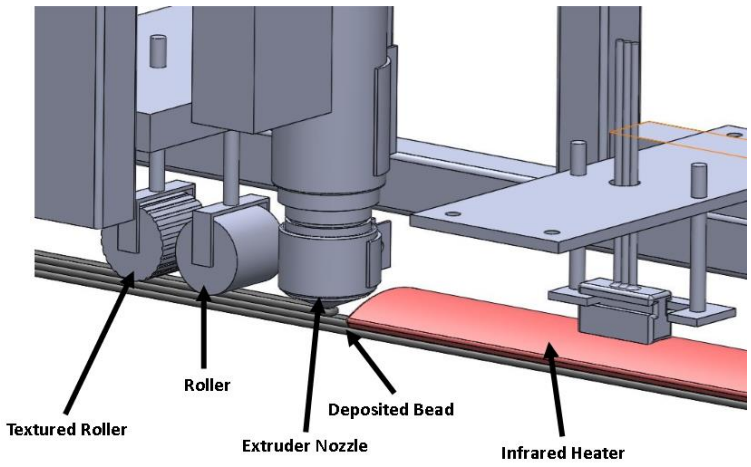

Figure 6.2. Pictorial Image of the Large Area Additive Processing Additions

The effect of the three print process additions described above are evaluated by a custom single lap shear test developed specifically for this purpose using ASTM 3163.03 as a guide. The ASTM 3163.03 standard is not adhered to fully but is used partially for creating a lap shear test suitable for evaluating interlayer adhesion in LAAM beads.

For each test specimen, a PTFE (Teflon) film with a thickness of 0.003” (3 mil) is placed between deposited layers two and three, which is done to limit the bonding area and define the circular bond shape used between successive layers as shown in Figure 6.3. The lines drawn on the PTFE film are used as guides for placement with the previously deposited beads and guides for cutting of the lap shear tensile specimen to prevent cutting through the bond area.

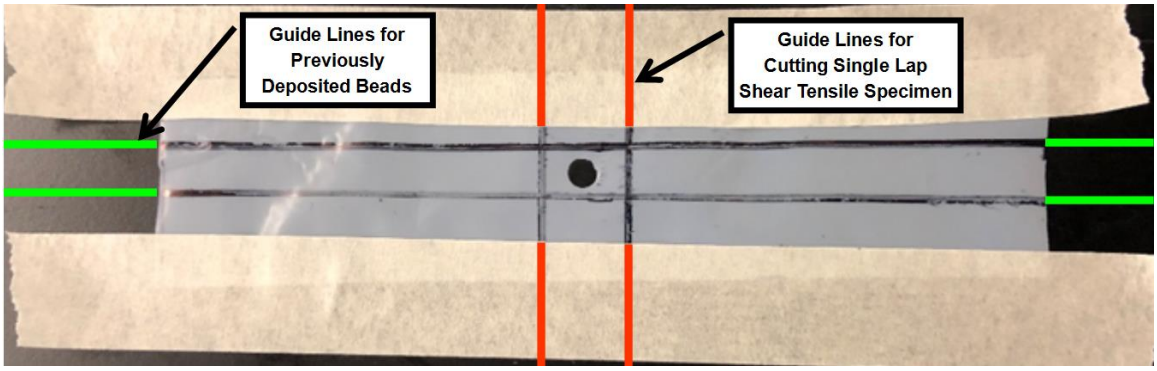

Figure 6.3. Example of Teflon Film Used in Single Lap Shear Tensile Test

The strength of the bond, σ, is then defined as the max load achieved during testing, F, divided by the area of the bond between the layers, A.

$$\sigma = \frac{F}{A} \tag{6.11}$$

6.3 Results

6.3.1 Interlayer Bond Strength Analysis

Bond strength in polymer deposition has been evaluated in literature [24, 29, 30], and due to the complexity of the bonding process a consensus on all effects influencing bond strength has not been made. The bond strength is predicted in this section and a single lap shear bond strength test is run as a demonstration of bond strength growth.

One of the major mechanisms in polymer bonding is the diffusion of polymer chains across the interlayer bond line, which has been described in literature [25-27]. The most important variable describing polymer chain diffusion is the reptation time for a given polymer. The reptation time, t_r, is a temperature dependent property which increases logarithmically as temperature decreases, and nears infinite time at the glass

transition, T_g, of the respective polymer. The reptation time for a given polymer can be found using polymer rheology and is defined as the inverse of the frequency at which the storage modulus, G', and loss modulus, G'' cross. This represents the point at which the polymer transitions from a viscous fluid to a viscoelastic solid.

Lustran 433 ABS was tested with a HAAKE MARS 40 (ThermoFisher Scientific Inc., Waltham, MA) parallel plate rheometer for a temperature range of 180-250 °C at 5 °C increments. Temperatures below 180 °C were problematic for the parallel plate rheometer as the material becomes too viscous and results became highly inaccurate. Lower temperature tests can be run using a rectangular rod test method [130], but is not available in our labs and is cost prohibitive to acquire. An example of the rheological results for the evaluation of the reptation time at a singular temperature is shown in Figure 6.4. For example, Lustran 433 ABS at 230 °C was found to have a crossover frequency of, $\omega = 12.81$ rad/s, which equates to a reptation time of 0.078 s.

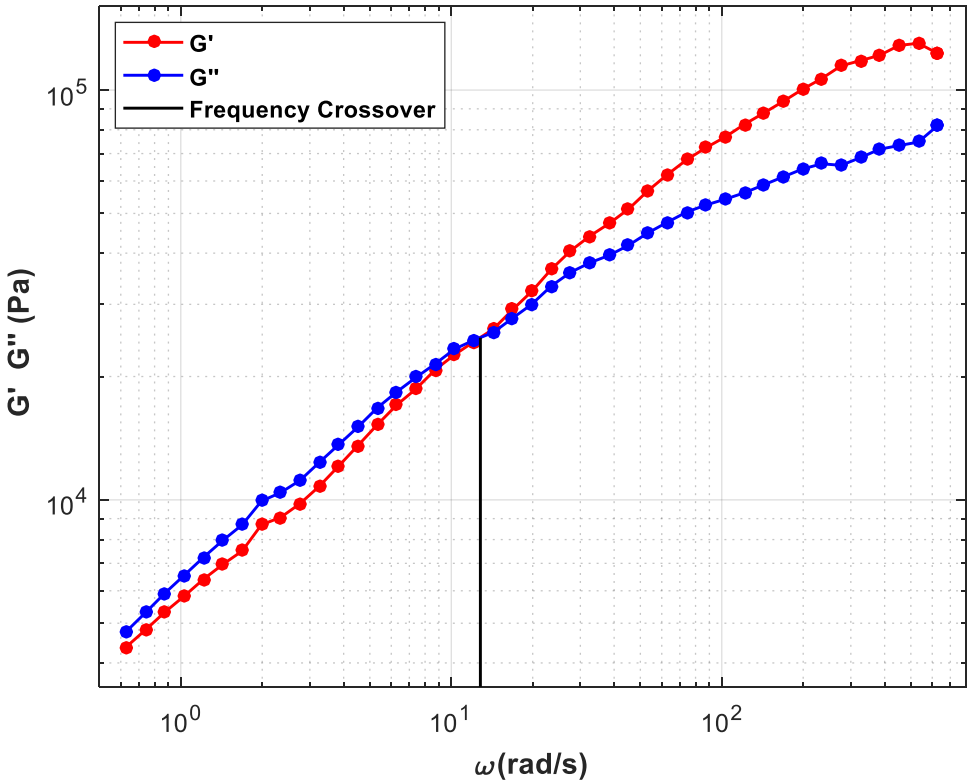

Figure 6.4. G' G'' Crossover for the Evaluation of Reptation Time

The results for the entire temperature range tested are shown in Figure 6.5. Also, shown are results from literature for ABS printing material. The data from Coogan [129] is shown for Cycolac MG47 from Sabic (Sabic Inc.), and the data from Hart, et al. [116] is shown for ABS-M30 from Stratasys (Stratasys Inc.). All data sets are fit using a WLF equation form which is given as

$$\log_{10}\left(\frac{1}{\omega}\right) = -\frac{C_1(T - T_{ref})}{C_2 + T - T_{ref}} \tag{6.12}$$

where C_1 and C_2 are fitting coefficients, and T_{ref} is the reference at which the data intersects zero for the linear regression. The coefficients C_1 and C_2 found for our rheometer data are 4.13 and 116.93 °C. As a note, due to the inability to test below 180 °C, another data point is required to obtain a reasonable curve fit. The point selected for

our data was set at the glass transition temperature, $T_g = 105$ °C, which was measured for our Lustran 433 ABS material using the TA DSC (TA Instruments, New Castle, Delaware), and set at a reptation time value of 10^9 seconds. The selection of 10^9 seconds was used to achieve a similar curve shape to the previously reported data from literature [116, 129].

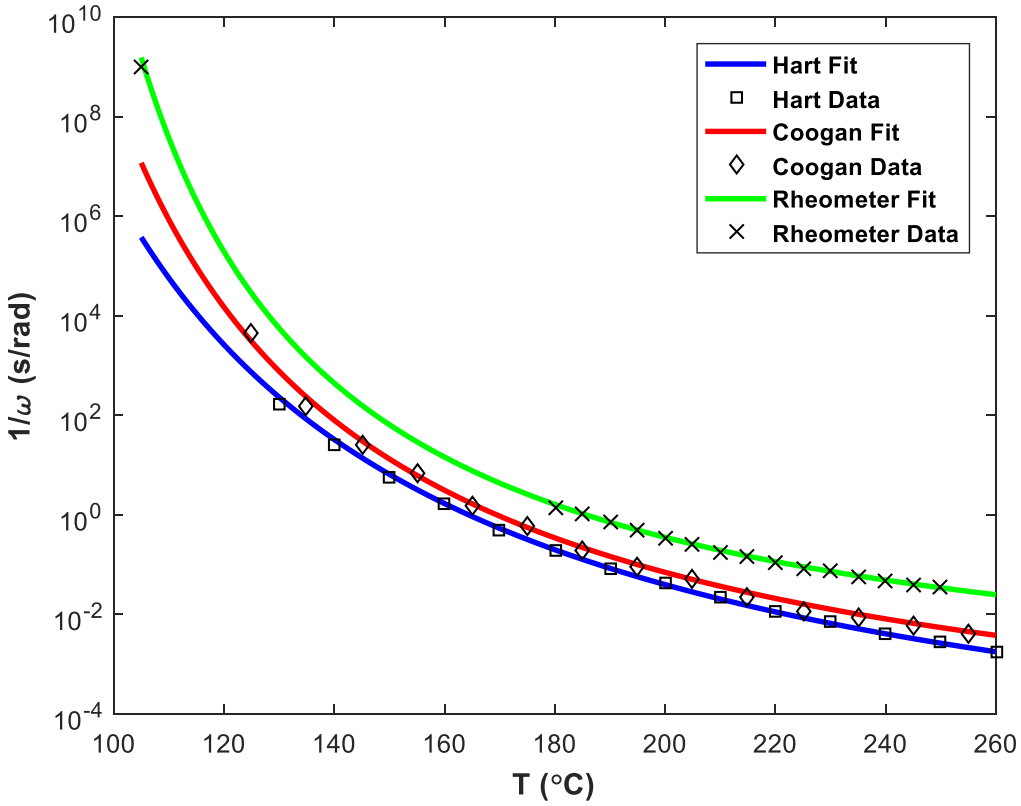

Figure 6.5. Reptation Time with respect to Temperature for Coogan [129], Hart [116], and Rheometer Data

The reptation times shown in Figure 6.5 are used to calculate the bond strength with respect to time between successively deposited beads using Equations 6.3, 6.4, and 6.9. The temperature with respect to time between layers is needed to complete the bond strength calculation. We are interested specifically in the time temperature history

between beads two and three which is the interface tested in our single lap shear tensile tests. The temperature histories are evaluated at six points along a line across the width of the interlayer bond given for the geometry shown in Figure 6.6 as y = 6, x = -3, -2.4, -1.8, -1.2, -0.6, 0. Symmetry is used in both the transient heat transfer models and our bonding calculation resulting in 11 points at which the bond strength is calculated.

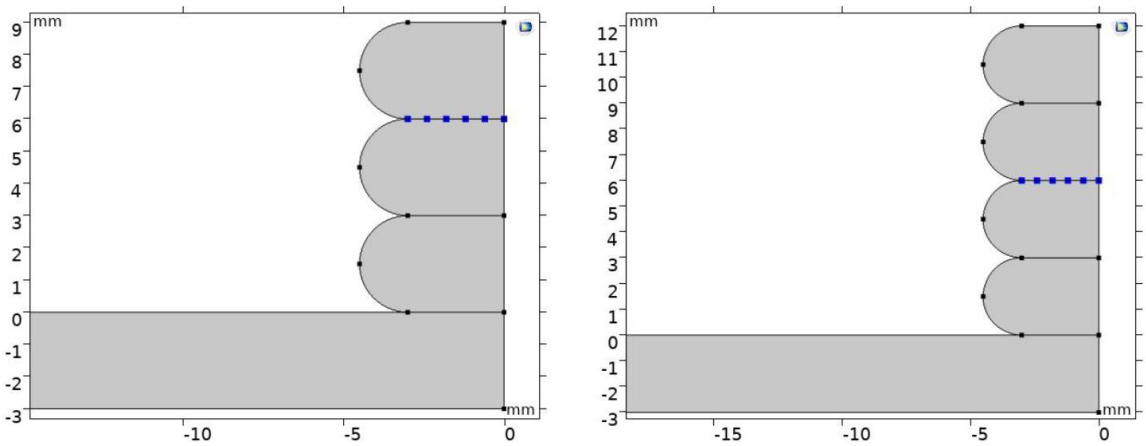

Figure 6.6. Temperature Evaluation Points from COMSOL Bead Stack Geometry

The temperature history between layers two and three in the four bead stack at the six designated points (11 with symmetry) without infrared preheating appear in Figure 6.7.

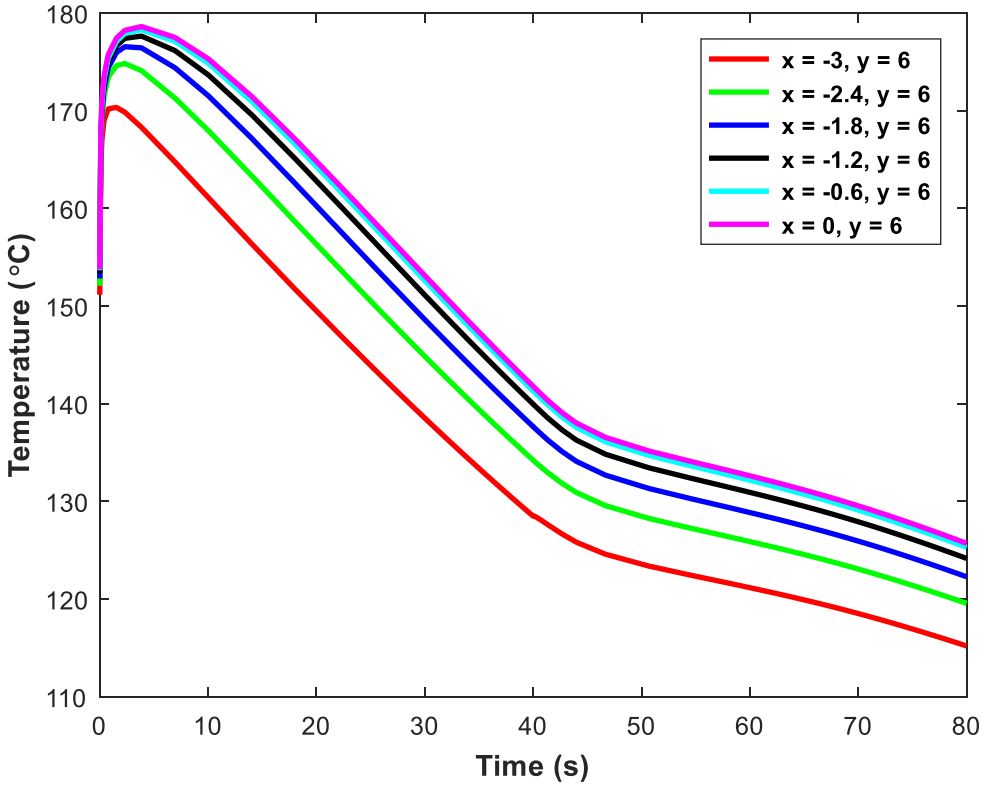

Figure 6.7. Temperature History with Respect to Time Between Layers Two and Three for Non-Infrared Heated Polymer Deposition

The temperature history evaluation for the infrared heated beads is evaluated in the same way as the non-infrared heated model, with six points evaluated between layers two and three. The extra heating step adds another model from which the temperatures are evaluated which is shown in Figure 6.8.

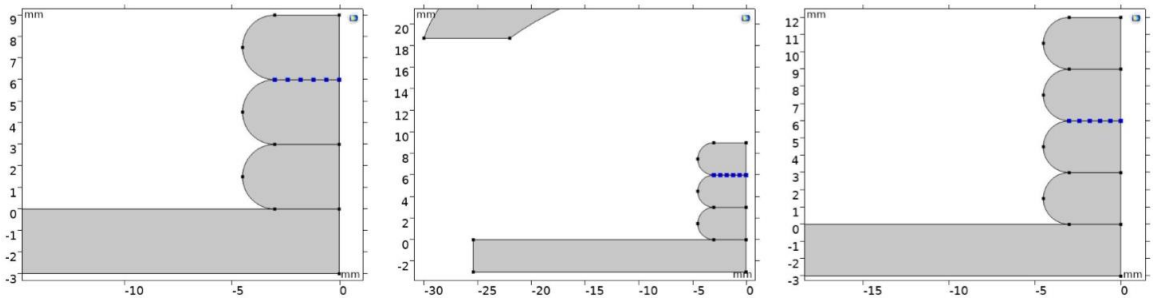

Figure 6.8. Temperature Evaluation Points from COMSOL Bead Stack Geometry Including Infrared Heating Step

The computed temperature history for infrared preheating of the printed beads from the model described in Section 5.2.2 are shown in Figure 6.9. The temperatures in Figure 6.9 are seen to be higher than the temperatures in Figure 6.7 over the same time period which is expected. The bond strength for the infrared preheated specimen is, therefore; expected to be greater than that of the non-infrared preheated model. In Figure 6.9, the effect of the infrared heater is seen from time 35.2 seconds to 40 seconds, where the temperature increases at the exterior surface of the beads (coordinate x = -3, y = 6). The increase in temperature due to the infrared heater is still seen, but to a much smaller degree at x= -2.4, y = 6. The effect of infrared heating decreases towards the center of the bead and becomes negligible along the bead centerline. Note given greater infrared heating times or greater infrared intensity the temperature increase seen at the two outermost points would be realized at points further into the bead thickness.

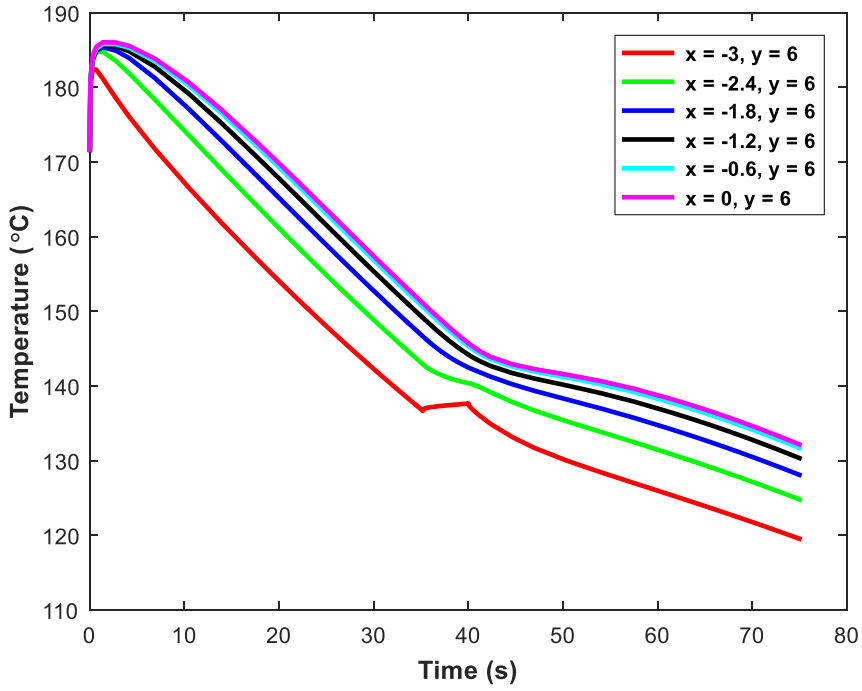

Figure 6.9. Infrared Heated Temperature History with Respect to Time Between Layers Two and Three

The bond strength growth for LAAM interlayer bond lines is calculated using the models of Bastien and Gillespie [41] and Pitchumani and Yang [42] for polymer diffusion and shown in Figure 6.10. In Figure 6.5 three data sets for reptation time, two from literature and one from our rheometer using Lustran 433 ABS, are shown. Bond strength over the interlayer bead width is shown in Figure 6.10 using the reptation data of Coogan [129], Hart [116], and our rheometer data, to represent the upper, lower bounds and an intermediate value possible with the given ABS materials.

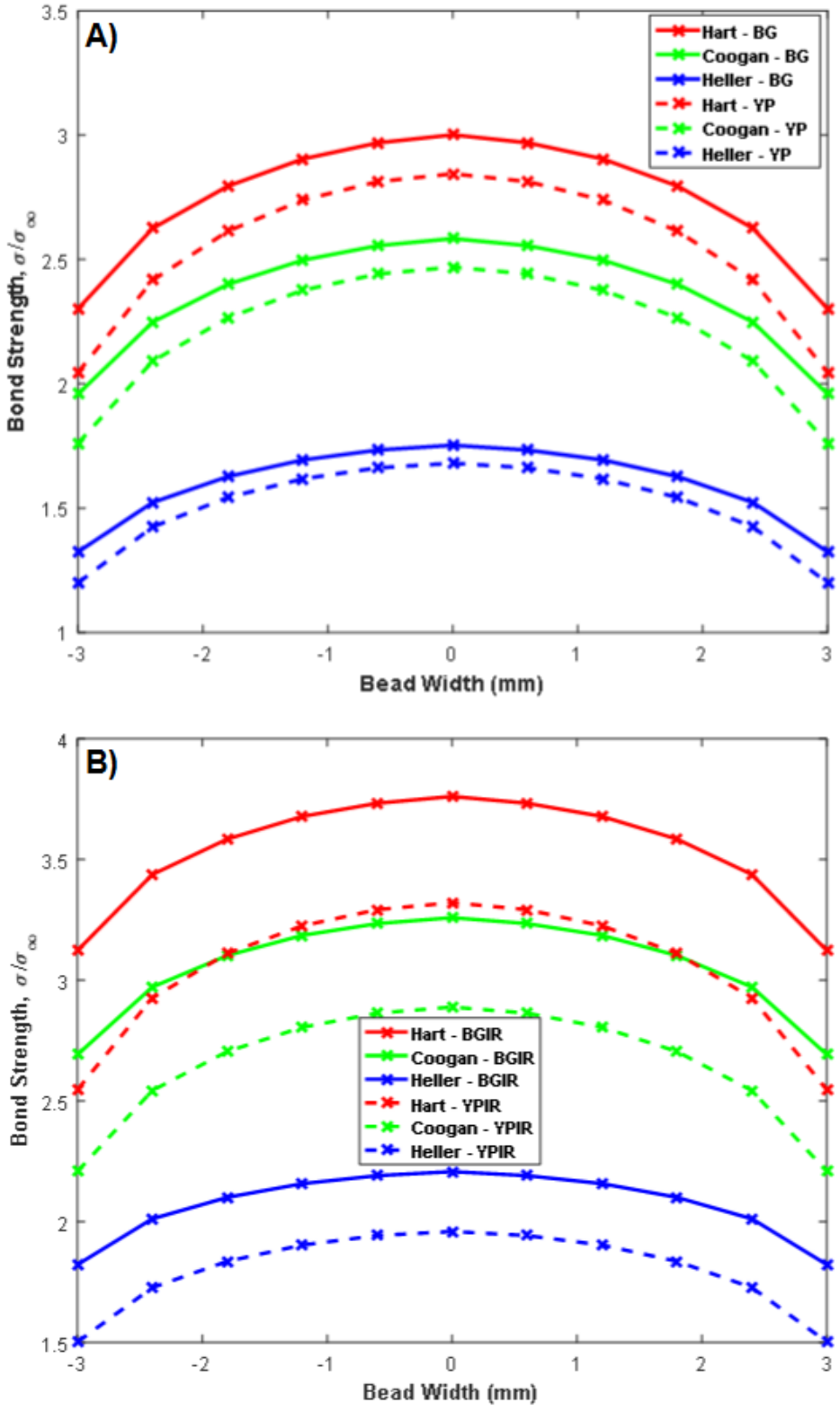

Figure 6.10. Bond Strength Over the Bead Width for Coogan, Hart, and Heller Reptation Time with Bastien and Gillespie and Yang and Pitchumani Healing Models A) without and B) with Infrared Preheating

Figure 6.10 shows all predictions have values greater than 1 for the bond strength between deposited beads. This result would mean that the strength of the interlayer bond is equal to the strength of the base polymer (not greater due to the upper bound which is the strength of the base polymer), therefore; one must conclude that this evaluation is missing a relevant physical phenomenon.

The bond strength growth models used for Figure 6.10 show that all values along the interlayer bond line have values greater than one. There is an inherent understanding to the given models that any value of bonding through polymer chain diffusion will peak at a value of one meaning the bond is as strong as the base material. Values appearing in Figure 6.10 indicate that there is sufficient thermal energy between these layers to allow for full bond strength to be achieved. Unfortunately, but it is well understood that LAAM printed parts are weak in the direction normal to the print plate, rendering these models ineffective.

The models discussed to this point assume that the fiber filled polymers have immediate and perfect intimate contact which is impossible to achieve in bonding processes and is very far from what is achieved with a basic Large Area Additive Manufacturing printer. Intimate contact growth with respect to time must, therefore; be considered to effectively evaluate the realized bond strength between successively deposited layers. The model produced by Butler, et al. [43] allows for the analysis of the growth of intimate contact as well as polymer chain diffusion concurrently. In the model described in Equation 6.9 the wettability of the two bonding surfaces is included in the bond strength growth evaluation and contains a roughness term, R_c, the temperature

dependent polymer viscosity, $\mu(T)$, at time, τ, and the applied pressure at the bond interface.

The roughness parameter given in Equation 6.8 is a function of the initial bead geometry. The roughness constant is calculated as

$$R_C = D_{ico} {C_1}^{1/5} \tag{6.12}$$

where D_{ico}, is the original contact area defined in Equation 6.7, and C_1 is defined as

$$C_1 = 5\left(1 + \frac{w_0}{b_0}\right)\left(\frac{a_0}{b_0}\right)^2 \tag{6.13}$$

The roughness of a surface and specifically the repeated rectangular initial geometry used to calculate it is very difficult to measure, therefore; the roughness parameter is used as an empirical fitting coefficient.

The evaluation of , Ω, is pivotal for the bond strength evaluation. The viscosity and pressure at the bond interface can be evaluated from our temperature dependent Carreau-Yasuda viscosity model given in Equation 4.4 and from the resulting finite element model.

The temperature dependent polymer viscosity for a shear rate of 26 s^{-1} is defined from the glass transition temperature of ABS (105 °C) to 260 °C using the non-isothermal Carreau-Yasuda model presented in Chapter Four and is shown in Figure 6.11. The pressure at the bond interface is defined using the flow model presented in Chapter Four as well, where the pressure between the deposited ABS and the print plate is evaluated in the flow model for the length of the modeled bead. The pressure along this boundary is shown in Figure 6.12.

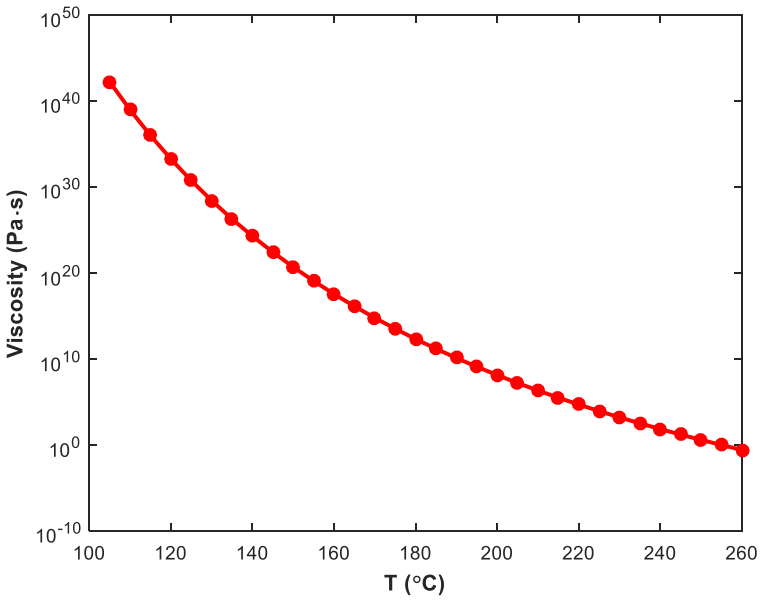

Figure 6.11 Polymer Viscosity with Respect to Temperature Using Carreau-Yasuda at a Shear Rate of 26 s^{-1}

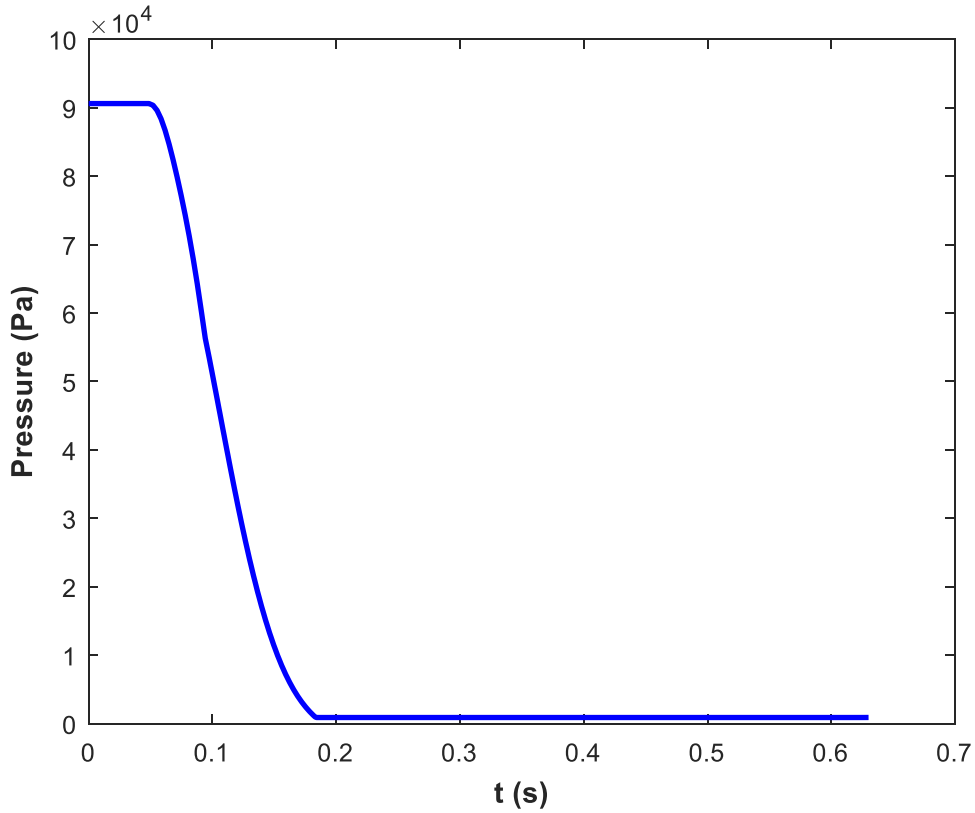

Figure 6.12. Pressure along Interlayer Boundary Between Deposited Bead and Aluminum Print Plate

The temperature histories from Figures 6.7 and 6.9 are used to evaluate the bond strength in conjunction with the coupled bonding method given in Equation 6.9. Figure 6.13 shows the values for the integral representing growth in intimate contact area and bond strength with and without infrared preheating. An initial contact area that undergoes full reptation is set at 0.5, which represents 50% of the initial bond area has intimate contact upon deposition.

The values of bond strength growth created by intimate contact growth are seen to be miniscule. The growth of bond strength through intimate contact is shown to increase by values of 1-45E-7 with the addition of infrared heating, and 1-9E-9 without the addition of infrared heating. This is driven by an, Ω, which far less than one which would present a highly intimate contact driven bonding process, which is expected with the very small pressure application of deposition over a small time period. It is understood, therefore; that the initial contact area upon deposition is the driving force for temperature based bonding in the Large Area Additive Manufacturing process.

The values shown in Figure 6.13 are expected to show larger values with the application of substantial heating and pressure application after deposition. There is an inherent limit to temperature and pressure application as polymer degradation occurs at very high temperatures and excessive deformation of the deposited beads is not desired.

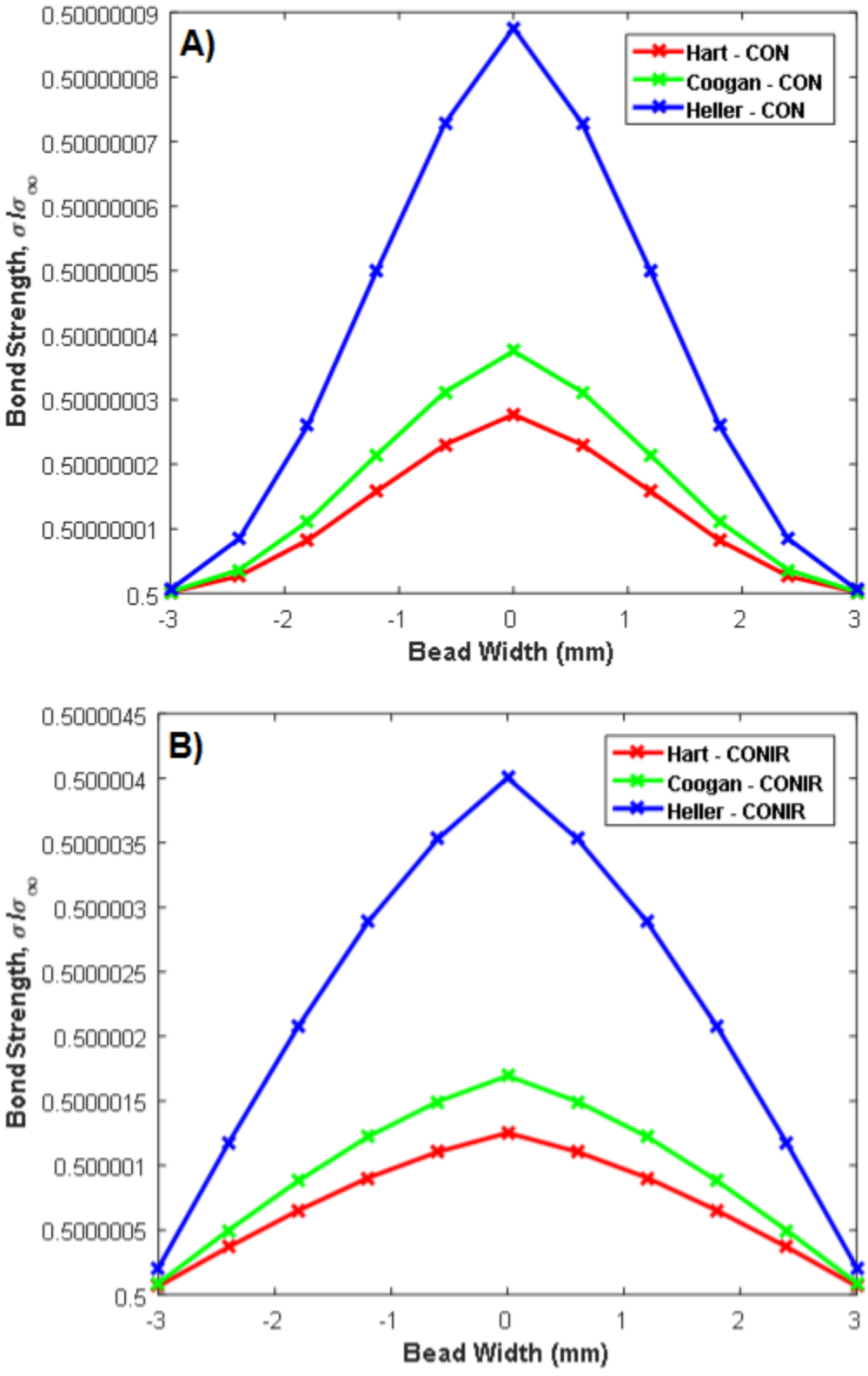

Figure 6.13. Bond Strength Over the Bead Width for Coogan, Hart, and Heller Reptation Time with Coupled Healing Models A) without and B) with Infrared Preheating

6.3.2 Single Lap Shear Tensile Test of Bond Strength

The single lap shear specimens used to demonstrate our bond strength growth presented in the previous section are created using the Large Area Additive Manufacturing printer that was built at Baylor University. A rectangle that takes 40 seconds per layer to deposit is created that is set to be four layers tall. Originally, a two layer rectangle was used, but it was found that breaking occurred in the legs before the bond area due to a very small cross sectional area in each leg of the specimen, therefore; a four bead sample was used to double the cross sectional area of the lap shear joint leg.

Another consideration was the shape of the bonded area that was to be used. Initially a square bond area was used due to being very easy to cut by hand, but concerns about stress concentrations at the corners of the square bond shape led to the use of circular bond areas to provide a more even stress distribution over the bond area. As a check to the stress concentration thought process a tensile test model for the bonded single lap shear joint was run, which is shown in Figure 6.14. As predicted there is a stress concentration seen at the four corners in the square bond shape. Stress concentrations still exist for the circular bond shape, but the concentration is distributed over the majority of the shear face and the magnitude of the stress is lower than in the square bond model. It is worth noting the upper circle and square bond shapes have an equal area of 40 mm^2, and the lower square and circle bond shapes have an area of 17.8 mm^2. Equal bond area allows for accurate decision making with respect to bond shape. Analysis of the plots in Figure 6.14 lead to the choice of a circular bond area for creating test specimens due to a decreased and more evenly distributed stress concentration over the geometry.

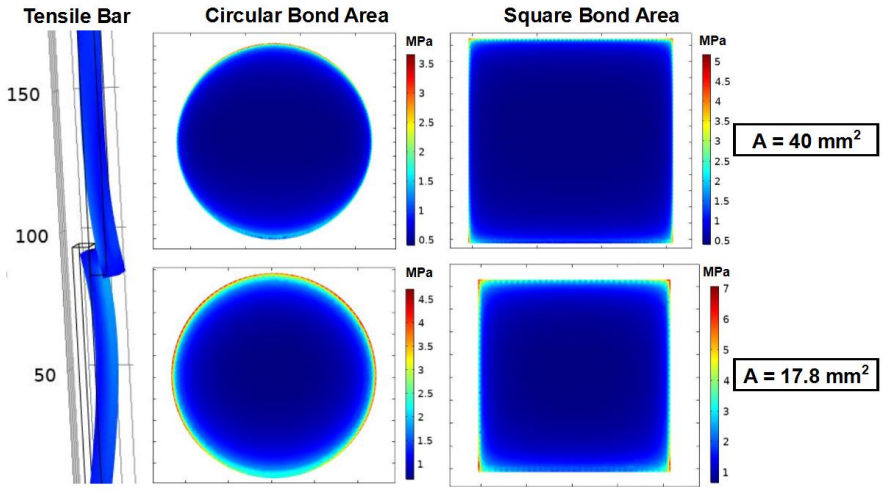

Figure 6.14. Tensile Test and Bond Area Shape Analysis for Stress Concentration, Von-Mises Stress

The creation of the single lap shear tensile specimens is now described in four steps as is shown in Figure 6.15. Two layers of polymer are initially deposited onto the print plate. Between the second and third layers a 0.003" PTFE film with bonding hole with a diameter of 4.763 mm (0.1875 in) is placed on the two previously deposited beads and taped down. The PTFE film is seven inches in length plus the length of the diameter of the bond hole. The hole in the middle of the PTFE film is cut at the diameter which will be the diameter of the bonded area in the lap shear tensile specimen. The third and fourth layers are then printed on top of the PTFE film. After completion of the print process a band saw is used to cut opposing legs off of the sample leaving a lap shear tensile specimen with a spent PTFE film still attached. The PTFE film is then removed and the specimen is marked with information about the specific print process used and the number for that specimen.

Tensile tests are then completed on the given samples using a TestResources (TestResources) machine. The tensile test procedure follows the method provided in

ASTM standard D3163-01. The offset grips are tightened so that the centerline of the bonded area of the single lap shear specimen does not sustain an applied bending moment, one inch of each of the single lap shear legs is contained in the respective upper and lower grips, the crosshead speed during testing is set at 1.3 mm/min (approximately 0.05 in/min), and all results are reported in stress units of MPa. The max load at during testing is compared to the area of the bond left after the PTFE film is removed. The area of the fractured bond surface is measured using a Keyence VR-3000 Microscope, which is shown in Figure 6.16.

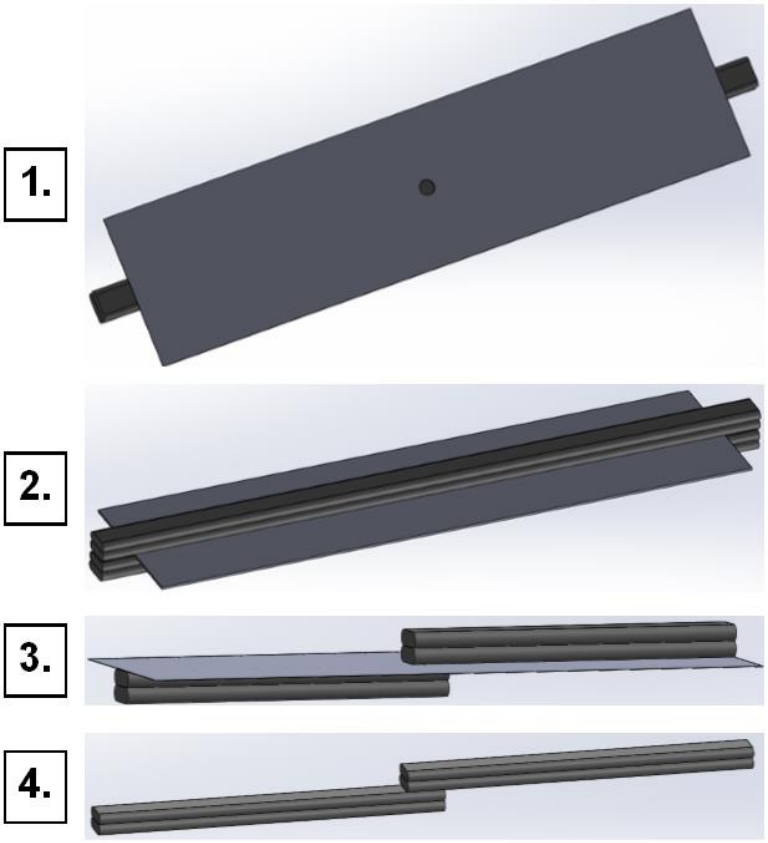

Figure 6.15. Lap Shear Specimen Production Process

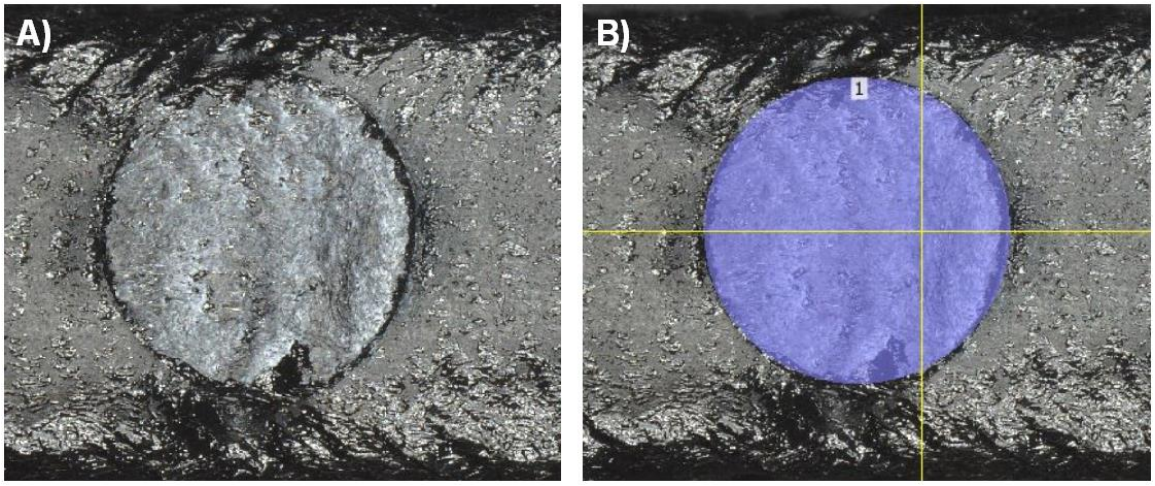

Figure 6.16 Bond Area Calculation using Keyence VR-3000, A) Initial Image, B) Circular Domain Used to Calculate Area

The bond strength is then evaluated using the max load and area of the bond surface. An example of the tensile test results used are shown in Figure 6.17, with maximum applied load shown as an ‘x’ of the same color as the load versus displacement line.

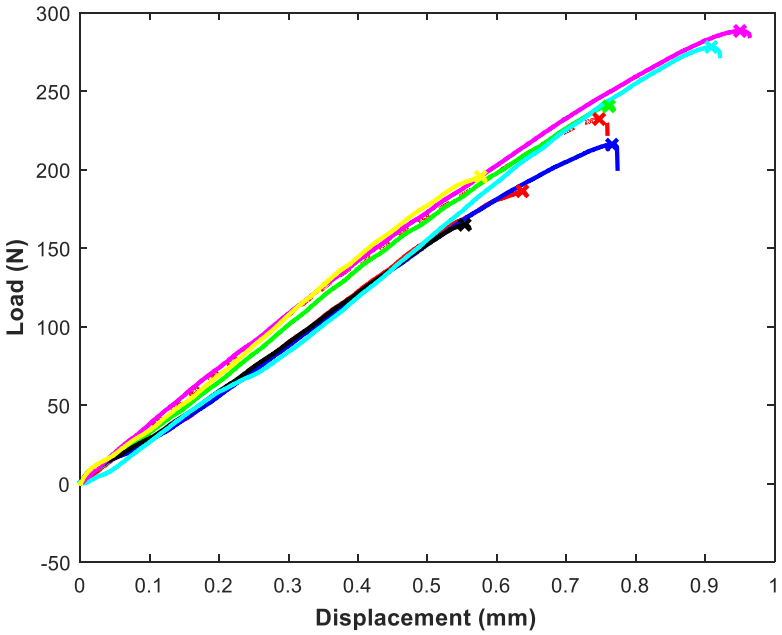

Figure 6.17. Tensile Test Results for Printed Samples with No Additions

The average bond strength for samples tested is shown in Table 6.1. The table includes values for the strength of the bond, σ, the strength of the bond with respect to the strength of the neat ABS polymer, σ/σ_∞, and the percent improvement with respect to printing with no additions. For the basic printing process with no additions the bond strength is 14.88 MPa which is approximately 35.4% of the overall strength of the neat ABS material (42 MPa) [124]. The addition of the smooth roller increases the strength of the bond to nearly half of the overall strength of the ABS material and is an almost 40% improvement in bond strength compared to printing with no additions. The textured roller results very closely mirror the values presented for the smooth roller which is not what was expected when adding this device. The infrared heater showed the greatest improvement over the base bond strength with an increase of 52.3 % over the basic print condition. It is seen for the given PTFE film geometry used here that all additions to the printing process increase the bond strength between successively deposited layers. The bond strength evaluation using the convolution integral approach presented in the previous section uses an initial intimate contact area of 50% or 0.5. This value could be changed to fit the data shown for printing with no additions or infrared heated specimens, but due to the complexity of measuring the initial intimate contact area would require a substantial effort as the roughness of the bead interfaces is not constant and is difficult to measure accurately.

Note that a single bond area is used that is sufficiently small to allow for the stress state at the bond line to be shear stress dominant. It is expected that with larger bond areas the stress state will become more complex with the inclusion of bending and peel stress which has been discussed in literature [131-133]. Also, as was found with initial

testing of the single lap shear specimens, larger bond areas may increase the number of specimens that break in the single lap shear specimen legs. This can be fixed with the addition of more layers to the bead stack (6 or 8 layers), which would result in more layers for each single lap shear specimen legs (3 or 4 layers). The test that was run was introduced as a demonstration of what was found in our presented modeling approach. A more in-depth study of the single lap shear test that was created in this dissertation would benefit the viability of the testing method as a metric for bond strength improvement in Large Area Additive Manufacturing.

Table 6.1. Print Process Additions Bond Strength Calculation

Process	σ (MPa)	σ/σ_∞	% Increase
No Additions	14.88	0.354	0
Smooth Roller	20.80	0.495	39.8
Smooth and Textured Roller	20.78	0.495	39.7
Infrared Heater 420 °C	22.66	0.540	52.3

6.4 Conclusions from Heat Transfer Model and Interlayer Bonding Analysis

In the presented study the bond strength between successively printed layers is modeled using the results from the heat transfer models with and without infrared preheating from Chapter Five. The bond strength predictions using the polymer chain diffusion models of Bastien and Gillespie and Yang and Pitchumani show bond strength values that are much greater than one, where a value of one represent bond strength equal to the strength of the base material. This means that the temperature history that occurs between layers in Large Area Additive Manufacturing are sufficient to promote bond strength that is much greater than what is seen in printed samples. The other major mechanism in polymer-polymer bonding is wetting or growth of intimate contact

between two layers of a polymer material. The coupled polymer diffusion and intimate contact model was used to analyze growth of bond strength with respect to time between successively deposited beads. It was seen that due to small amounts of pressure application over a very short period of time and high viscosity values of the polymer at cool temperatures cause infinitesimal amounts of bond strength growth after deposition. This implies that the bond strength is almost completely dependent on the initial area of the polymer that is in intimate contact after deposition.

Single lap shear tensile specimens were printed using the large area additive manufacturing printer built at Baylor University. The strength of the bond between successively printed layers was evaluated by placing a PTFE film with a small hole cut in the center to allow for a controlled bond size and shape between layers two and three in the printed bead stack. The single lap shear specimens were tested using a TestResources tensile tester which has grips that can handle geometries with an offset.

The bond strength was evaluated as the maximum load with respect to the area of the bond fracture surface. Using a bond hole with a diameter of 0.1875 in the results showed the expected theoretical trends of bond strength growth with additions to the print process.

Improvements to the bond strength modeling and the creation of the single lap shear process presented in this chapter present a basis for understanding polymer bonding and bond strength testing in Large Area Additive Manufacturing which will help to improve the industrial viability of this manufacturing process.

CHAPTER SEVEN

Conclusions and Future Work

7.1 Conclusions

Large Area Additive Manufacturing is a popular method for the fast production of parts such as tooling, which has seen vast improvements in the past decade. The improvements made to the Large Area Additive Manufacturing process have greatly increased the industrial viability of this technology, but there are still issues that present substantial problems to the full acceptance of this technology as a manufacturing technique. Poor interlayer bonding and voids that occur during the printing process reduce the overall strength of the part which needs to be improved.

The work presented in this dissertation sought to improve the modeling of the deposition process, to provide a modeling technique for bond strength evaluation through heat transfer analysis of the basic printing process and with the addition of infrared heating, and created a mechanical testing technique to evaluate the bond strength between successively printed layers which used a single lap shear tensile specimen with a defined bond area. The results from the given studies and the conclusions for each are now discussed in further detail.

In Chapter Three a Newtonian fluid flow model was created for the deposition flow exiting a Large Area Additive Manufacturing extruder nozzle onto a print plate at different deposition heights. The turning flow that occurs in this process was evaluated for the first time in this work, where a minimization of the free surface technique was

applied similar to the technique used by Heller, et al. [6]. Deposition at different nozzle heights is common in Large Area Additive Manufacturing and is dependent on what the operator is trying to produce during deposition. Three nozzle heights were considered in this study which are level flow (the nozzle is at the height of the deposited bead), bull nose flow (the nozzle is below the height of the deposited bead), and falling flow (the nozzle is above the height of the deposited bead). The fiber orientation was evaluated for the three deposition heights that were modeled to determine the change in mechanical and thermomechanical properties of the deposited beads dependent on nozzle deposition height. The properties were found to change very little between the deposition heights, but the fiber orientation distribution was found to change substantially through the bead thickness causing anisotropy in the deposited bead. The anisotropy evaluated in this study is considered to be a part of the warping and delamination issues that occur in Large Area Additive Manufacturing printed parts.

In Chapter Four the deposition model was improved by adding a non-isothermal Carreau-Yasuda polymer flow model to the minimization process. It is known that polymers are shear thinning fluids that have temperature dependent viscosities, therefore; the improvement from modeling a Newtonian fluid was needed. Three new models were run only analyzing the level flow geometry discussed in Chapter Three. The flow models include an isothermal Carreau-Yasuda model, non-isothermal Carreau-Yasuda model depositing onto an aluminum print plate, and a non-isothermal Carreau-Yasuda model depositing on a previously printed ABS bead. These models were compared with the level flow Newtonian model from Chapter Three. The isothermal Carreau-Yasuda model showed the greatest increase in swell with respect to the Newtonian flow model, whereas

both of the non-isothermal models were seen to be similar to the Newtonian flow model. The decrease in swell with respect to the isothermal model seen for the non-isothermal models is expected to be due to the temperature dependency which effects the polymer viscosity.

Fiber orientation was again calculated for all of the flow models that were analyzed, but some major changes were made to the properties used in the orientation flow modeling to more accurately describe the carbon fiber filled material we began using in the Large Area Additive Manufacturing printer built at Baylor University. Also, the anisotropic thermal conductivity for misaligned short carbon fibers was derived and used for the first time in the thermomechanical property evaluation of the deposited bead. The changes to the properties in the fiber orientation models returned different values than what was calculated in Chapter Three. This is due to a much larger fiber aspect ratio which was calculated by Russel, et al. [125], the longitudinal modulus and thermal conductivities were seen to be much higher, and the longitudinal coefficient of thermal expansion was seen to decrease substantially with the greater fiber aspect ratio. The properties evaluated with the improved non-isothermal Carreau-Yasuda were then used in Chapter Five.

In Chapter Five, transient heat transfer models were created to evaluate temperature history during the deposition process for four successively deposited beads with and without infrared preheating. Infrared preheating of previously deposited beads has been done in experimental studies, but a model to account for the increased temperatures due to infrared heating was created for the first time. The temperature histories for the four bead stacks were evaluated using the bead geometries measured

using the Baylor LAAM printer, and a somewhat complex system was created for accurate temperatures to be computed for each addition of a bead to the stack.

In Chapter Six the temperature histories from the transient heat transfer models from Chapter Five were used to evaluate the bond strength and dominant bonding mechanism that occurs in LAAM printing. The polymer diffusion models which assume complete intimate contact of the bonding area returned values greater than one for both the infrared preheated and basic printing processes, which would mean that the bond strength is greater than the material strength of the bonding polymers. This is impossible and a maximum strength limit is held at a value of one, but this result means that there is enough thermal energy held between successively printed beads to promote complete bonding. It is known that the bond strength between successively printed layers is far lower than the strength of the polymer material, therefore; another bonding mechanism (intimate contact growth) is designated as the reason behind the low bond strength. A coupled polymer diffusion and intimate contact model is then evaluated using the temperature histories from Chapter Five. This model shows that growth of bond strength through the growth of intimate contact after deposition is infinitesimal due to low pressure application and substantial viscosity of the polymer. This means that the initial area that comes in intimate contact during the deposition process is essentially the only area of intimate contact that becomes fully bonded which is far less than the entire bond area.

The addition of a smooth roller, textured roller, and infrared heater to the deposition printing process is then applied to improve the bonding between successively printed layers. The smooth roller applies pressure to the hot polymers in the bead stack

and improves the bond strength over the basic printing process by 39.8%. The textured roller which was expected to increase the strength between layers by creating a mechanical interlock was found to not cause the expected improvement as it was slightly weaker than the results found for the smooth roller with a strength increase of 39.7% compared to the basic printing process. The infrared heater provided the greatest improvement to bond strength with an increase in strength of 52.3% over the basic printing process.

The studies completed in this dissertation allow for a better understanding of what occurs during the deposition printing process. Improved deposition flow models and fiber orientation models provide more accurate results for expected properties in LAAM printed beads. Improved heat transfer models which use the anisotropic properties evaluated using the deposition models, and include the effects of an infrared pre-deposition heater provide a sound basis for the evaluation of interlayer bond strength in LAAM printed parts. The bonding analysis shows that the initial intimate contact area is the driving force behind bond strength between deposited layers, which are insufficient for the basic LAAM printing process. Additions to the printing process showed the expected improvements except for the textured roller that was introduced. The work presented is an improvement to the knowledge of the LAAM printing process, but more work is needed to increase the industrial viability of LAAM as a manufacturing technique.

7.2 Future Work

The deposition model presented in this dissertation is substantially improved with respect to previous studies, but there are some improvements that could still be made.

The most helpful improvement to the deposition model would be the evaluation of the gradients for the minimization process. This is a complex task that would greatly improve the speed of a very slow minimization process. Also, the non-isothermal Carreau-Yasuda viscosity model was evaluated with properties found in literature, and could be improved by fitting rheological data for our specific fiber filled ABS material to the Carreau-Yasuda viscosity model as well as evaluation of the material specific activation energy for the non-isothermal portion of the model.

The heat transfer models presented in this work are an improvement to what is currently presented in literature, but there is some difference between what is modeled and what is seen when imaging the print process with the FLIR E95 camera. The heat transfer coefficient used in the model could be more accurately evaluated which would improve the overall heat transfer model. Also, the ambient temperature around the beads during deposition should be evaluated in the Baylor LAAM printer environment. In this work, room temperature was used, but in the area immediately around the deposited beads the temperature is expected to be greater than room temperature.

The analytical bond strength analysis that was completed in this work could be improved by an in depth study of the roughness parameter and initial intimate contact area evaluation which would improve the accuracy of the model. The single lap shear bond strength test method used in this work used a singular bonding area as a demonstration of the test method, but improvements to the test method and production of the single lap shear test specimens would benefit from a more in depth analysis.

The improvement of interlayer bonding through more accurate modeling techniques and process improvements is pivotal to increasing the industrial viability of

Large Area Additive Manufacturing printing as a common manufacturing technique. Several ideas for improvement on the methods presented in this dissertation have been presented and should be accomplished to further improve the Large Area Additive Manufacturing Process.

BIBLIOGRAPHY

[1] Nikzad, M., Masood, S.H., Sbarski, I., Thermo-mechanical properties of a highly filled polymeric composites for Fused Deposition Modeling, Materials & Design, 32(6), pp. 3448-3456, June 2011

[2] Mulholland, T., Goris, S., Boxleitner, J., Osswald, T.A., Rudolph, N., Process-Induced Fiber Orinentation in Fused Filament Fabrication, Journal of Composites Science, 45(2), pp. 1-14, August 2018

[3] Tekinalp, H.L., Kunc, V., Velez-Garcia, G.M., Duty, C.E., Love, L.J., Naskar, A.K., Blue, C.A., and Ozcan, S., Highly Oriented Carbon Fiber-Polymer Composites via Additive Manufacturing, Composites Science and Technology, 105, pp. 144-150, 2014.

[4] Jiang, D., Smith, D.E., "Mechanical Behavior of Carbon Fiber Composites Produced with Fused Filament Fabrication," Solid Freeform Fabrication Symposium Proceedings, pp. 884-898, August 2016

[5] Nixon, J., Dryer, B., Lempert, I., and Bigio, I., Three Parameter Analysis of Fiber Orientation in Fused Deposition Modeling Geometries, Proceedings of PPS-30, (2014)

[6] Heller, B.P., Smith, D.E, Jack, D.A., Effects of extrudate swell and nozzle geometry on fiber orientation in Fused Filament Fabrication nozzle flow, Additive Manufacturing, 12(B), pp. 252-264, October 2016

[7] Heller, B.P., Smith, D.E., Jack, D.A., Planar deposition flow modeling of fiber filled composites in large area additive manufacturing, Additive Manufacturing, 25, pp. 227-238, January 2019

[8] Russell, T., Heller, B., Jack, D.A., Smith, D.E., Prediction of the Fiber Orientation State and the Resulting Structural and Thermal Properties of Fiber Reinforced Additive Manufactured Composites Fabricated Using the Big Area Additive Manufacturing Process, Journal of Composites Science, 26(2), pp. 1-18, April 2018

[9] Wang, Z., Smith, D.E., Rheology Effects on Predicted Fiber Orientation and Elastic Properties in Large Scale Polymer Composite Additive Manufacturing, Journal of Composites Science, 10(2), pp. 1-18, February 2018

[10] Duty, C.E., Kunc, V., Compton, B., Post, B., Erdman, D., Smith, R., Lind, R. Lloyd, P., Love, L., Structure and mechanical behavior of Big Area Additive Manufacturing (BAAM) materials, Rapid Prototyping Journal, 23(1), pp.181-189, 2017.

[11] Love, L.J., Kunc, V., Rios, O., Duty, C.E., Elliot, A.M., Post, B.K., Smith, R.J., Blue, C.A., The importance of carbon fiber to polymer additive manufacturing, Journal of Materials Research, 29(17), pp. 1893-1898, June 2014

[12] Advani, S.G., Tucker, C.L., The use of tensors to describe and predict fiber orientation in short fiber composites, Journal of Rheology, 31, pp. 751-784, 1987

[13] Jack, D.A., Smith, D.E., Elastic Properties of Short-fiber Polymer Composites, Derivation and Demonstration of Analytical Forms for Expectation and Variance from Orientation Tensors, Journal of Composite Materials, 42, pp. 277-308, 2008.

[14] Cintra, J.S., Tucker, C.L. III, Orthotropic closure approximations for flow-induced fiber orientation, Journal of Rheology, 39(6), pp. 1095-1122, 1995

[15] VerWeyst, B.E., Tucker III, C.L., Foss, P.H., O'Gara, J.F., Fiber Orientation in 3-D Injection Molded Features: Prediction and Experiment, International Polymer Processing, 14, pp. 409-420, 1999.

[16] Folgar, F., Tucker, C.L. III, Orientation behavior of fibers in concentrated suspensions, Journal of Reinforced Plastic Composites, 3(2), pp. 98-119, 1984

[17] Wang, J., O'Gara, J.F., Tucker III, C.L., An Objective Model for Slow Orientation Kinetics in Concentrated Fiber Suspensions: Theory and Rheological Evidence, Journal of Rheology, 52, pp. 1179-1200, 2008

[18] Bellini, A., 2003, "Fused Deposition of ceramics: a comprehensive experimental, analytical, and computational study of material behavior, fabrication process and equipment design," Ph.D. thesis, Drexel University, Philadelphia, PA

[19] George, C., 2017, "Additive Manufacturing Extruder Heads," http://strangpresse.com/strangpresse-extruders/

[20] Kishore, V., Ajinjeru, C., Nycz, A., Post, B., Lindahl, J., Kunc, V., Duty, C., Infrared preheating to improve interlayer strength of big area additive manufacturing (BAAM) components, Additive Manufacturing, 14, pp. 7-12, 2017

[21] Blok, L.G., Longana, M.L., Yu, H., Woods, B.K.S., An investigation into 3D printing of fibre reinforced thermoplastic composites, Additive Manufacturing, 22, pp. 176-186, 2018

[22] Pokluda, O., Bellehumeur, C., Vlachopoulos, J., Modification of Frenkel's model for sintering, American Journal of Chemical Engineering, 43(12), pp. 3253-3256, December 1997

[23] Bellehumeur, C., Li, L., Sun, Q., Gu, P., Modeling of Bond Formation Between Polymer Filaments in the Fused Deposition Modeling Process, Journal of Manufacturing Processes, 6(2), pp. 170-178, 2004

[24] Gurrala, P.K., Regalla, S.P., Part strength evolution with bonding between filaments in fused deposition modelling, Virtual and Physical Prototyping, 9(3), pp. 141-149, April 2014

[25] de Gennes, P.G., Reptation of a Polymer Chain in the Presence of Fixed Obstacles, The Journal of Chemical Physics, 55, pp. 572-579, 1971

[26] Wool, R.P., Time-Dependence of Crack Healing, Journal of Polymer Science, Part C, Polymer Letters, 20(1), pp. 7-16, January 1982

[27] Wool, R.P., Welding of Polymer Interfaces, Polymer Engineering and Science, 29(19), pp. 1340-1367, October 1989

[28] Kim, S.G., Suh, N.P., Performance prediction of weldline structure in amorphous polymers, Polymer Engineering and Science, 26(17), pp. 1200-1207, September 1986

[29] Thomas, J.P., Rodriguez, J.F., 2000, "Modeling the Fracture Strength Between Fused Deposition Extruded Roads," Solid Freeform Fabrication Symposium Proceedings, Austin, TX

[30] Li, L., Sun, Q., Bellehumeur, C., Gu, P., 2002, "Investigation of Bond Formation in FDM Process," Solid Freeform Fabrication Symposium Proceedings, Austin, TX

[31] Compton, B.G., Post, B.K., Duty, C.E., Love, L., Kunc, V., Thermal analysis of additive manufacturing of large-scale thermoplastic polymer composites, Additive Manufacturing, 17, pp. 77-86, July 2017

[32] Ravi, A., Deshpande, A., Hsu, K., An in-process laser localized pre-deposition heating approach to inter-layer bond strengthening in extrusion based polymer additive manufacturing, Journal of Manufacturing Processes, 24(1), pp. 179-185, October 2016

[33] Kusel, S.D., 2017, “A Study of Heating and Degradation of Acrylonitrile-Butadine-Styrene/Polycarbonate Polymer Due to Ultraviolet Lasers Illumination during Localized Pre-Deposition Heating for Fused Filament Fabrication 3D Printing,” M.S. thesis, Arizona State University, Tempe, AZ

[34] Partain, S., 2007, “Fused Deposition Modeling with Localized Pre-Deposition Heating Using Forced Air,” M.S. thesis, Montana State University, Bozeman, MT

[35] Lee, M.J., Lim, J.M., Lee, B.C., Finite Element Analysis of an Adhesive Joint Using the Cohesive Zone Model and Surface Pattern Design of Bonding Surfaces, The Journal of Adhesion, 89, pp, 205-224, 2013

[36] Pocius, A.V., 2012, Adhesion and Adhesives: Science and Techonology: An Introduction, Carl Hanser Verlag GmbH & Company KG, Munchen, Deutschland

[37] Prolongo, S.G. and Urena, A.,Effect of surface pre-treatment on the adhesive strength of epoxy aluminum joints, International Journal of Adhesion and Adhesives, 29(1), pp. 23-31, January 2009

[38] Shahid, M., Hashim, S.A., Effect of surface roughness on the strength of cleavage joints, International Journal of Adhesion and Adhesives, 22(3), pp. 235-244, 2002

[39] Kim, W.S, Yun, I.H., Lee, J.J., Jung, H.T., Evaluation of mechanical interlock effect on adhesion strength of polymer-metal interfaces using micro-patterned surface topography, International Journal of Adhesion and Adhesives, 30(6), pp.408-417, 2010

[40] Reis, P.N.B., Ferreira, J.A.M., Antunes, F., Effect of adherend’s rigidity on the shear strength of single lap adhesive joints, International Journal of Adhesion and Adhesives, 31(4), pp. 193-201, June 2011

[41] Bastien, L.J., Gillespie Jr., J.W., A non-isothermal healing model for strength and toughness of fusion bonded joints of amorphous thermoplastics, Polymer Engineering and Science, 31(24), pp. 1720-1730, December 1991

[42] Yang, F., Pitchumani, R., Healing of Thermoplastic Polymers at an Interface under Nonisothermal Conditions, Macromolecules, 35, pp. 3213-3224, 2002

[43] Butler, C.A., McCullough, R.L., Pitchumani, R., Gillespie, J.W., An Analysis of Mechanisms Governing Fusion Bonding of Thermoplastic Composites, Journal of Thermoplastic Composite Materials, 11, pp. 338-363, July 1998

[44] Tanner, R.I, A Theory of Die Swell, Journal of Polymer Science: Part A-2, 8, pp. 2067-2078, 1970

[45] Tanner, R.I, A Theory of Die Swell Revisited, Journal of Non-Newtonian Fluid Mechanics, 129, pp. 85-87, 2005

[46] Athanasopulos, I., Makrakis, G., and Rodrigues, J.F., 1999, Free boundary problems: theory and applications, 1st ed., Chapman & Hall/CRC, Boca Raton, FL

[47] Georgiou, G.C., The Compressible Newtonian Extrudate Swell Problem, International Journal For Numerical Methods in Fluids, 20, pp. 255-261, 1995.

[48] Georgiou, G.C., Boudouvis, A.G., Converged Solutions of the Newtonian Extrudate-Swell Problem, International Journal For Numerical Methods in Fluids, 29, pp. 363-371, 1999.

[49] Elwood, K.R.J., Papanastasiou, T.C., and Wilkes, J.O., Three-Dimensional Streamlined Finite Elements: Design of Extrusion Dies, International Journal for Numerical Methods in Fluids, 14, pp. 13-24, 1992.

[50] Karagiannis, A., Hrymak, A.N., Vlachopoulos, J., Three-dimensional extrudate swell of creeping Newtonian jets, American Journal of Chemical Engineering, 34(12), pp. 2088-2094, December 1988

[51] Michaeli, W., 1984, Extrusion Dies: Design and Engineering Computations, 1st ed., Hanser, Cincinnati, OH

[52] Mitsoulis, E., Georgiou, G.C., Kountouriotis, Z., A study of various factors affecting Newtonian extrudate swell, Computers and Fluids, 57, pp. 195-207, March 2012

[53] Mitsoulis, E., Hatzikiriakos, S.G., Annular extrudate swell of fluoropolymer melt, International Polymer Processing, 27(5), pp. 535-546, 2012

[54] Kanvisi, M., Motahari, S., Kaffashi, B., Numerical investigation and experimental observation of extrudate swell for viscoelastic polymer melts, International Polymer Processing, 29(2), pp. 227-232, 2014

[55] Nixon, J., Dryer, D., Chiu, D., Lempert, I., Bigio, D.I., 2014, Three Parameter Analysis of Fiber Orientation in Fused Deposition Modeling Geometries, ANTEC Proceedings, Las Vegas, NV

[56] Lewicki, J.P., Rodriguez, J.N., Zhu, C., Worsley, M.A., Wu, A.S., Kanarska, Y., Horn, J.D., Duoss, E.B., Ortega, J.M., Elmer,W., Hensleigh, R., Fellini, R.A., King, M.J., 3D-Printing of Meso-structurally Ordered Carbon Fiber/Polymer Composites with Unprecedented Orthotropic Physical Properties, Scientific Reports, 7, pp. 1-14, March 2017.

[57] Osswald, T.A., Puentes, J., Kattinger, J., Fused filament fabrication melting model, Additive Manufacturing, 22, pp. 51-59, April 2018

[58] Ramanath, H.S., Chua, C.K., Leong, K.F., Shah, K.D., Melt flow behavior of poly-ε-caprolactone in fused deposition modeling, Journal of Materials Science Materials in Medicine, 19(7), pp. 2541-2550, August 2008

[59] Gilmer, E.L., Miller, D., Chatham, C.A., Zawaski, C., Fallon, J.J., Pekkanen, A., Long, T.E., Williams, C.B., Bortner, M.J., Model analysis of feedstock behavior in fused filament fabrication: Enabling rapid materials screening, Polymer, 152, pp. 51-61, September 2018

[60] Wang, Z., Smith, D.E., "Screw Swirling Effects on Fiber Orientation Distribution In Large-Scale Polymer Composite Additive Manufacturing," Solid Freeform Fabrication Symposium Proceedings, pp. 1832-1846, August 2018

[61] Einstein, A. Eine neue Bestimmung der Molekuldimensionen, Annalen der Physik, 19, pp. 289-306,1896

[62] Jeffery, G.B., The Motion of Ellipsoidal Particles Immersed in a Viscous Fluid, International Journal For Numerical Methods in Fluids, 29, pp. 363-371, 1999

[63] Zhang, D., 2013, "Flow-Induced Micro- and Nano-Fiber Suspensions, Short-Fiber Reinforced Composite Materials Processing," Ph.D. Thesis, University of Missouri, Columbia, MO

[64] Montgomery-Smith, S., Jack, D.A., Smith, D.E., The fast exact closure for Jeffery's equation with diffusion, Journal of Non-Newtonian Fluid Mechanics, 166(7-8), pp.343-353, 2011

[65] Bay, R.S., 1991, "Fiber Orientation in Injection Molded Composites: A Comparison of Theory and Experiment," Ph.D. Thesis, University of Illinois at Urbana-Champaign, Champaign, IL

[66] Phelps, J.H., Tucker III, C.L., An anisotropic rotary diffusion model for fiber orientation in short- and long fiber thermoplastics. Journal of Non-Newtonian Fluid Mechanics, 156, pp. 165–176, 2009

[67] Hand, G.L., Theory of Anisotropic Fluids, Journal of Fluid Mechanics, 13, pp. 33-46, 1962

[68] Lipscomb, G.G., Denn, M.M., Hur, D.U., and Boger, D., The Flow of Fiber Suspensions in Complex Geometries, Journal of Non-Newtonian Fluid Mechanics, 26, pp. 297-325, 1988

[69] Cintra, J.S., Tucker III, C.L., Orthotropic closure approximations for flow-induced fiber orientation, Journal of Rheology, 39(6), pp. 1095-1122, 1995

[70] Wetzel, E.D., Tucker III, C.L., Area tensors for modeling microstructure during laminar liquid-liquid mixing, International Journal of Multiphase Flow, 25(1), pp. 35-61, February 1999

[71] Verleye, V., Dupret, F., 1993, "Prediction of Fiber Orientation in Complex Injection Molded Parts, Symposium; Winter Annual Meeting, Developments in Non-Newtonian Flows, 175, pp. 139–163, New Orleans, LA

[72] Chung, D.H., and Kwon, T.H., Invariant-Based Optimal Fitting Closure Approximation for the Numerical Prediction of Flow-Induced Fiber Orientation, Journal of Rheology, 46, pp.169–194, 2002

[73] Liang, E., Tucker III, C.L., Stiffness predictions from unidirectional short-fiber composites: review and evaluation, Composites Science Technology, 59(5), pp. 655-671, 1999

[74] Hill, R., Elastic properties of reinforced solids: Some theoretical principles, Journal of the Mechanics and Physics of Solids, 11(5), pp. 357-372, September 1963

[75] Eshelby, J.D., The determination of the elastic field of an ellipsoidal inclusion and related problems, Proceedings of the Royal Society A, 241, pp. 376-396, 1957

[76] Mori, T., Tanaka, K., Average stress in matrix and average elastic energy of materials with misfitting inclusions, Acta Metallurgica, 21, pp. 571-574, 1973

[77] Tandon, G.P., Weng, G.J., The effect of aspect ratio of inclusions on the elastic properties of unidirectionally aligned composites, Polymer Composites, 5(4), pp. 327-333, 1984

[78] Zhang, C., 2011, "Modeling of Flexible Fiber Motion and Prediction of Material Properties," M.S. Thesis, Baylor University, Waco, TX

[79] Halpin, J.C., Stiffness and Expansion Estimates for Oriented Short Fiber Composites, Journal of Composite Materials, 3, pp. 732-734, 1969

[80] Camacho, C.W., Tucker III, C.L., Yalvac, S., McGee, R.L., Stiffness and Thermal Expansion Predictions for Hybrid Short Fiber Composites, Polymer Composites, 11(4), pp. 229-239, 1990

[81] Schapery, R.A., Thermal Expansion Coefficients of Composite Materials Based on Energy Principles, Journal of Composite Materials, 3(4), pp. 732-734, 1969

[82] Stair, S., Jack, D.A., Comparison of Experimental and Modeling Results for Cure Induced Curvature of a Carbon Fiber Laminate, Polymer Composites, 38(11), pp. 2488-2500, December 2015

[83] Fu, S.Y., Lauke, B., Mai, Y.W., 2009, "Science and Engineering of Short Fibre Reinforced Polymer Composites," 1st ed., CRC Press, Boca Raton, LA

[84] Cox, H.L., The elasticity and strength of paper and other fibrous materials, British Journal of Applied Physics, 3(3), pp. 72-79, 1952

[85] Springer, G.S., Tsai, S.W., Thermal Conductivities of Unidirectional Materials, Journal of Composite Materials, 1, pp. 166-173, 1967

[86] Thornburg, J.D., Pears, C.D., 1965, "Prediction of the Thermal Conductivity of Filled and Reinforced Plastics," ASME-Paper, 65-WA/HT-4, New York, NY

[87] Carslaw, H.S., Jaeger, J.C., 1986, "Conduction of Heat in Solids," 2nd ed., Oxford University Press, Oxford, United Kingdom

[88] Hasselman, D.P.H., Bhatt, H., Donaldson, K.Y., Thomas, Jr., J.R., Effect of Fiber Orientation and Sample Geometry on the Effective Thermal Conductivity of a Uniaxial Carbon Fiber-Reinforced Glass Matrix Composite, Journal of Composite Materials, 26(15), pp. 2278-2288, 1992

[89] Nye, J.F., 1957, "Physical Properties of Crystals," 1st ed., Oxford University Press, Oxford, United Kingdom

[90] Hasselman, D.P.H., Donaldson, K.Y., Thomas, Jr., J.R., Effective Thermal Conductivity of Uniaxial Composite with Cylindrically Orthotropic Carbon Fibers and Interfacial Thermal Barrier, Journal of Composite Materials, 27(6), pp. 637-644, 1993

[91] Choy, C.L., Leung, W.P., Kwok, K.W., Elastic moduli and thermal conductivity of injection-molded short-fiber-reinforced thermoplastics, Polymer Composites, 13(2), pp. 69-80, 1992

[92] Nielsen, L.E., Thermal Conductivity of particulate-filled polymers, Journal of Applied Polymer Science, 17(12), pp. 3819-3820, 1973

[93] Curtis, J.W., The effect of pre-orientation on the fracture properties of glassy polymers, Journal of Physics D: Applied Physics, 3(10), pp. 1413-1422, 1970

[94] Griffith, A.A., The Phenomena of Rupture and Flow in Solids, Philosophical Transactions of the Royal Society of London, Series A, Containing Papers of a Mathematical or Physical Character, 221, pp. 163-198, 1921

[95] Graessley, W.W., Some Phenomenological Consequences of the Doi-Edwards Theory of Viscoelasticity, Journal of Polymer Science, 18(1), pp. 27-34, January 1980

[96] Ageorges, C., Ye, L., Hou, M., Advances in fusion bonding techniques for joining thermoplastic matrix composites: a review, Composites: Part A, 32, pp. 839-857, 2001

[97] Dara, P.H., Loos, A.C., 1987, Processing of thermoplastic matrix composites, Review of Progress in Quantitative Nondestructive Evaluation, 6, 1987, San Diego, CA

[98] Prager, S., Tirrell, M., The healing process at polymer-polymer interfaces, Journal of Chemical Physics, 75, pp. 5194-5198, 1981

[99] Sonmez, F.O., Hahn, H.T., Modeling of Heat Transfer and Crystallization in Thermoplastic Composite Tape Placement Process, Journal of Thermoplastic Composite Materials, 10(3), pp. 198-240, May 1997

[100] Yang, F., Pitchumani, R., Interlaminar contact development during thermoplastic fusion bonding, Polymer Science and Engineering, 42(2), pp. 424-438, February 2002

[101] Ezekoye, O.A., Lowman, C.D., Fahey, M.T., Hulme-Lowe, A.G., Polymer Weld Strength Predictions Using a Thermal and Polymer Chain Diffusion Analysis, Polymer Engineering and Science, 38(6), pp. 976-991

[102] Frenkel, J., Viscous flow of crystalline bodies under the action of surface tension, Journal of Physics, 9, pp. 385-391, 1945

[103] Eshelby, J.D., Discussion in paper by Shaler A.J., Seminar on the kinetics of sintering, Metallurgical Transactions, 185, pp. 806-807, 1949

[104] Bellehumeur, C., Kontopoulou, M., Vlachopoulos, J., The role of viscoelasticity in polymer sintering, Rheologica Acta, 37, pp. 270-278, March 1998

[105] Ahn, S.H., Montero, M., Odell, D., Roundy, S., Wright, P.K., Anisotropic material properties of used deposition modeling ABS, Rapid Prototyping Journal, 8(4), pp. 248-257, 2002

[106] Sood, A.K., Ohdar, R.K., and Hahapatra, S.S., Parametric Appraisal of Mechanical Property of Fused Deposition Modeling, Materials and Design, 31, pp. 287-295, 2010

[107] Mohamed, O.A., Masood, S. H., Bhowmik, J.L. Optimization of Fused Deposition Modeling Process Parameters: A Review of Current Research and Future Prospects. Advances in Manufacturing, 3(1), pp.42-53, 2015

[108] Bayraktar, O., Uzun, G., Cakiroglu, R., Guldas, A., Experimental study on the 3D-printed plastic parts and predicting the mechanical properties using artificial neural networks, Polymer Advanced Technologies, 28, pp. 1044-1051, 2017

[109] Ning, F., Cong, W., Hu, Y., Wang, H., Additive manufacturing of carbon fiber-reinforced plastic composites using fused deposition modeling: Effects of process parameters on tensile properties, Journal of Composite Materials, 51(4), pp. 451-462, 2017

[110] Velez-Garcia, G.M., Wapperom, P., Baird, D.G., Aning, A.O., Kunc, V., Unambiguous orientation in short fiber composites over small sampling area in a center-gated disk, Composites Part A, 43(1), pp. 104-113, 2012

[111] Jiang, D., Smith, D.E., "Mechanical Behavior of Carbon Fiber Composites Produced with Fused Filament Fabrication," Solid Freeform Fabrication Symposium Proceedings, pp. 884-898, August 2016

[112] Potente, H., Michel, P., Heil, M., "Infrared Radiation Welding: A Method for Welding High Temperature Resistant Thermoplastics," SPE ANTEC Proceedings, 1991

[113] Grimm, R.A., Yeh, H., "Infrared Welding of Thermoplastics. Colored Pigments and Carbon Black Levels on Transmission of Infrared Radiation," SPE ANTEC Proceedings, 1998

[114] Chen, Y.S., Benatar, A., "Infrared Welding of Polypropylene," SPE ANTEC Proceedings, 1995

[115] Shih, C.C., Burnette, M., Staack, D., Wang, J., Tai, B.L., Effects of cold plasma treatment on interlayer bonding strength in FFF process, Additive Manufacturing, 25, pp. 104-111, January 2019

[116] Hart, K.R., Dunn, R.M., Sietins, J.M., Hofmeister Mock, C.M., Mackay, M.E., Wetzel, E.D., Increased fracture toughness of additively manufactured amorphous thermoplastics via thermal annealing, Polymer, 144, pp. 1-13, April 2018

[117] Sweeny, C.B., Lackey, B.A., Pospisil, M.J., Achee, T.C., Hicks, V.K., Moran, A.G., Teipel, B.R., Saed, M.A., Green, M.J., Welding of 3D-printed carbon nanotube-polymer composites by locally induced microwave heating, Applied Sciences and Engineering, 3, pp.1-6, June 2017

[118] Tadmoor, Z. and Gogos, C.G., 2006, Principles of Polymer Processing, 2nd ed., John Wiley & Sons, Hoboken, NJ

[119] Danaila, I., Joly, P., Kaber, S.M., Postel, M., 2007, An Introduction to Scientific Computing; Twelve Computational Projects Solved with MATLAB, Springer, New York City, NY

[120] Biron, M., 2013, Thermoplastics and Thermoplastic Composites, 2nd ed., Elsevier, Amsterdam, Netherlands

[121] Barbero, E.J., 2011, Introduction to Composite Materials Design, 2nd ed., CRC Press, Boca Raton, FL

[122] Bertevas, E., Ferec, J., Khoo, B.C., Ausias, G., Phan-Thien, N., Smoothed particle hydrodynamics (SPH) modeling of fiber orientation in a 3D printing process, Physics of Fluids, 30, pp. 103103: 1-17, 2018

[123] Kubota, H., Flow Properties of ABS (acrylonitrile-butadiene-styrene) terpolymer, Journal of Applied Polymer Science, 19(8), pp. 2299-2308, 1975

[124] Ineos Styrolution, 2016, "Lustran 433," file:///C:/Users/blake/AppData/Local/Packages/Microsoft.MicrosoftEdge_8wekyb3d8bbwe/TempState/Downloads/StyrolutionTDS300600421212%20(1).pdf

[125] Russell, T., Jack, D.A.,"Fiber Aspect Ratio Characterization and Stiffness Prediction in Large-Area, Additive Manufactured, Short-Fiber Composites," ACCE 2019 (Accepted)

[126] Bergman, T.L, Lavine, A.S., Incropera, F.P., Dewitt, D.P., 2011, Fundamentals of Heat and Mass Transfer, 7th ed., John Wiley & Sons, Hoboken, NJ

[127] ThermoWorks, 2019, "Infrared Emissivity Table," https://www.thermoworks.com/emmisivity-table

[128] Mantell, S.C., Springer, G.S., Manufacturing Process Models for Thermoplastic Composites, Journal of Composite Materials, 26, pp. 2348-2377, 1992

[129] Coogan, T.J., 2011, “Fused Deposition Modeling (FDM) Part Strength and Bond Strength Simulations Based on Healing Models,” Masters Thesis, University of Massachusetts Lowell, Lowell, MA

[130] Franck, A., “Evaluation of the correct Modulus in Rectangular Torsion,” https://www.tainstruments.com/pdf/literature/APN024.pdf

[131] Volkersen, O., Die Nietkrafvereilung in Zugbeanspruchten Nietverbindungen Mit Knostanten Laschenquerschnitten, Luftfahrtforschung, 15(1/2), pp. 41-47, 1938

[132] Goland, M., Reissner, E., The Stresses in Cemented Joints, Journal of Applied Mechanics – T ASME, 11(1), pp. A17-A27, 1944

[133] Hart-Smith, L.J., Adhesive-Bonded Single-Lap Joints, NASA Langley Research Center, Report NASA CR-112236, January 1973